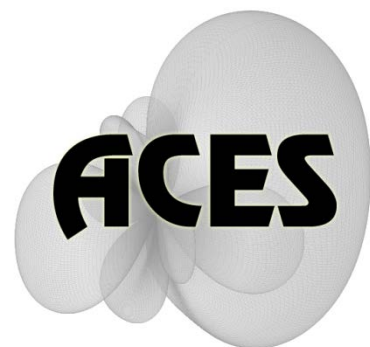


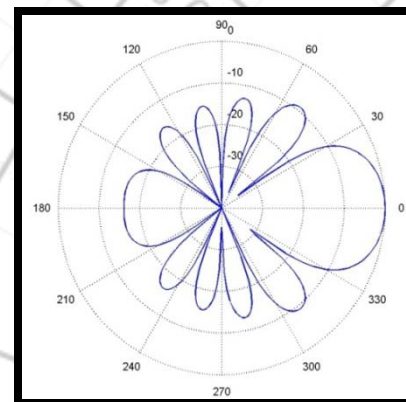
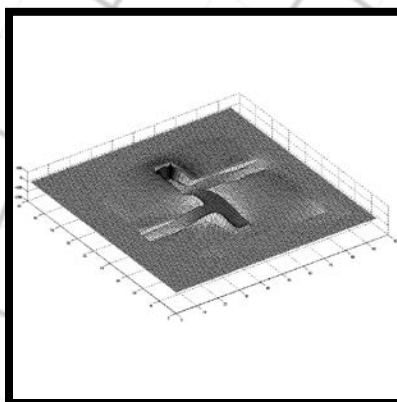
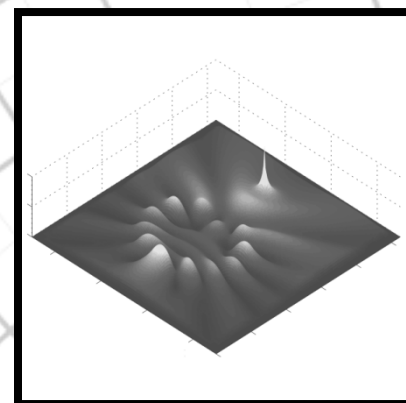
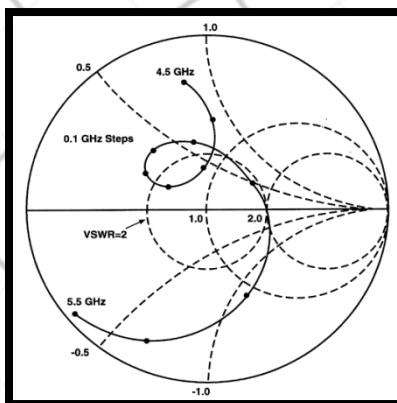
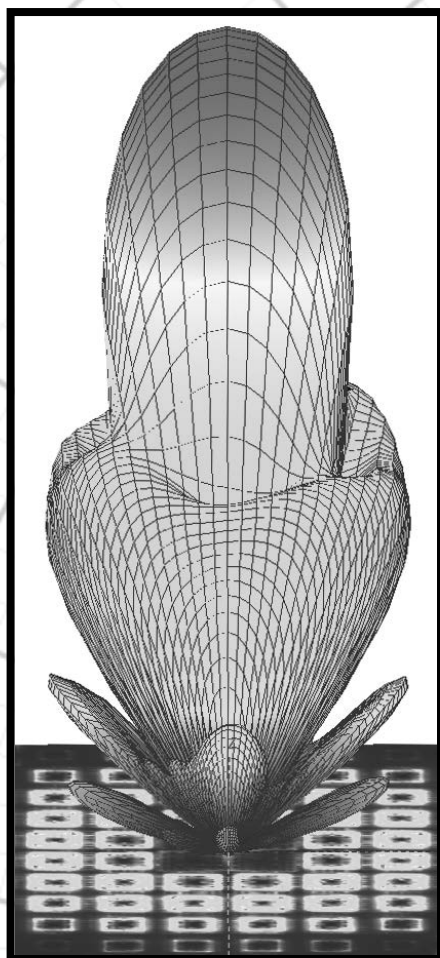
Applied Computational Electromagnetics Society

Journal



October 2012

Vol. 27 No. 10



ISSN 1054-4887

GENERAL PURPOSE AND SCOPE: The Applied Computational Electromagnetics Society (*ACES*) Journal hereinafter known as the *ACES Journal* is devoted to the exchange of information in computational electromagnetics, to the advancement of the state-of-the art, and the promotion of related technical activities. The primary objective of the information exchange is to inform the scientific community on the developments of new computational electromagnetics tools and their use in electrical engineering, physics, or related areas. The technical activities promoted by this publication include code validation, performance analysis, and input/output standardization; code or technique optimization and error minimization; innovations in solution technique or in data input/output; identification of new applications for electromagnetics modeling codes and techniques; integration of computational electromagnetics techniques with new computer architectures; and correlation of computational parameters with physical mechanisms.

SUBMISSIONS: The *ACES Journal* welcomes original, previously unpublished papers, relating to applied computational electromagnetics. Typical papers will represent the computational electromagnetics aspects of research in electrical engineering, physics, or related disciplines. However, papers which represent research in applied computational electromagnetics itself are equally acceptable.

Manuscripts are to be submitted through the upload system of *ACES* web site <http://aces.ee.olemiss.edu> See "Information for Authors" on inside of back cover and at *ACES* web site. For additional information contact the Editor-in-Chief:

Dr. Atef Elsherbeni
Department of Electrical Engineering
The University of Mississippi
University, MS 386377 USA
Phone: 662-915-5382
Email: atef@olemiss.edu

SUBSCRIPTIONS: All members of the Applied Computational Electromagnetics Society are entitled to access and download the *ACES Journal* any published journal article available at <http://aces.ee.olemiss.edu>. Printed issues of the *ACES Journal* are delivered to institutional members. Each author of published papers receives a printed issue of the *ACES Journal* in which the paper is published.

Back issues, when available, are \$50 each. Subscription to *ACES* is through the web site. Orders for back issues of the *ACES Journal* and change of address requests should be sent directly to *ACES* office at:

Department of Electrical Engineering
The University of Mississippi
University, MS 386377 USA
Phone: 662-915-7231
Email: aglisson@olemiss.edu

Allow four weeks advance notice for change of address. Claims for missing issues will not be honored because of insufficient notice, or address change, or loss in the mail unless the *ACES* office is notified within 60 days for USA and Canadian subscribers, or 90 days for subscribers in other countries, from the last day of the month of publication. For information regarding reprints of individual papers or other materials, see "Information for Authors".

LIABILITY. Neither *ACES*, nor the *ACES Journal* editors, are responsible for any consequence of misinformation or claims, express or implied, in any published material in an *ACES Journal* issue. This also applies to advertising, for which only camera-ready copies are accepted. Authors are responsible for information contained in their papers. If any material submitted for publication includes material which has already been published elsewhere, it is the author's responsibility to obtain written permission to reproduce such material.

**APPLIED
COMPUTATIONAL
ELECTROMAGNETICS
SOCIETY
JOURNAL**

October 2012
Vol. 27 No. 10
ISSN 1054-4887

The ACES Journal is abstracted in INSPEC, in Engineering Index, DTIC, Science Citation Index Expanded, the Research Alert, and to Current Contents/Engineering, Computing & Technology.

The illustrations on the front cover have been obtained from the research groups at the Department of Electrical Engineering, The University of Mississippi.

THE APPLIED COMPUTATIONAL ELECTROMAGNETICS SOCIETY

<http://aces.ee.olemiss.edu>

EDITOR-IN-CHIEF

Atef Elsherbeni

University of Mississippi, EE Dept.
University, MS 38677, USA

ASSOCIATE EDITORS-IN-CHIEF

Sami Barmada

University of Pisa, EE Dept.
Pisa, Italy, 56126

Fan Yang

University of Mississippi, EE Dept.
University, MS 38677, USA

Mohamed Bakr

McMaster University, ECE Dept.
Hamilton, ON, L8S 4K1, Canada

Yasushi Kanai

Niigata Inst. of Technology
Kashiwazaki, Japan

Mohammed Hadi

Kuwait University, EE Dept.
Safat, Kuwait

Mohamed Abouzahra

MIT Lincoln Laboratory
Lexington, MA, USA

EDITORIAL ASSISTANTS

Matthew J. Inman

University of Mississippi, EE Dept.
University, MS 38677, USA

Anne Graham

University of Mississippi, EE Dept.
University, MS 38677, USA

EMERITUS EDITORS-IN-CHIEF

Duncan C. Baker

EE Dept. U. of Pretoria
0002 Pretoria, South Africa

Allen Glisson

University of Mississippi, EE Dept.
University, MS 38677, USA

David E. Stein

USAF Scientific Advisory Board
Washington, DC 20330, USA

Robert M. Bevensee

Box 812
Alamo, CA 94507-0516, USA

Ahmed Kishk

University of Mississippi, EE Dept.
University, MS 38677, USA

EMERITUS ASSOCIATE EDITORS-IN-CHIEF

Alexander Yakovlev

University of Mississippi, EE Dept.
University, MS 38677, USA

Erdem Topsakal

Mississippi State University, EE Dept.
Mississippi State, MS 39762, USA

EMERITUS EDITORIAL ASSISTANTS

Khaled ElMaghoub

University of Mississippi, EE Dept.
University, MS 38677, USA

Mohamed Al Sharkawy

Arab Academy for Science and
Technology, ECE Dept.
Alexandria, Egypt

Christina Bonnington

University of Mississippi, EE Dept.
University, MS 38677, USA

SEPTEMBER 2012 REVIEWERS

**Ahmed Abdelrahman
Michel Audrey Abessolo
Shirook Ali
Mohamed Al-Sharkaway
Hakan Bagci
Mohamed Bakr
Veysel Demir
Juan Pablo Fernandez
Amir Hajiaboli
Julie Huffman
Mourad Ibrahim**

**Amir Jafargholi
Shambhu Jha
Yasushi Kanai
Ricardo Matias
Andrew Peterson
Ioannis Rekanos
Vince Rodriguez
Katherine Siakavara
Ahmet Turk
Yan Zhang**

THE APPLIED COMPUTATIONAL ELECTROMAGNETICS SOCIETY
JOURNAL

Vol. 27 No. 10

October 2012

TABLE OF CONTENTS

“High-Directive Patch and Dipole Antennas using Biased Grounded Ferrite” A. H. Gangaraj, M. Tayarani, and A. Abdolali.....	779
“Integration of An Optimized E-Shaped Patch Antenna into Laptop Structure for Bluetooth and Notched-UWB Standards using Optimization Techniques” A. M. Montaser, K. R. Mahmoud, and H. A. Elmikati.....	786
“Compact Ultra-Wideband (UWB) Bandpass Filter with Dual Notched Bands” S. Gao, S. Xiao, and J. L. Li.....	795
“Compact Microstrip-fed Monopole Antenna with Modified Slot Ground Plane for UWB Applications” M. Majidzadeh and C. Ghobadi.....	801
“Compact Microstrip Low-Pass Filter Design with Ultra-Wide Reject Band using a Novel Quarter-Circle DGS Shape” M. Challal, A. Boutejdar, M. Dehmas, A. Azrar, and A. Omar.....	808
“Band-Notch Slot Antenna with Enhanced Bandwidth by using Ω -Shaped Strips Protruded inside Rectangular Slots for UWB Applications” A. Valizade, Ch. Ghobadi, J. Nourinia, N. Ojaroudi, and M. Ojaroudi.....	816
“Broadband and Compact Zeroth-Order Resonant Antennas with Truncated Grounds” J. C. Liu and W. Shao.....	823
“Efficient PEEC-Based Simulations using Reluctance Method for Power Electronic Applications” D. Daroui and J. Ekman.....	828
“Method of Moments (MoM) Modeling for Resonating Structures: Propagation inside a Parallel Plate Waveguide” G. Apaydin, L. Sevgi.....	842
“Comparison of Dynamic Differential Evolution and Asynchronous Particle Swarm Optimization for Inverse Scattering of a Two-Dimensional Perfectly Conducting Cylinder” C. L. Li, C. H. Huang, C. C. Chiu, and C. H. Sun.....	850

High-Directive Patch and Dipole Antennas using Biased Grounded Ferrite

A. Hassani Gangaraj, M. Tayarani, and A. Abdolali

Department of Electrical Engineering
Iran University of Science and Technology, Tehran, 1684613114, Iran
Ali.Gangaraj@gmail.com, m_tayarani@iust.ac.ir, abdolali@iust.ac.ir

Abstract — In this paper, a new perfect magnetic conductor (PMC) substrate for improving the directivity of patch and dipole antennas is introduced. We used biased grounded ferrite to construct this new substrate. The most important difference between this substrate and the other artificial magnetic conductor (AMC) structures is the homogeneity. A conventional electromagnetic AMC has a periodic nature and as a result it is not homogenous but this novel substrate is homogenous. The results show that the directivity of both the patch and the dipole antennas is improved surprisingly in the presence of this novel homogenous PMC substrate. The physical reasons for the improvements are also given. Moreover, at the last section, we have calculated the magnetic loss of this magnetic anisotropic substrate.

Index Terms — Biased-grounded ferrite, dipole antenna, directivity, Faraday rotation, magnetic loss, patch antenna.

I. INTRODUCTION

Gyrotropic and magnetic materials have brought a lot of advantageous such as antenna miniaturization or beam squint for antenna applications [1-3]. Biased ferrites or magnetic photonic crystals are some examples for these types of materials.

A perfect magnetic conductor (PMC) is a concept, dual to the perfect electric conductor (PEC), but the nature did not provide a PMC material due to lack of magnetic charges [4]. Too many attempts were made to design artificial PMCs using electromagnetic band-gap (EBG) structures [5-6]. Suppression of surface waves by a PMC surface results in higher efficiency, smoother radiation pattern, and less back lobe and side lobe

levels in antenna applications particularly for microstrip antennas [7-9] like patch antenna.

A dipole antenna with low profile configuration is a main aim in wireless communications. In such a design, the overall height of the dipole antenna structure is usually less than one tenth of the operating wavelength [10]. Due to reverse image of antenna produced by a PEC ground plane the dipole antenna radiation efficiency encounters a dramatic reduction. [10]. To solve this problem, dipoles are located at a height of $0.25\lambda_{free\ space}$ or higher from the ground plane which is not practical for the wireless communication systems [10]. But in this paper we have reduced this height to $0.005\lambda_{free\ space}$.

Shahvarpour et al, in [11] has shown that the surface of a grounded biased ferrite can be used as a PMC surface. In this paper we have used this idea and asserted that a grounded biased ferrite can function as a new substrate for the patch antenna and as a new ground for the dipole antenna to solve the deficiencies of these antennas.

In Section II, we briefly explain the role of Faraday rotation in a grounded biased ferrite for creation of a PMC surface. In Section III, we explain the application of this PMC surface for increasing the directivity of patch antenna and furthermore, in Section IV, we use the property of grounded biased ferrite to increase the directivity of a dipole antenna and at last in Section V, we discuss and calculate the magnetic loss of this magnetic anisotropic substrate.

II. GROUNDED BIASED FERRITE

A grounded ferrite is a ferrite which is backed with a PEC plane. As it is stated in [11], at the first, consider an electromagnetic wave with E and H directed along the $+y$ and $+z$ respectively as it

is shown in Fig. 1a. When this electromagnetic wave illuminates the interface of the biased ferrite and the air as shown in Fig. 1b, it will experience Faraday rotation because both the wave propagation and the bias have a same direction along the x . With the respect to characteristics of the biased ferrite, we can design h (the thickness of the ferrite) such that the wave senses a 90° rotation through the ferrite. Therefore, the E and the H will be directed along $-z$ and $+y$ respectively as it is shown in Fig. 1c. When the wave hits the PEC at the back of the ferrite the electric field undergoes phase reversal and the new direction of E will be $+z$ as it is shown in Fig. 1d. The reflected wave from PEC will experience same 90° Faraday rotation again and the tangential magnetic fields will cancel out each other on the ferrite-air surface and at last the PMC condition will be satisfied as shown in Fig. 1e.

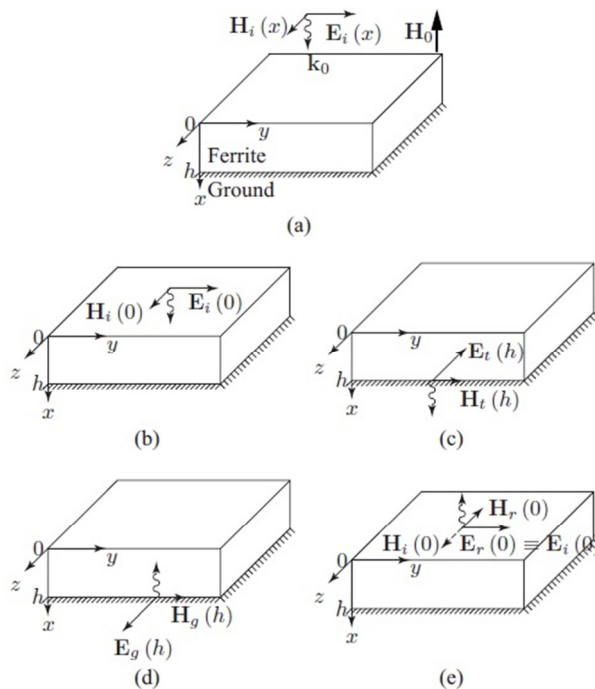


Fig. 1. (a to e) show the way that how a grounded ferrite can propose a PMC condition on its surface [11].

At this conceptual design of PMC surface, the effect of mismatch on ferrite-air surface is neglected. But it is mathematically shown in [11] that it has a negligible effect. At the continuation, we use this method to design a PMC substrate for patch and a ground for dipole antenna.

III. PATCH ANTENNA

Both the patch antenna and the dipole antenna are designed to operate at 3GHz. So, the grounded ferrite should satisfy the 90° Faraday rotation at 3GHz to realize a PMC substrate at the operating frequency. Now, we calculate the h (the thickness of ferrite substrate) using the following equations [12]:

$$\theta_{(\omega,y)} = -\left[\frac{\beta_{+(\omega)} - \beta_{-(\omega)}}{2}\right]y \quad (1)$$

$$\beta_{\pm(\omega)} = \omega\sqrt{\varepsilon\mu_0[\mu_{\omega} \pm k_{\omega}]} = \omega\sqrt{\varepsilon\mu_0\sqrt{[\mu'_{\omega} - j\mu''_{\omega}] \pm [k'_{\omega} - jk''_{\omega}]}} = \omega\sqrt{\varepsilon\mu_0\mu_{e\pm(\omega)}} \quad (2)$$

where β_{+} and β_{-} represent the right-handed circularly polarized (RHCP) and left-handed circularly polarized (LHCP) propagation constants, respectively. Because the ferrite is biased in the Y direction the permeability tensor is:

$$\bar{\mu} = \begin{bmatrix} \mu & 0 & -jk \\ 0 & \mu_0 & 0 \\ jk & 0 & \mu \end{bmatrix} \quad (3)$$

$$\mu = \mu_0(1 + x) \quad (4)$$

$$k = -j\mu_0 \quad (5)$$

$$x = x' - jx'' \quad (6)$$

$$y = y'' + jy' \quad (7)$$

$$x' = \frac{[\omega_0\omega_m(\omega_0^2 - \omega^2) + \omega_0\omega_m\omega^2\alpha^2]}{T} \quad (8)$$

$$x'' = \frac{[\alpha\omega_0\omega_m(\omega_0^2 + \omega^2(1 + \alpha^2))]}{T} \quad (9)$$

$$y' = \frac{[\omega\omega_m(\omega_0^2 - \omega^2(1 + \alpha^2))]}{T} \quad (10)$$

$$y'' = \frac{2\alpha\omega_0\omega_m\omega^2}{T} \quad (11)$$

$$T = [\omega_0^2 - \omega^2(1 + \alpha^2)]^2 + 4\omega_0^2\omega^2\alpha^2 \quad (12)$$

$$\alpha = \frac{\gamma\Delta H\mu_0}{2\omega} \quad (13)$$

$$\omega_0 = \mu_0\gamma H_0 \text{ and } \omega_m = 4\pi\gamma M_s \quad (14)$$

The angular velocity ω_0 is often called the Larmor frequency and γ is the ratio of mass over the angular momentum of an electron which is $1.759 \times 10^{11} \text{ C/Kg}$.

For the parameters: $f = 3\text{GHz}$, $4\pi M_s = 0.101 \text{ T}$, $\Delta H = 20 \text{ Oe}$, $\varepsilon_r = 13.2$, $\mu_0 H_0 = 0.124 \text{ T}$, the required 90° Faraday rotation angle will be achieved by putting $h = 4 \text{ mm}$. So, a grounded slab ferrite with the aforementioned parameter can realize a PMC surface.

The patch antenna on the new substrate is shown in Fig. 2. The patch antenna is supported by a

dielectric layer with $\epsilon_r = 2.35$ (blue section in Fig. 2). The dimensions of this dielectric layer are $38.4\text{mm} \times 38.3\text{mm}$ and the thickness of this supporter dielectric is 1.14 mm. This supporter dielectric is surrounded by the designed ferrite with the dimensions $103\text{mm} \times 103\text{mm}$ and its thickness is 4mm (the yellow section in Fig. 2). This ferrite substrate is backed by a PEC ground to form a grounded ferrite. This grounded ferrite can be biased by a slab magnet at the back of the PEC. This magnet provides $\mu_0 H_0 = 0.124$ T. The dimensions of the rectangular patch are $32\text{mm} \times 32\text{mm}$, this patch on the substrate with $\epsilon_r = 2.35$ and the dimensions of $38.4\text{mm} \times 38.3\text{mm}$ can resonate at 3 GHz. The patch is fed by a pin which is 8 mm away from the center point of the patch along with the z-axis. The S_{11} is plotted in Fig. 3. CST Microwave Studio 2009 is used for simulation.

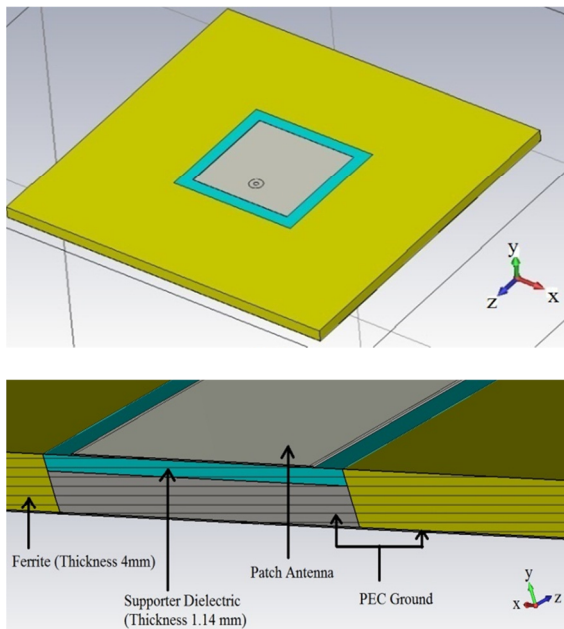


Fig. 2. The perspective view and side cut view of patch antenna on the ferrite substrate.

The operating frequency of the patch antenna shifts to 3.03 GHz in the presence of the ferrite. The directivity of a conventional patch antenna is almost 7 dBi but as it can be seen in Fig. 4 the directivity of the proposed patch antenna backed by new biased grounded ferrite substrate is 10.7 dBi at the 3.03 GHz.

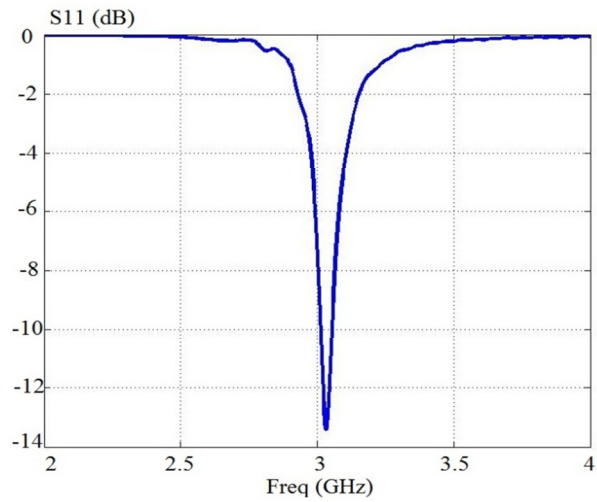


Fig. 3. S_{11} for patch antenna above the biased ferrite substrate.

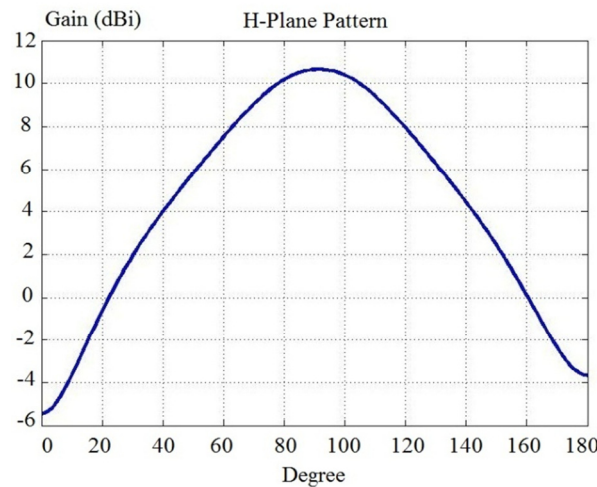
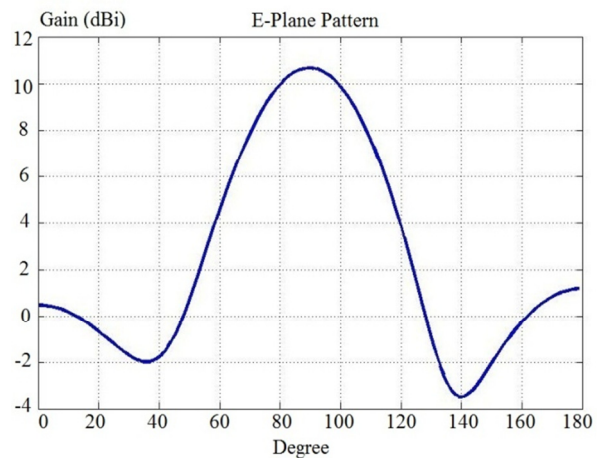


Fig. 4. Directivity of improved patch, E-plane and H-plane at $f_0 = 3.03\text{GHz}$.

The main reason for low directivity of the conventional patch antenna is the surface waves in TE, TM or hybrid modes excited by the patch into the dielectric slab. But by the biased grounded ferrite substrate, the surface of the substrate will change into PMC at operating frequency and the tangential component of the magnetic fields will vanish and therefore eliminates the TM modes. As a result, the amount of coupled power into the substrate will reduce and it causes an increase in the directivity and the gain.

IV. DIPOLE ANTENNA

The dipole antenna above the new ferrite ground is shown in Fig. 5.

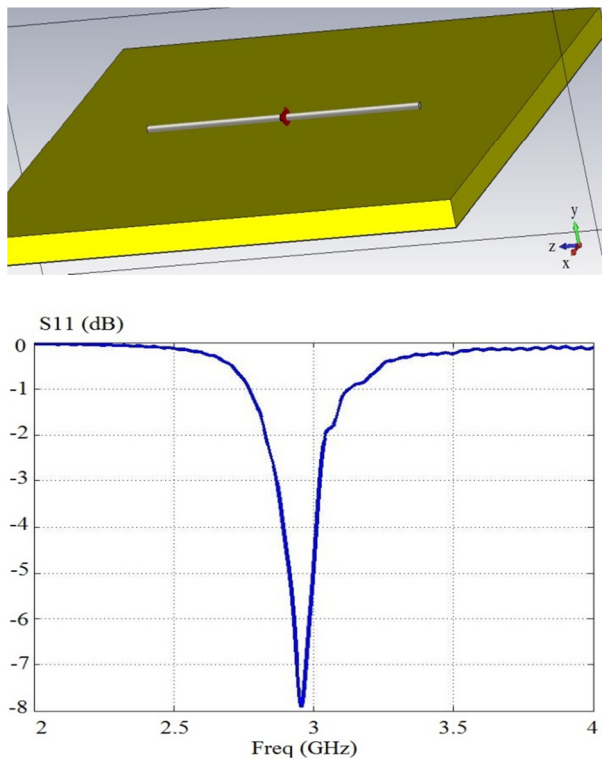


Fig. 5. The upper figure is the schematic of dipole antenna above the grounded biased ferrite substrate and the lower figure is the S_{11} of the antenna.

The dipole is designed to operate at 3GHz. The length of the dipole is 50mm and it is located $0.005\lambda_{3\text{GHz}}$ above the surface of the grounded biased ferrite. The ferrite should realize a PMC surface at 3GHz so we have used a ferrite which its characteristics are same as the ferrite which mentioned in the previous section. The grounded

ferrite dimensions are $90\text{mm} \times 70\text{mm} \times 4\text{mm}$. The operating frequency of the dipole antenna shifts to 2.95 GHz in the presence of the ferrite substrate. The S_{11} is shown in the Fig. 5.

The E-Plane and the H-Plane directivity of this system are obtained and they are shown in Fig. 6. The directivity of the dipole antenna is surprisingly increased to 10.4 dBi.

In wireless applications, Dipole antennas do not function effectively when positioned very close and parallel above a PEC ground plane because of the reverse image currents, which reduces the antenna radiation efficiency [10] but in our case a positive image current is created by biased grounded ferrite. This is the main reason for increasing the directivity.

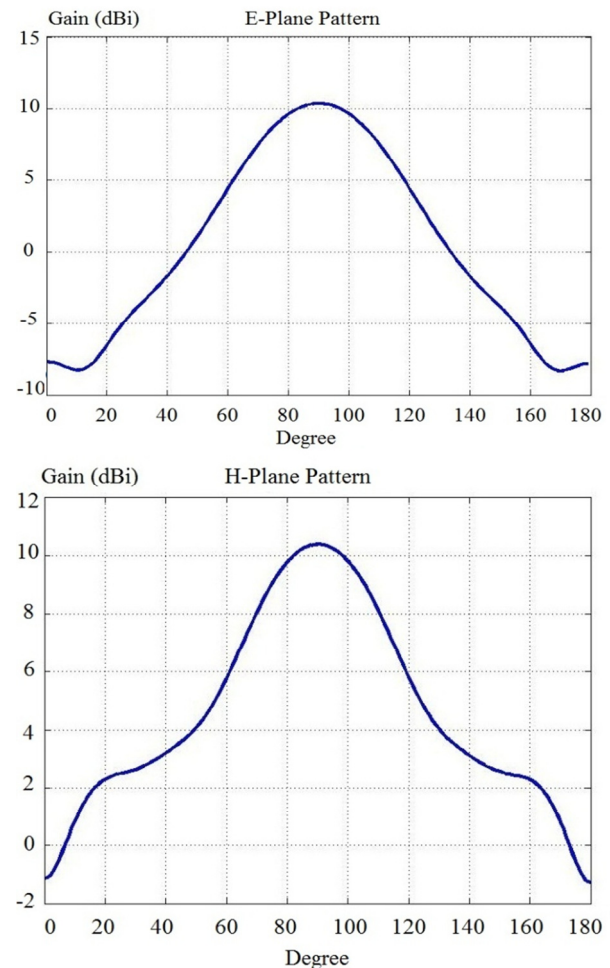


Fig. 6. The directivity of the improved dipole, E-plane and H-plane at $f_0 = 2.95\text{GHz}$.

In conventional dipole antenna which operates in wireless communication, for solving the problem

of reverse image and directivity reduction, the dipoles are positioned at the height of 0.25λ or higher from the ground plane which is not practical for the wireless communication systems [10]. But in our proposed structure, with this new PMC ground the height is decreased to 0.005λ .

V. MAGNETIC LOSS

As it is evident in Eq. (2), the right hand circularly polarization and left hand circularly polarization have different permeability. They are $\mu + k$ and $\mu - k$ for RHCP and LHCP respectively. The magnetic loss of the ferrite substrate can be taken into consideration by calculating the imaginary part of the permeability for different polarizations separately. The real and the imaginary parts of the $\mu + k$ and $\mu - k$ for right and left hand circularly polarizations are calculated and compared in Fig. 7.

As it is apparent the imaginary part of permeability for both polarizations is negligible in comparison with corresponding real parts. Therefore, we can conclude that the magnetic loss in this structure is not the main problem and we can neglect it. Also, it is apparent that the imaginary part is negative, which is expected for passive medium.

Now, we shortly discuss about the effects of the operating frequency on the performance for this proposed material specially, magnetic loss. There are two methods for realization of PMC surface by using a biased grounded ferrite with assumption of a fixed thickness. As it was mentioned above, to realize a PMC surface by biased grounded ferrites for a specific thickness, the ferrite should be able to rotate the electromagnetic wave 90 degrees. If we suppose a fixed thickness for the ferrite and a constant static magnetic field for biasing the ferrite, the speed of Faraday rotation will be increased by increasing the magnetic saturation of the ferrite. As a result of this phenomenon, the 90 degrees Faraday rotation will occur at lower frequencies but we should notice that by increasing the magnetic saturation the magnetic loss will also increase. Therefore, a trade-off should be considered between the loss and lowering the operating frequency. Another solution for the lowering the operating frequency for a fixed thickness can be found by decreasing the magnetic resonance of the ferrite which means decreasing the amount of the applied static

magnetic field. Decreasing the magnetic resonance of the ferrite seems better idea comparing with increasing the magnetic saturation because, by decreasing the amount of the applied static field the magnetic loss decreases.

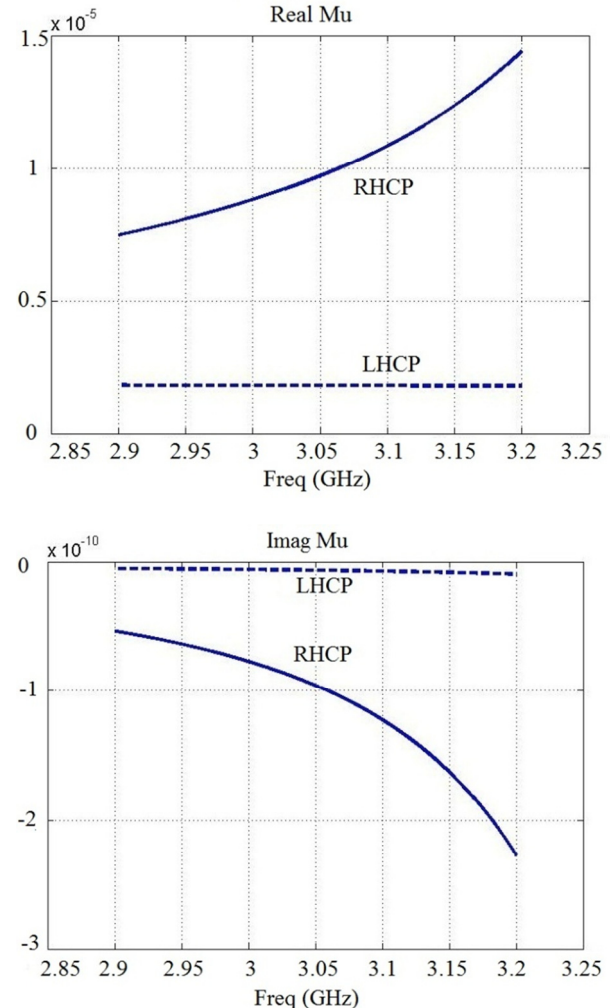


Fig. 7. Real and imaginary parts of effective permeability for RHCP and LHCP.

As a result of the aforementioned discussion the concept of PMC by using biased grounded ferrite is applicable for low frequency bands utilizing above mentioned ideas.

VI. CONCLUSION

A new substrate for patch antenna and a new ground for dipole antenna have been designed. The directivity and the magnetic loss are calculated. The results show that, the directivity for patch and dipole is improved meaningfully. This new substrate can increase the directivity of

the patch antenna up to 10.7 dBi and the directivity of the dipole antenna up to 10.4 dBi. And moreover the height of the dipole antenna was decreased from $0.25\lambda_{\text{free space}}$ to $0.005\lambda_{\text{free space}}$, which is very suitable for wireless communications. Since this substrate is made by ferrite, the magnetic loss is calculated and it is presented that this loss is negligible for this structure.

REFERENCES

- [1] E. Irci, K. Sertel, and J. L. Volakis, "Miniature Printed Magnetic Photonic Crystal Antennas Embedded into Vehicular Platforms," *Applied Computational Electromagnetics Society (ACES) Journal*, vol. 26, no. 2, pp. 109-114, February 2011.
- [2] John L. Volakis, Kubilay Sertel, and Chi-Chih Chen, "Miniature Antennas and Arrays Embedded within Magnetic Photonic Crystals and Other Novel Materials," *Applied Computational Electromagnetics Society (ACES) Journal*, vol. 22, no. 1, pp. 22-30, March 2007.
- [3] S. S. Iqbal, and M. R. Ali, "Beam Squint Using Integrated Gyrotropic Phase Shifter," *Applied Computational Electromagnetics Society (ACES) Journal*, vol. 23, no. 2, pp. 174-176, June 2008.
- [4] R. F. Harrington, Time-Harmonic Electromagnetic Fields, 2nd Edition, Wiley-IEEE Press, NJ, 2001.
- [5] D. Sievenpiper, L. Zhang, R. F. J. Broas, N. G. Alexopolous, and E. Yablonovitch, "High-Impedance Electromagnetic Surfaces with a Forbidden Frequency Band," *IEEE Trans. Microwave Theory Tech.*, vol. 47, no. 11, pp. 2059-2074, Nov. 1999.
- [6] F. R. Yang, K. P. Ma, Y. Qian, and T. Itoh, "A Novel TEM Waveguide using Uniplanar Compact Photonic Bandgap (UC-PBG) Structure," *IEEE Trans. Microwave Theory Tech.*, vol. 47, no. 11, pp. 2092-2098, Nov. 1999.
- [7] F. Yang and Y. R. Samii, "Microstrip Antennas Integrated with Electromagnetic Band-Gap (EBG) Structures: A Low Mutual Coupling Design for Array Applications," *IEEE Transactions on Antennas and Propagation*, vol. 51, no. 10, October 2003.
- [8] F. Yang and Y. R. Samii, "Wire Antenna on an EBG Ground Plane vs. Patch Antenna: A Comparative Study on Low Profile Antennas," *Electromagnetic Theory Symposium*, Ottawa, Canada, July 26-28, 2007.
- [9] QU D., Shafai L. and A. Foroozesh, "Improving Microstrip Patch Antenna Performance using EBG Substrates", *IEE Proc.-Microw. Antennas Propag.*, vol. 153, no. 6, December 2006.
- [10] M. K. T. Al-Nuaimi, W. G. Whittow, "Ultra Thin Dipole Antenna Backed by New Planar Artificial Magnetic Conductor", *Loughborough, UK Antennas & Propagation Conference*, 16-17 November 2009.
- [11] A. Shahvarpour, T. Kodera, A. Parsa, and C. Caloz, "Arbitrary Electromagnetic Conductor Boundaries using Faraday Rotation in a Grounded Ferrite Slab", *IEEE Transactions On Microwave Theory and Techniques*, vol. 58, no. 11, November 2010.
- [12] D. M. Pozar, *Microwave Engineering*, 3rd ed., John Wiley, 2005.



Seyyed Ali Hassani Gangaraj

was born in Amole, Mazandaran, Iran on Sep 7, 1988. He received his B.S .degree from Iran University of Science and Technology (IUST) at 2010 and currently he is carrying out his M.Sc. in IUST from 2010. His

main research areas are Metamaterials, Frequency Selective Surfaces (FSS), Wave Propagation in Anisotropic Media, Electromagnetic Wave Scattering, Microwave Filters and Devices, Antennas, Fundamental Electromagnetic Theory.



Majid Tayarani

was born in Tehran, Iran, in 1962. He received the B.Sc. degree from the University of Science and Technology, Tehran, Iran, in 1988, the M.Sc. degree from Sharif University of Technology, Tehran, Iran in 1992, and the

Ph.D. degree in communication and systems from the University of Electro- Communications, Tokyo, Japan, in 2001. From 1990 to 1992, he was a Researcher with the Iran Telecommunication Center, where he was involved with nonlinear microwave circuits. Since 1992, he has been a member of the faculty with the Department of Electrical Engineering, Iran University of Science and Technology, Tehran, Iran, where he is currently an Assistant Professor. His research interests are qualitative methods in engineering electromagnetic, electromagnetic compatibility (EMC) theory, computation and measurement techniques, microwave and millimeter-wave linear and nonlinear circuit design, microwave measurement techniques, and noise analysis in microwave signal sources.



Ali. Abdolali was born in Tehran, Iran, on May3, 1974 .He received B.S .degree from the University of Tehran, and M.S .degree from the University of Tarbiat Modares, Tehran, and the Ph.D .degree from the Iran University of Science and Technology (IUST), Tehran Ann Arbor, all in electrical engineering, in 1998, 2000, and 2010, respectively. In 2010, he joined the Department of Electrical Engineering, Iran University of Science and Technology, Tehran, Iran, where he is an assistant Professor of electromagnetic engineering. His research interests include electromagnetic wave scattering, Radar Cross Section (RCS) & RCSR, Radar Absorbing Materials (RAM), cloaking, Metamaterials, Wave Propagation in composite media (anisotropic, inhomogeneous, dispersive media), Frequency Selective Surfaces (FSS), Bio electromagnetism (BEM) .He has authored or coauthored over 20 papers in international journals & conferences.

Integration of An Optimized E-Shaped Patch Antenna into Laptop Structure for Bluetooth and Notched-UWB Standards using Optimization Techniques

A. M. Montaser¹, K. R. Mahmoud², and H. A. Elmikati³

¹Electrical Engineering Department
Sohag University, Sohag, 82524, Egypt
eng_ahmed_s81@yahoo.com

²Department of Electronics and Communications Engineering
Helwan University, Cairo, 11790, Egypt
Kurany_hameda@h-eng.helwan.edu.eg

³Department of Electronics and Communications Engineering
Mansoura University, Mansoura 35516, Egypt
mikati43@yahoo.com

Abstract — In this article, an optimized E-shaped patch antenna for Bluetooth (2.4 - 2.484 GHz) and UWB (3.1- 10.6 GHz) applications with WLAN (5.15 - 5.825 GHz) band-notched characteristics is proposed. The dimensions of the E-shaped structure in addition to the position of the slotted C-shape in the ground plane are optimized using recent optimization techniques such as modified particle swarm optimization (MPSO), bacterial swarm optimization (BSO), and central force optimization (CFO). The optimization algorithms were implemented using MATLAB-software and linked to the CST Microwave Studio Suite® version 2011 to simulate the antenna. Next, the effects of the laptop structure on the antenna radiation characteristics are considered. To validate the results, the antenna structures are simulated by the finite difference time domain method (FDTD).

Index Terms - E-shape antenna, FDTD method, notched-UWB, optimization techniques.

I. INTRODUCTION

The commercial usages of ultra-wideband

(UWB) frequency band from 3.1 GHz to 10.6 GHz, was approved by Federal Communications Commission (FCC) in 2002 [1]. Recently, UWB technology has been widely used in various radars and has attracted much attention for communication systems [2-4]. UWB antennas must cover FCC definition for the indoor and handheld UWB applications, have electrically small size, and hold a reasonable impedance match and omnidirectional radiation patterns over the entire band. With the development of UWB technology, various types of planar UWB antennas have been developed with many various shaped planar elements, such as rectangular, circular, elliptical, pentagonal, and triangular geometries for UWB applications [5-12]. One of the most widely studied antennas is the E-shaped antenna due to its broadband capability including 2-6 GHz wireless communication systems [13,14]. In [15], a wideband circularly polarized E-shaped patch antenna for wireless applications are proposed. Recently, a new miniaturized E-shaped printed monopole antenna is designed for UWB applications [16]. In addition, the E-shaped patch antenna is proposed in [17] for millimeter wave frequencies

(31.6-40 GHz).

Over past years, Bluetooth has been widely used in portable devices such as mobile phones, PDAs and notebooks etc. In 2006, the Bluetooth Special Interest Group selected the multi-band orthogonal frequency division multiplexing (MB-OFDM) version of the UWB to integrate with the current Bluetooth wireless technology. However, consumers usually prefer lighter and thinner products, and one of the solutions is to have a single antenna to work in both UWB and Bluetooth. On the other hand, some existing narrow bands for other communication systems, such as WLAN (5.15–5.825 GHz) cause interference with UWB systems. To solve this problem, it is desirable to design antennas with band-notched characteristic to minimize potential interference [18]. The undesired frequencies can be rejected using different techniques so that the system performance may be enhanced well. One simple way is to etch thin slots on the antenna surface, such as U-shaped slot [19], T-shaped slot [20], and L-shaped slot [21]. Moreover, a planar integrated antenna working on both Bluetooth and UWB applications with WLAN band notched characteristics has been recently introduced for systems operating in those two communication systems [22-24].

Furthermore, the latest trend is to build these wireless systems into portable devices through various interfaces [25-27]. For embedded solutions, the antennas are required to reside with the devices such as the laptop computer itself, underneath the plastic, composite, or metals covers. However, one has to suffer from the degraded performance of embedded antennas. The embedded antennas usually do not perform as well as external ones due to greatly reduced space required for optimal designs, being partially hidden within semi-conducting or conducting materials and the proximity effect of metallic cover and/or liquid crystal display (LCD) panel. To achieve acceptable performance of embedded antennas, the commonly used method is to keep the antenna away from any metal component of a laptop computer. Depending on the design of laptop computers and type of antennas, the distance between the antenna and metal components should be as large as possible [28].

In this study, an E-shaped patch antenna is optimized using recent optimization techniques such as modified particle swarm optimization (MPSO) and bacterial swarm optimization (BSO) in addition to central force optimization (CFO) which are completely described before in [29], [30], and [31], respectively. However in [30,31], simple antennas are considered with one or two variables to be optimized. In this paper, the antenna design is more complicated with multivariable and constraints. The antenna parameters such as return loss and radiation patterns are discussed. Then, the optimized E-shaped antenna will reside in a laptop computer to study the degradation performance of embedded antenna. The antenna is analyzed completely using CST Microwave Studio which linked with MATLAB to optimize the antenna via Visual Basic for Applications (VBA) programs. Interchanging information between CST Microwave studio and Matlab allows the implementation of optimization algorithms not included in the Microwave studio environment itself [32]. The paper is organized as follows. In Section II, the antenna design and numerical results are presented. Section III presents the degradation of the embedded E-shaped antenna in Laptop computer. Finally, Section IV presents the conclusions.

II. ANTENNA DESIGN AND NUMERICAL RESULTS

The schematic of the E-patch antenna structure is shown in Fig. 1(a), depicts the front and back structure of the patch antenna. The dimensions of E-shaped patch are arranged on a $28 \times 32 \times 0.8 \text{ mm}^3$ thick quartz-crystal substrate with permittivity constant $\epsilon_r = 3$. Concrete dimension parameters are shown in Fig. 1(b), where, $L_1 = 14.8 \text{ mm}$, $L_2 = 3.2 \text{ mm}$, $L_3 = 10 \text{ mm}$, and line width $w_1 = 2.8 \text{ mm}$. Fig. 1(c) shows the dimension parameters in ground plane such as $L_9 = 5 \text{ mm}$, $L_8 = 1 \text{ mm}$. A partial ground plane with C-shape slot is considered for band notch characteristic from 5 – 6 GHz. A 50Ω SMA is connected to the end of the feeding strip L_1 and grounded to the edge of the ground plane.

In this paper, the E-shape patch antenna dimensions are optimized firstly using the PSO algorithm integrated with the CST Microwave

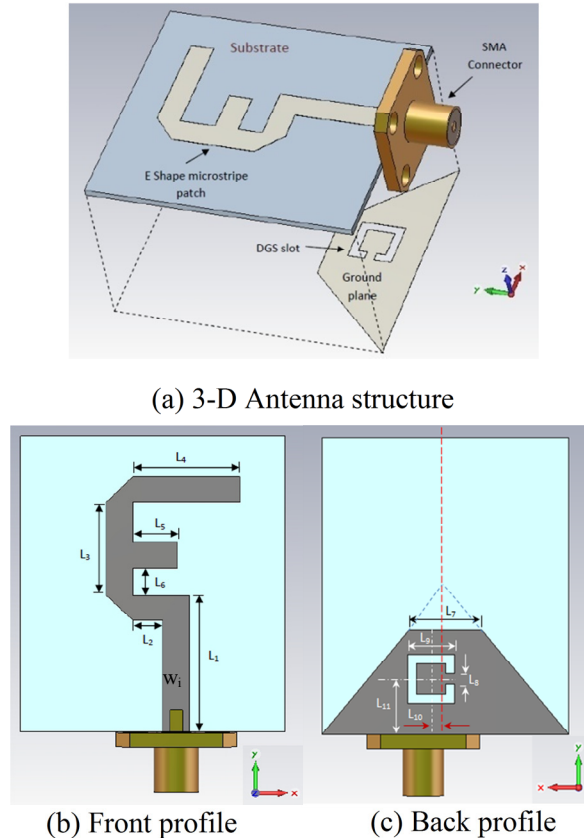


Fig. 1. E-shaped antenna geometry structure.

Studio package then other global optimization techniques such as MPSO, CFO, and BSO algorithms is considered to compare between their capabilities in antenna design using random initial values with the same number of evaluations (1000 evaluations). The antenna dimensions are optimized to operate in the Bluetooth band in addition to UWB notched at the WLAN communication band (5 – 6 GHz) by appropriate adjustment of the antenna parameters. As a result of this study, we focus on the following antenna parameters: L_4 along the upper side in the E-shape patch, L_5 along the middle side in the E-shape patch, L_6 the distance between the middle rib and lower rib, L_7 the upper side of the partial ground plane, finally the position of the etched C-shape in the partial ground plane through L_{10} and L_{11} . From the parametric studies, it is found that the top and middle rib strips of lengths are strongly affects the Bluetooth operating band. The width L_6 affects the return loss at the Bluetooth and

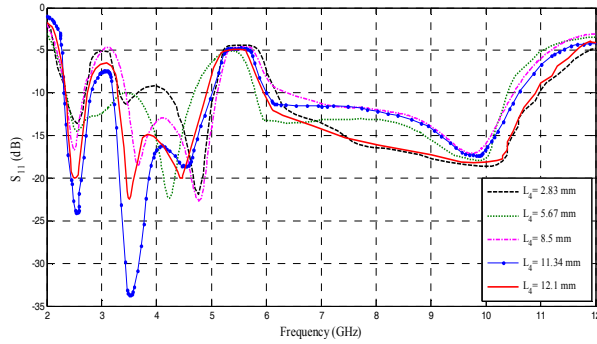
high frequency bands. The upper side of partial ground plane L_7 is a very critical parameter on the antenna performance where it completely affects the return loss curve. The lengths L_4 and L_5 are allowed to vary between 0 to 12.1 mm, L_6 vary from 0 to 6.4 mm and L_7 from 0 to 10 mm. For the position of the slotted C-shape, the decision space for L_{11} start from 3 to 9.8 mm, however the decision space of L_{10} depending on L_7 and L_9 to be from $(L_7-L_9)/2$ to $(L_7+L_9)/2$.

The first step is to define the objective function focusing on the antenna return loss (S_{11}) to be less than -10dB at the required operating bands. According to these remarks the objective function is calculated by using the following Equation:

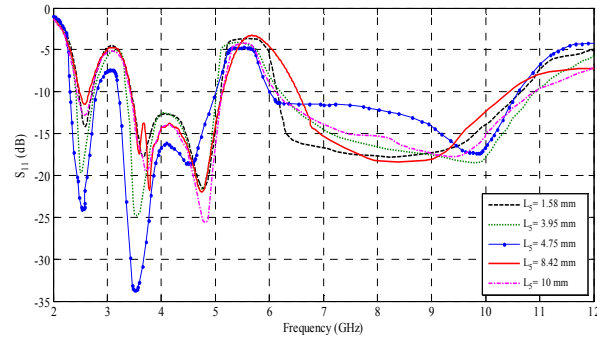
$$\begin{aligned} \text{Objective function} = & \min |S_{11}|_{2.45 \text{ GHz}} + \\ & \min |S_{11}|_{3.1 \sim 5 \text{ GHz}} + \max |S_{11}|_{5 \sim 6 \text{ GHz}} + \\ & \min |S_{11}|_{6 \sim 10.6 \text{ GHz}}. \end{aligned} \quad (1)$$

The optimization algorithms programmed with MATLAB will generate the antenna variables which will be sent to the CST simulator for calculating the fitness value of each individual [32].

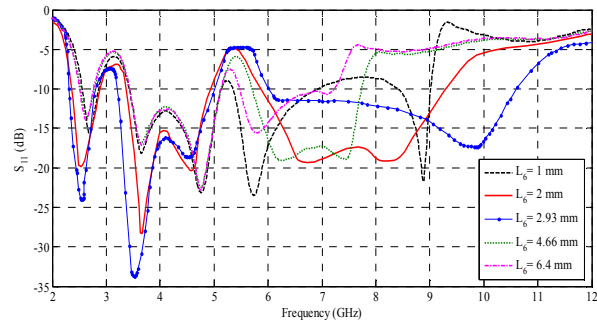
To investigate the antenna parameters effect on the antenna performance, a parametric study was carried out. It is found that the parameters which have a significant impact and remarkably on return loss S_{11} such as: L_4 along the upper side in the E-shape patch, L_5 along the middle side in the E-shape patch, L_6 the distance between the middle rib and lower rib, L_7 the upper side of the partial ground plane, finally the position of the etched C-shape in the partial ground plane through L_{10} and L_{11} . Figure 2(a) shows how the top rib strip length L_4 strongly affects the Bluetooth operating band. Also, the effect of varying the middle rib strip L_5 on the antenna performance has been presented in Fig. 2(b). Figure 2(c) describes the return loss based on increasing and decreasing the width L_6 . It can be noticed that the width L_6 affects the return loss at the Bluetooth and high frequency bands. Figure 2(d) shows that the upper side of partial ground plane L_7 is a very critical parameter on the antenna performance where it is completely affects the return loss curve. As



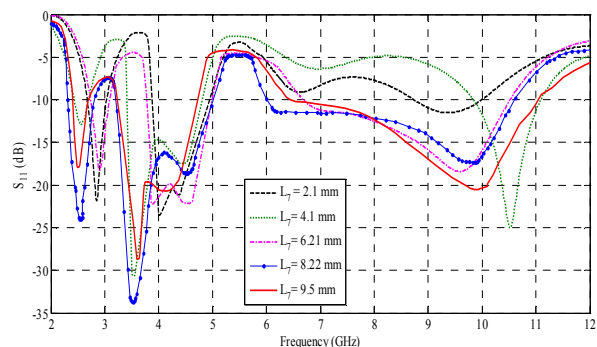
(a) The variation of L_4 parameter on the return loss.



(b) The variation of L_5 parameter on the return loss.



(c) The variation of L_6 parameter on the return loss.



(d) The variation of L_7 parameter on the return loss Fig. 2. Return loss curves for different antenna parameters.

for the rest of the parameters such as L_1, L_2, L_3 has no significant effect on return Loss S_{11} .

Table 1 shows the optimized values for selected antenna parameters from different optimization algorithms to achieve our goals. Figure 3 shows a comparison between the return losses obtained from different optimization techniques. From the comparisons between CFO and PSO, it can be seen that CFO had significantly better performance on the notched band. However, the CFO algorithm yielded slightly worse results on the Bluetooth band compared to PSO. It is clearly seen that, the BSO algorithm slightly outperformed to the MPSO algorithm in the Bluetooth band. However, approximately exact notch is obtained using MPSO (5.01 – 6 GHz) with a minimum S_{11} of -4.7 dB compared to the notch obtained by BSO (4.88 – 6 GHz) with an S_{11} of -4.15 dB. In summary, it can be found that the BSO algorithm outperformed PSO and CFO algorithms and was comparable to the MPSO for this antenna design. The simulated return loss results illustrate the ability of the proposed antenna to cover the ISM2450 band and UWB respectively with a notched band from 5 to 6 GHz. Table 1 shows also the required computation time for each algorithm on Toshiba laptop, Pentium(R) Dual core CPU @ 2GHz, 2.00 GB RAM, 32 bit operating system.

Table 1: The optimized antenna parameters using different optimization techniques

	Optimization Technique			
	PSO	MPSO	CFO	BSO
L_4 (mm)	8.8	11.34	10.52	9.78
L_5 (mm)	6.28	4.75	7.33	3.46
L_6 (mm)	3.94	2.93	5.18	5.37
L_7 (mm)	7.83	8.225	8.19	9.16
L_{10} (mm)	-0.527	1.59	-0.18	1.611
L_{11} (mm)	7.69	5.8	7.03	5.829
Time (day)	3.91	3.98	4.05	4.11

In the CST Microwave Studio simulator, which based on frequency domain solver (finite element), the following settings were used for time domain simulations: the minimum mesh step = 0.7, maximum mesh step = 2.605 and the mesh cells = 15,925 ($N_x = 36$, $N_y = 36$, $N_z = 14$). The mesh line ratio limit was set to 50 with an equilibrate mesh ratio of 1.19. Open add space boundary condition is applied in all directions with thermal boundaries isothermal ($T = \text{constant}$), while the parameters for FDTD computation were set as follows: the domain was $152 \times 138 \times 45$ cells with a cell size of $\Delta x = 0.29$ mm, $\Delta y = 0.29$ mm, $\Delta z = 0.29$ mm. The FDTD lattice needs to be terminated by perfectly matched layer (PML) on all sides; a spatially varying conductivity should be used in order to avoid numerical reflections at the interface of FDTD/PML regions. The computational domain was terminated with 8 cells perfectly matched layer in all directions (PML) with a time step of 551.7 ps and number of time step is 3000 time step.

Figure 4 illustrates the simulated current distribution on the optimized antenna by BSO algorithm at 2.45, 4, and 9 GHz. One can observe that, most current concentrated under the patch and more areas are needed for low frequency (2.45 GHz) than for high frequencies (4 and 9 GHz). The electric currents are mainly concentrated around the feeding strip at high frequencies. As shown in Figs. 4(b) and 4(c), the UWB element appears more active and the Bluetooth element appears colder at 4 and 9 GHz. Therefore, the top and middle rip strips are concluded to be responsible to generate the Bluetooth band.

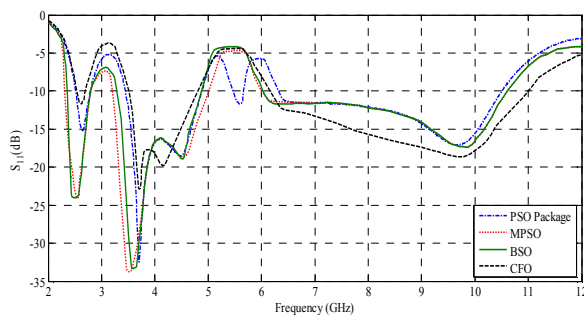
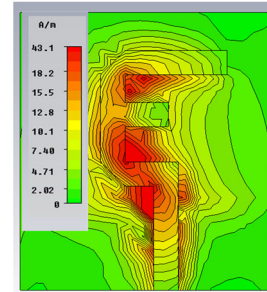
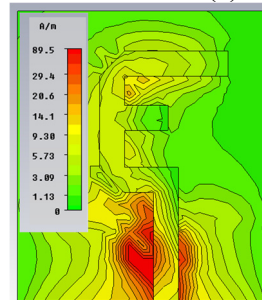


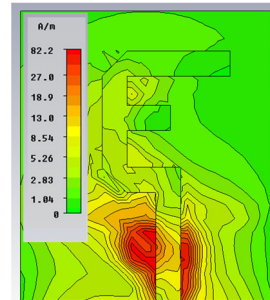
Fig. 3. Return losses comparison for optimized antenna using different optimization algorithms.



(a) $f = 2.45$ GHz



(b) $f = 4$ GHz



(c) $f = 9$ GHz

Fig. 4. Simulated current distributions of the optimized antenna using BSO at different frequencies.

III. EMBEDDED ANTENNA IN LAPTOP COMPUTER

To perform the study of integration and packaging, a generic model of a laptop computer is assumed. The overall dimensions of the laptop structure are: base unit ($2.6 \times 3.6 \times 3$ cm³) and screen ($2.5 \times 3.6 \times 1.5$ cm³). The open angle (α) of the computer to simulate actual operation is assumed to be 105° as shown in Fig. 5. The fabricated model consists of a Lucite ($\epsilon_r = 3.6$) body, clad in copper tape across the base unit structure, which is meant to mimic the computer's internal shielding. The optimized antenna using BSO algorithm is embedded in the center of the screen.

In this section, the effects of the laptop structure on the E-shaped antenna properties have been studied numerically. The input matching and radiation pattern characteristics have been calculated and compared. Figure 6 shows a comparison between the return losses obtained from the antenna in free space and

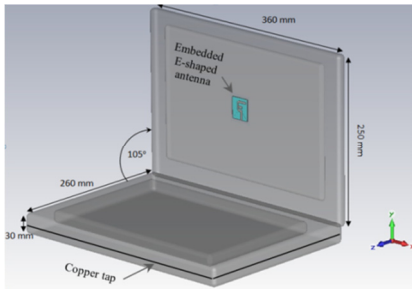


Fig. 5. Embedded E-shaped Antenna in Laptop.

those embedded in the Laptop structure with CST MWS package. It has been shown that the laptop structure slightly affect the antenna input reflection coefficient without disturbing the antenna resonant frequency and the impedance bandwidth. To validate the results, a finite difference time domain (FDTD) program code written with MATLAB is used to simulate the antenna either in free space or embedded in Laptop computer [33-35]. In addition, Fig. 6 shows a comparison between the simulated results with FDTD method and EM simulator of CST Microwave Studio software which based on a finite element method (FEM) for return loss in the range 2 – 12 GHz. A good agreement between the FDTD simulated results and those produced by CST Microwave Studio are achieved. The differences between the calculated results using the FDTD method and the CST MWS are related to the applied numerical techniques difference (FDTD and FEM). The parameters for FDTD computation were set as follows: the domain was $180 \times 200 \times 43$ cells with a cell size of $\Delta x = 0.2$ mm, $\Delta y = 0.2$ mm, $\Delta z = 0.283$ mm. The computational domain was terminated with perfectly matched layer (PML) of 8 cells in all directions.

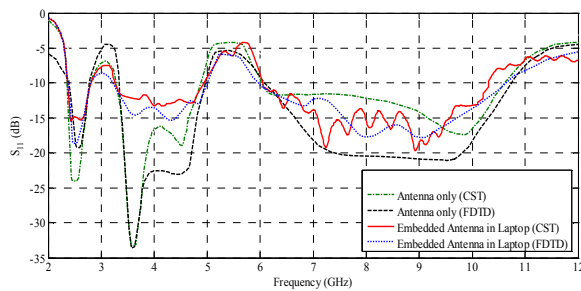


Fig. 6. Return losses comparisons between the antenna only and the embedded antenna in Laptop using FDTD method and the CST.

Figures 7(a), 7(b), and 7(c) show the radiation patterns of the antenna in free space and that embedded in laptop in x-z plane and x-y plane at 2.45, 4 GHz, and 9 GHz, respectively. It is found that, the antenna has approximately omni-directional characteristics in the x-z plane.

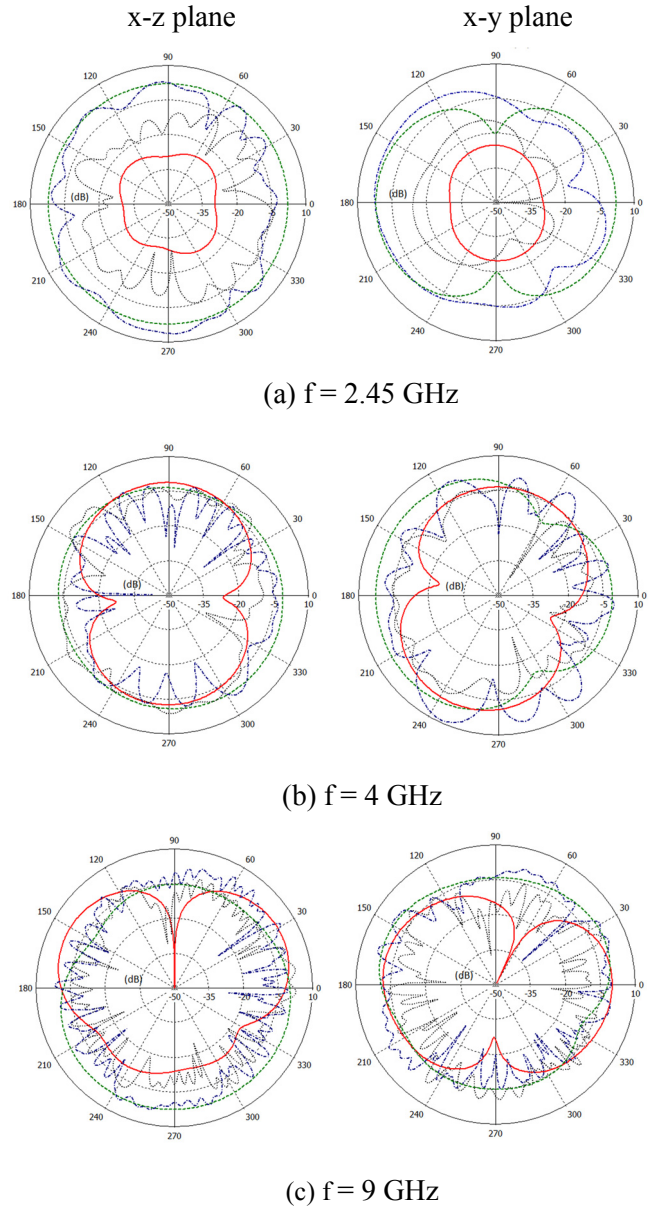


Fig. 7. Simulated radiation patterns of the proposed antenna at different frequencies.

— E_{θ} - - - E_{ϕ} (Antenna in free space)
 E_{θ} - . - E_{ϕ} (Embedded Antenna)

As expected, the presence of the laptop structure affects the antenna radiation pattern due to the

interference of the reflected wave from the keyboard with the direct wave radiated from the antenna element. In the horizontal plane, in spite of the presence of the keyboard structure, the (total power) radiation pattern is almost omnidirectional in both front and back hemispheres.

Finally, the effects of changing the open angle on the antenna characteristics are studied. Figure 8 shows the effect of changing the open angle on the return loss. It is found that, the return loss in the Bluetooth band is slightly improved as the open angle increase. In addition it affects the UWB range by decreasing and increasing the high cutoff frequency. The effect of changing the open angle on the radiation patterns are depicted in Fig. 9. As shown in figure, a slight change is observed due to changing the open angle without any effect on the antenna omnidirectionality.

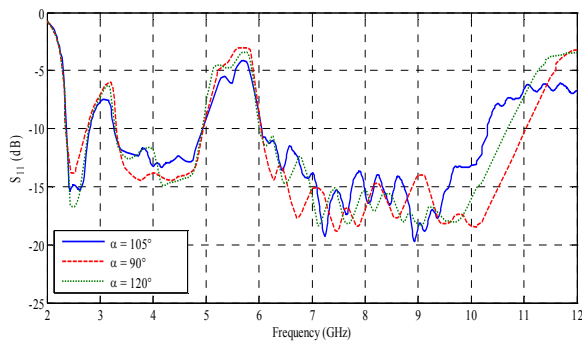


Fig. 8. Return losses comparison for embedded antenna with different open angles.

IV. CONCLUSIONS

In this article, an E-shaped patch antenna is designed using recently optimization techniques such as MPSO, CFO, and BSO for Bluetooth/notched UWB applications. The algorithms have been implemented in MATLAB and the prototype simulations have been carried out using the CST Microwave Studio simulator. It is found that the BSO algorithm is slightly outperformed than MPSO and CFO. In addition, the optimized antenna is embedded in laptop computer which slightly affect the antenna return loss without disturbing the resonant frequency and the impedance bandwidth; however, it affects the antenna

radiation patterns without any disturbance on the antenna omni-directionality.

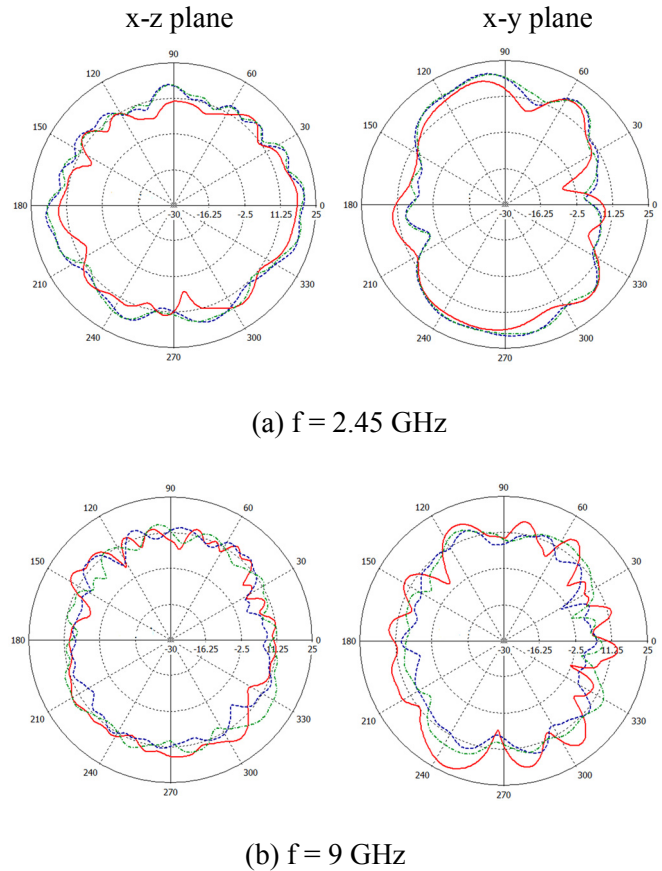


Fig. 9. The simulated radiation patterns of the embedded antenna in x-z, and x-y planes at different frequencies.

--- $\alpha = 90^\circ$ — $\alpha = 105^\circ$ - - - $\alpha = 120^\circ$

ACKNOWLEDGEMENT

We would like to acknowledge the Electronics Research Institute (ERI), Microstrip Department for the support and cooperation during simulation process of this research.

REFERENCES

- [1] Federal Communications Commission, *First Report and Order on Ultra-Wideband Technology*, FCC 02-48, Washington, DC, April 22, 2002.
- [2] B. Allen, M. Dohler, E. E. Okon, W. Q. Malik, A. K. Brown, and D. J. Edwards, *Ultra-Wideband Antennas and Propagation for Wireless Communications, Radar and Imaging*, John Wiley & Sons, USA, 2007.

- [3] R. Azim, M. T. Islam, and N. Misran, "Design of a Planar UWB Antenna with New Band Enhancement Technique," *Applied Computational Electromagnetics Society (ACES) Journal*, vol. 26, no. 10, pp. 856-862, October 2011.
- [4] A. T. Mobashsher, M. T. Islam, N. Misran, "Wideband Compact Antenna with Partially Radiating Coplanar Ground Plane," *Applied Computational Electromagnetics Society (ACES) Journal*, vol. 26, no. 1, pp. 73-81, January 2011.
- [5] D. H. Kwon and Y. Kim, "CPW-Fed Planar Ultrawideband Antenna with Hexagonal Radiating Elements," in *Proc. IEEE Int. Symp. Antennas Propagation*, vol. 3, pp. 2947-2950, Jun. 2004.
- [6] A. Abbosh and M. Bialkowski, "Design of Ultra Wideband Planar Monopole Antennas of Circular and Elliptical Shape," *IEEE Trans Antennas Propag.*, vol. 56, pp. 17-23, 2008.
- [7] C.-C. Lin and H.-R. Chuang, "A 3-12 GHz UWB Planar Triangular Monopole Antenna with Ridged Ground-Plane," *Progress in Electromagnetics Research*, vol. 83, pp. 307-321, 2008.
- [8] M. A. A. Fattah, A. M. A. Allam, and S. I. Shams, "Irregular Pentagon Monopole Structured Antenna for Ultra-Wideband Communication Systems," *Antennas and Propagation (MECAP), 2010 IEEE Middle East Conference*, Cairo, Oct. 20-22, pp. 1-4, 2010.
- [9] M. Hayouni, F. Choubani, M. Denden, T. H. Vuong, and J. David, "A Novel Compact Ultra-wideband Rectangular Shaped Antenna," *Progress In Electromagnetics Research Symposium Proceedings*, Marrakesh, Morocco, Mar. 20-23, pp. 381-385, 2011.
- [10] J. William and R. Nakkeeran, "A New UWB Slot Antenna with Rejection of WiMax and WLAN Bands," *Applied Computational Electromagnetics Society (ACES) Journal*, vol. 25, no. 9, pp. 787 – 793, September 2010.
- [11] D. S. Javan and O. H. Ghouchani, "Cross Slot Antenna with U-Shaped Tuning Stub for Ultra Wideband Applications," *Applied Computational Electromagnetics Society (ACES) Journal*, vol. 24, no. 4, pp. 427 – 432, August 2009.
- [12] M. Naghshvarian-Jahromi and N. Komjani-Barchloui, "Analysis of the Behavior of Sierpinski Carpet Monopole Antenna," *Applied Computational Electromagnetics Society (ACES) Journal*, vol. 24, no. 1, pp. 32 – 36, February, 2009.
- [13] F. Yang, X.-X. Zhang, X. Ye, and Y. Rahmat-Samii, "Wide-Band E-Shaped Patch Antennas for Wireless Communications," *IEEE Trans. Antennas Propag.*, vol. 49, no. 7, pp. 1275-1279, Jul. 2001.
- [14] Y. Ge, K. P. Esselle, and T. S. Bird, "E-Shaped Patch Antennas for High-Speed Wireless Networks," *IEEE Trans. Antennas Propag.*, vol. 52, no. 12, pp. 1094-1100, Dec. 2004.
- [15] A. Khidre, K. F. Lee, F. Yang, and A. Elsherbeni, "Wideband Circularly Polarized E-Shaped Patch Antenna for Wireless Applications," *IEEE Antennas and Propagation Magazine*, pp. 219-229, Oct. 2010.
- [16] K. A. Jawad and A. S. Hussain, "A New Miniaturized E-shaped Printed Monopole Antenna for UWB Applications," *Progress In Electromagnetics Research Symposium Proceedings*, Suzhou, China, Sept. 12-16, pp. 1273-1276, 2011.
- [17] W. He, R. Jin, and J. Geng, "E-Shape Patch with Wideband and Circular Polarization for Millimeter-Wave Communication," *IEEE Transactions on Antennas and Propagation*, vol. 56, no. 3, March 2008.
- [18] Y. Kim and D.-H. Kwon, "CPW-Fed Planar Ultra Wideband Antenna Having a Frequency Band Notch Function," *Electronics Letters*, issue 7, pp. 403-405, April 2004.
- [19] H.-I. Zhou, B.-H. Sun, Q.-Z. Liu, and J.-y. Deng, "Implementation and Investigation of U-Shaped Aperture UWB Antenna with Dual Bandnotched Characteristics," *Electron.Lett.*, vol. 44, no. 24, pp. 1387-1388, Nov. 2008.
- [20] M. Ojaroudi, C. Ghobadi, and I.Nourinia, "Small Square Monopole Antenna with Inverted T -Shaped Notch in the Ground Plane for UWB Application," *IEEE Antennas Wireless Propag. Lett.*, vol. 8, pp. 728- 731, 2009.
- [21] R. Zaker, C. Ghobadi, and I.Nourinia, "Bandwidth Enhancement of Novel Compact Single and Dual Band-Notched Printed Monopole Antenna with a Pair of L-Shaped Slots," *IEEE Trans. Antennas Propag.*, vol. 57, no. 12, pp. 3978-3983, Dec. 2009.
- [22] C. Kim, H. Ahn, J. Kim, X. Cheng, and Y.-K. Yoon, "A Compact 5 GHz WLAN Notched Bluetooth/UWB Antenna," *IEEE Antennas and Propagation Society International Symposium (APS/URSI)*, Toronto, pp. 11-17 July 2010.
- [23] S. K. Mishra, R. Gupta, A. Vaidya, and J. Mukherjee, "Printed Fork Shaped Dual Band Monopole Antenna for Bluetooth and UWB Applications with 5.5 GHz WLAN Notched Characteristics," *Progress in Electromagnetic Research C*, Vol. 22, pp. 195-210, 2011.
- [24] B. S. Yildirim, B. A. Cetiner, G. Roqueta, and

- L. Jofre, "Integrated Bluetooth and UWB Antenna," *IEEE Antennas and Wireless Propagat. Letters*, vol. 8, pp. 149-152, 2009.
- [25] K. Ito and T. Hosoe, "Study of the Characteristics of Planar Inverted F Antenna Mounted in Laptop Computers for Wireless LAN," *Proc. IEEE Ant. and Prop. Society Int. Symposium*, vol. 2, pp. 22-25, Columbus, Ohio, USA, July 2003.
- [26] D. Liu, B. P. Gaucher, E. B. Flint, T. W. Studwell, H. Usui, and T. J. Beukema, "Developing Integrated Antenna Subsystems for Laptop Computers," *IBM Journal of Research and Development*, vol. 47, no. 2/3, pp. 355-367, March/May 2003.
- [27] G. H. Huff, J. Feng, S. Zhang, G. Cung, and J. T. Bernhard, "Directional Reconfigurable Antennas on Laptop Computers: Simulation, Measurement and Evaluation of Candidate Integration Positions," *IEEE Trans. On Antennas and Propagation*, vol. 52, no. 12, pp. 3220-3227, Dec. 2004.
- [28] J. Guterman, A. A. Moreira, and C. Peixeiro, "Laptop Structure Effects on an Integrated Omnidirectional Wrapped Microstrip Antenna," *Microwaves, Radar & Wireless Communications*, 2006. MIKON 2006. International Conference, 1003 – 1006, 22-24 May 2006.
- [29] K. R. Mahmoud, M. El-Adawy, R. Bansal, S. H. Zainud-Deen, and S. M. M. Ibrahim, "MPSO-MOM: A Hybrid Modified Particle Swarm Optimization and Method of Moment Algorithm for Smart Antenna Synthesis," *Electromagnetics*, vol. 28, pp. 411-426, 2008.
- [30] K. R. Mahmoud, "Design Optimization of a Bow-Tie Antenna for 2.45 GHz RFID Readers using a Hybrid BSO-NM Algorithm," *Progress In Electromagnetics Research*, PIER 100, 105-117, 2010.
- [31] K. R. Mahmoud, "Central Force Optimization: Nelder-Mead Hybrid Algorithm for Rectangular Microstrip Antenna Design," *Electromagnetics*, vol. 31, iss. 8, pp. 578-592, 2011.
- [32] A. M. Montaser, K. R. Mahmoud, and H. A. Elmikati, "An Interaction Study Between Pifas Handset Antenna and a Human Hand-Head in Personal Communications," *Progress In Electromagnetics Research B*, vol. 37, pp. 21-42, 2012.
- [33] K. S. Yee, "Numerical Solution of Initial Boundary Value Problems Involving Maxwell's Equations in Isotropic Media," *IEEE Trans. Antennas and Propagation*, vol. 14, pp. 302-307, May 1966.
- [34] A. Taflove and S. C. Hagness, *Computational Electrodynamics: The Finite-Difference Time-*

Domain Method, 3rd edition. Norwood, MA: Artech House, 2005.

- [35] E. Atef and V. Demir, *The Finite Difference Time Domain Method for Electromagnetics: With MATLAB Simulations*, SciTech Publishing, North Carolina, 2009.



Ahmed M. Montaser was born in Luxor, Egypt, on August 1981. He received his B.S. and M.S. degrees in Communications and Electronics Engineering from South Valley University – Aswan (Egypt) in 2003 and 2009. He is currently working toward the Ph.D. degree in the area of antenna design for wireless communications using optimization techniques at Mansoura University. His current research interests are in the area of antenna design and Multiband PIFA antenna for Mobile Phone Communications using optimization techniques.



Korany R. Mahmoud was born in Cairo, Egypt, on August 1975. He received his B.S. and M.S. degrees in Communications and Electronics Engineering from University of Helwan in 1998 and 2003. His Ph.D degree from Helwan University in collaboration with the University of Connecticut, USA in 2008. Currently he is an assistant professor at the department of communication and electronics in the same faculty. Dr. Mahmoud has served as an Editor/Reviewer of Int. J. RF & Microwave CAE. His current research interests include the areas of antenna design, array beamforming using optimization techniques, the interaction between the handsets and the human head.



Hamid A. El-Mikati was born in Rozetta, Egypt, in 1943. He received the B.Sc. and M.Sc. degrees in electrical engineering from Alexandria University, Egypt, in 1964 and 1969, respectively, and the Ph.D. degree from the Polytechnic Institute, Leningrad (now St. Petersburg State Polytechnic University, Russia), in 1974. Since 1975 he has been with the Faculty of Engineering, Mansoura University, Egypt, where he is currently Professor Emeritus at the department of Electronics and Electrical Communications. His research interests have included computational electromagnetics and optimization techniques especially with applications to microwave and optical passive devices and antenna arrays.

Compact Ultra-Wideband (UWB) Bandpass Filter with Dual Notched Bands

Shanshan Gao, Shaoqiu Xiao, and Jia-Lin Li

School of Physical Electronics,
University of Electronic Science and Technology of China, Chengdu, 610054, China
issgao@hotmail.com, xiaoshaoqiu@uestc.edu.cn, jialinuestc@yahoo.com.cn

Abstract — A compact ultra-wideband (UWB) bandpass filter with two controllable highly selective notched bands is presented. The modified stepped impedance resonator (SIR) and two interdigital feed-lines realize the UWB passband. The loaded stubs at each side of the modified SIR and the U-shaped slot on the ground plane produce two notched bands at desired frequencies without increasing the total size of the filter. High performance achieved by the proposed UWB filter is validated by both simulations and measurements.

Index Terms - Ultra-wideband (UWB), bandpass filter (BPF), stepped-impedance resonator (SIR), defected ground structure.

I. INTRODUCTION

In recent years, due to the attractive merits such as high speed data transmission rate, low power operation, and large data capacity, ultra-wideband (UWB) technology has attracted much attention since the Federal Communication Commission (FCC) released the frequency spectrum from 3.1 to 10.6 GHz for commercial applications in 2002 [1]. Filters [2-5] are the key components in UWB systems. Many researchers have explored various UWB bandpass filters via different methods: a ring resonator connected by a stub [6]; multiple-mode resonator [7]; short-circuited coplanar waveguide (CPW) multiple-mode resonator [8]. It is well known that there are some undesired narrow band RF signals such as wireless local-area network (WLAN) radio signals within the UWB frequency range. Thus, there is an increasing requirement in UWB bandpass filters

and antennas with one or multiple notched bands within the allocated UWB spectrum [9-14].

This paper presents a UWB filter using the modified stepped impedance resonator (SIR) and two interdigital feed-lines. Two controllable highly selective notched bands within the UWB passband are generated by respectively using loaded stubs at each side of the modified SIR and etching a U-shaped slot on the ground plane. Characteristics of such a filter are studied and a demonstrator is validated by simulations and measurements.

II. NOTCHED BANDS DESIGN

In our initial works [15], a UWB bandpass filter with one controllable notched band within the UWB passband is realized by using a stub-loaded modified SIR and two identical interdigital feed-lines, as shown in Fig. 1(a) except the U-shaped slot. The UWB passband bandwidth is achieved by the modified SIR and two identical interdigital feed-lines. A controllable notched band within the UWB passband is generated by loading identical stub between the high impedance double-lines at each side of the modified SIR. By properly adjusting the length of the loaded stub i.e., L_4 , the lower notched band at desired frequency can be achieved, as shown in Fig. 1(b). The bandwidth of the notched band can be controlled by tuning the width of the loaded stub, i.e., W_4 . Figure 1(c) shows the simulated frequency responses with varying W_4 . It can be seen that the bandwidth decreases when increasing W_4 . According to above analysis, the loaded stubs can generate a notched band at desired frequency without significant influence on the passband performance.

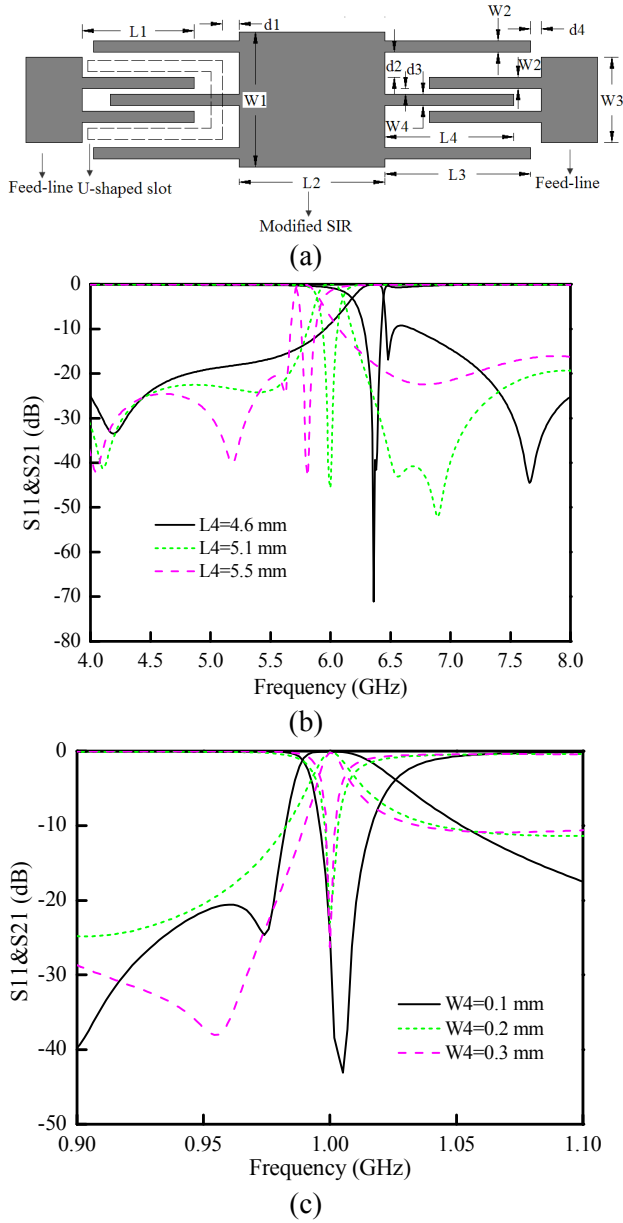


Fig. 1. (a) Structure of the UWB bandpass filter, (b) Simulated frequency responses of the loaded stubs for varying L_4 ($W_4=0.1$ mm), (c) Simulated frequency responses for varying W_4 ($L_4=5.5$ mm, $d_2=0.1$ mm, and $d_3=0.1$ mm).

The concept of the defected ground structure (DGS) has been used extensively in the field of microwave devices design. Here a U-shaped DGS is proposed to generate the upper notched band. Figure 2 shows the configuration and equivalent circuit of the proposed DGS resonator. The U-shaped slot in the ground plane disturbs the shield

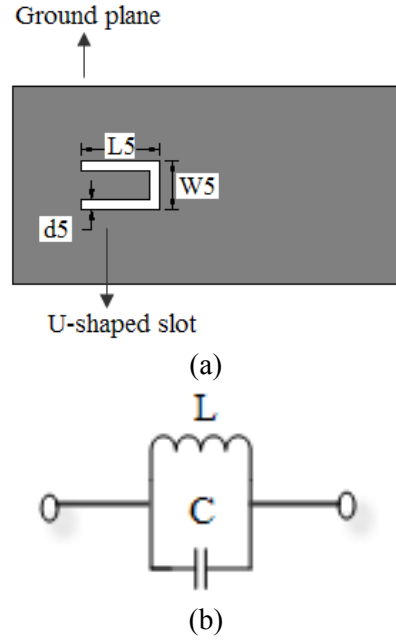


Fig. 2. (a) Configuration of the U-shaped slot, (b) Its equivalent circuit.

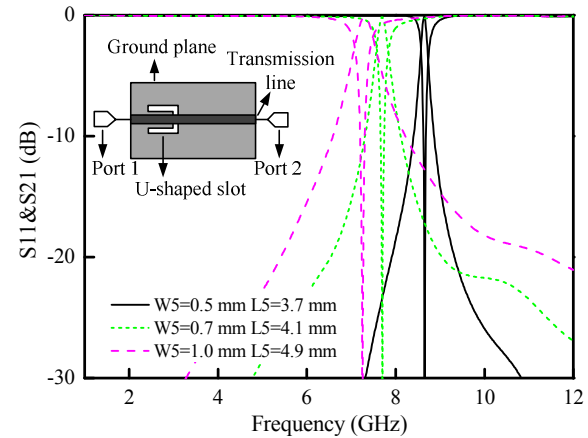


Fig. 3. Frequency responses of the proposed DGS for varying W_5 and L_5 ($d_5=0.1$ mm).

current distribution in the ground plane, which changes the capacitance and inductance of the transmission line. Thus, the resonance frequency of the proposed DGS depends on the physical dimensions of the U-shaped slot. In order to investigate the influence of the proposed DGS dimensions on the frequency characteristics, three cases are simulated. The value of d_5 is fixed to 0.1 mm for all cases when the values of W_5 and L_5 are varied. The linewidth of the transmission line for the proposed DGS section is chosen as 50Ω

Table 1: Extracted equivalent circuit parameters for varying W5 and L5

W5 (mm)	L5 (mm)	Resonance Frequency (GHz)	Cutoff Frequency (GHz)
0.5	3.7	8.65	8.57
0.7	4.1	7.70	7.58
1.0	4.9	7.25	7.09
W5 (mm)	L5 (mm)	Capacitance (pF)	Inductance (nH)
0.5	3.7	9.901	0.034
0.7	4.1	6.579	0.065
1.0	4.9	4.918	0.098

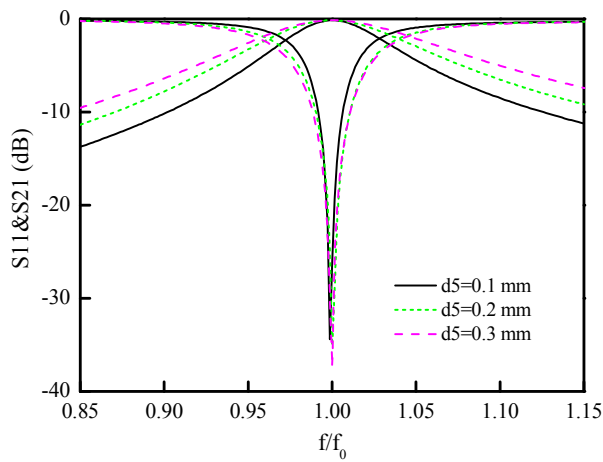


Fig. 4. Simulated frequency responses for varying d5 (W5=1.0 mm, L5=4.9 mm).

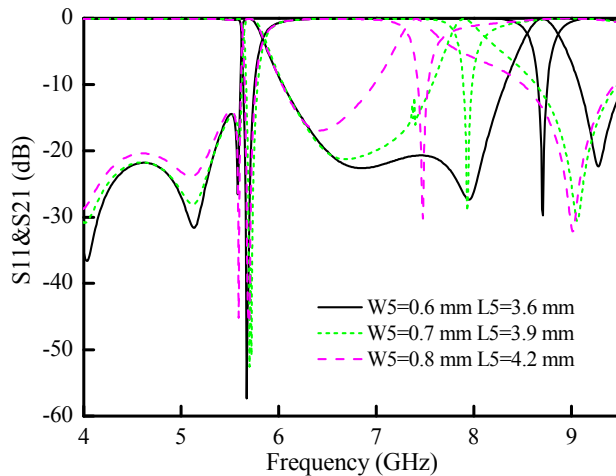


Fig. 5. Simulated frequency responses for varying W5 and L5 (L4=5.6 mm, W4=0.1 mm, d5=0.1 mm).

for simulations. The simulated results are plotted in Fig. 3. As the physical dimensions of the U-shaped slot increases, the equivalent capacitance decreases and the equivalent inductance increases, thus the resonance frequency slowly shifts to lower position due to the increased inductance. The circuit parameters of the equivalent circuit can be extracted [16]

$$C = \frac{\omega_c}{2Z_0} \cdot \frac{1}{\omega_0^2 - \omega_c^2} \quad (1)$$

$$L = \frac{1}{4\pi^2 f_0^2 C} \quad (2)$$

where ω_c is the 3-dB cutoff angular frequency, ω_0 is the resonance angular frequency, Z_0 is the characteristic impedance of the transmission line, and f_0 is the frequency of the attenuation pole location. Table 1 lists the circuit parameters of the equivalent circuit which are extracted from the simulated scattering parameters in Fig. 3. The bandwidth of the notched band can be controlled by the width of the gap, i.e., d_5 . Figure 4 shows the frequency responses with varying d_5 . It can be seen that the bandwidths are proportional to d_5 . Accordingly, the upper notched band can be achieved by properly tuning the dimensions of the proposed U-shaped slot, but the position of the lower notched band doesn't change as shown in Fig. 5.

III. SIMULATED AND MEASURED RESULTS

Based on the above study, a novel UWB bandpass filter with two controllable highly rejected notched bands is designed. One notched band is controlled by the loaded stub, and another one is determined by the U-shaped slot on the ground plane without increasing the total size of the filter. The dimensions for the UWB filter [referred to Figs. 1(a), 2(a)] are: W1=1.5 mm, W2=0.1 mm, W3=0.76 mm, W4=0.1 mm, W5=0.7 mm, L1=4.9 mm, L2=2.0 mm, L3=5.6 mm, L4=5.6 mm, L5=4.1 mm, d1=2.6 mm, d2= 0.1 mm, d3=0.1 mm, d4=0.1 mm, d5=0.1 mm. Simulation was accomplished using Ansoft HFSS, and measurement was carried out on an Agilent E8363B network analyzer. Figure 6 illustrates the simulated and measured frequency responses of the proposed filter. From this figure we can see

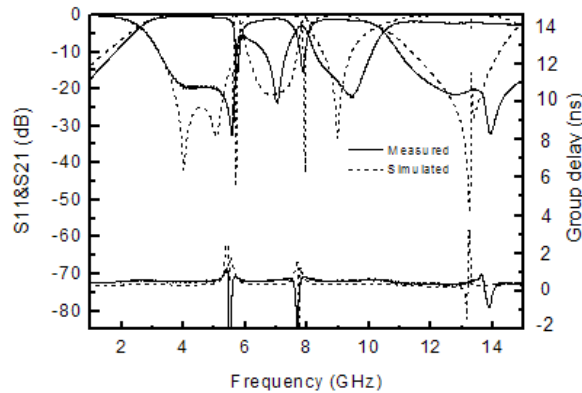


Fig. 6. Simulated and measured results.

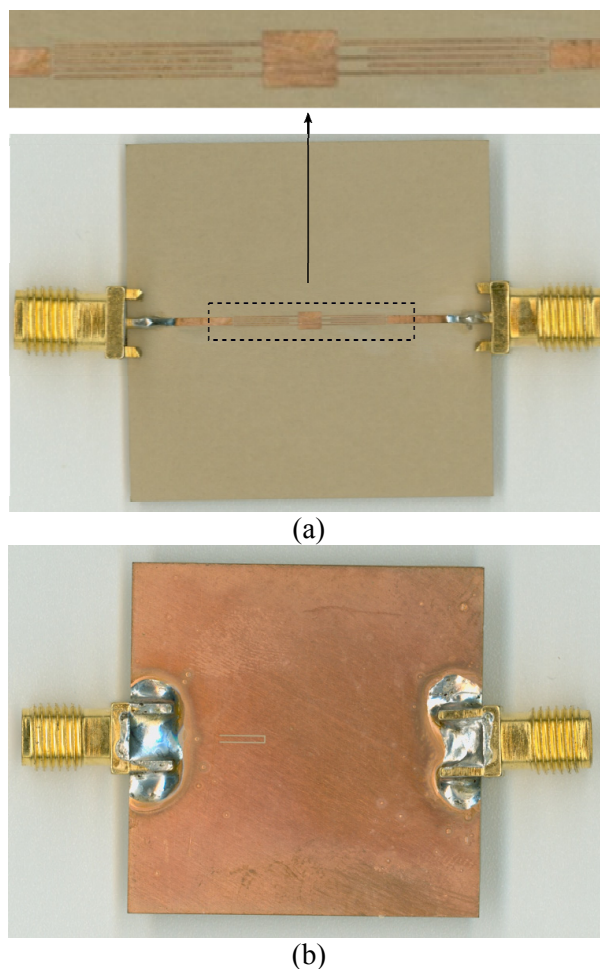


Fig. 7. Photograph of the fabricated UWB filter (a) top view, (b) bottom view.

that the measured passband is from 2.64 GHz to 10.27 GHz, and the two notched bands are centered at 5.74 GHz and 7.86 GHz, respectively.

The attenuations at the center of the notched bands are about -15.551 dB and -15.432 dB, respectively. Within the passbands, the return losses are below -10 dB. Meanwhile, there is a transmission zero located at 13.9 GHz, which realizes a good out-of-band rejection. The simulated and measured group delays are also shown in Fig. 6. It is seen that the measured group delays within the passbands are all less than 0.2 ns. The deviation between the simulated and measured results is mainly caused by SMA connectors and fabrication. Figure 7 displays the photograph of the fabricated UWB filter.

IV. CONCLUSION

A compact UWB bandpass filter with two controllable sharply rejected notched bands has been proposed in this letter. The UWB passband was realized by using the modified SIR and two interdigital feed-lines. Two notched bands at the desired frequencies within the UWB passband have been achieved by adopting the loaded stubs and U-shaped DGS without increasing the total size of the UWB filter. The proposed new UWB bandpass filter features compact size, easy fabrication, and is suitable for UWB wireless systems.

ACKNOWLEDGMENT

This work was in part supported by the Fundamental Research Funds for Central Universities under contract E022050205, in part by the National Natural Science Foundation of China under contract 60872034 and 60971029.

REFERENCES

- [1] Federal Communications Commission, "Revision of Part 15 of the Commission's Rules Regarding Ultra-Wideband Transmission Systems," Tech. Rep. ET Docket 98-153, FCC02-48, 2002.
- [2] A. Boutejdar, M. Challal, and A. Azrar, "A Novel Band-stop Filter Using Octagonal-shaped Patterned Ground Structures Along with Interdigital and Compensated Capacitors," *Applied Computational Electromagnetics Society (ACES) Journal*, vol. 26, no. 4, pp. 312-318, Apr. 2011.
- [3] G. E. Al-Omair and S. F. Mahmoud, A. S. Al-Zayed, "Lowpass and Bandpass Filter Designs Based on DGS with Complementary Split Ring Resonators," *Applied Computational Electromagnetics Society (ACES) Journal*, vol. 26, no. 11, pp. 907-914, Nov. 2011.

- [4] A. Eroglu and R. Smith, "Triple Band Bandpass Filter Design and Implementation using SIRs," *26th Annual Review of Progress in Applied Computational Electromagnetics (ACES)*, pp. 862-865, Tampere, Finland, Apr. 2010.
- [5] F. Karshenas, A. R. Mallahzadeh, and J. Rashed-Mohassel, "Size Reduction and Harmonic Suppression of Parallel Coupled-line Bandpass Filters using Defected Ground Structure," *Applied Computational Electromagnetics Society (ACES) Journal*, vol. 25, no. 2, pp. 149-155, Feb. 2010.
- [6] H. Ishida and K. Araki, "Design and Analysis of UWB Bandpass Filter with Ring Filter," *IEEE MTT-S Int Microwave Symp. Dig.*, vol. 3, pp. 1307-1310, Jun. 2004.
- [7] L. Zhu, S. Sun, and W. Menzel, "Ultra-wideband (UWB) Bandpass Filters Using Multiple-mode Resonator," *IEEE Microw. Wireless Compon. Lett.*, vol. 15, no. 11, pp. 796-798, Nov. 2005.
- [8] J. Gao, L. Zhu, W. Menzel, and F. Bogelsack, "Short-Circuited CPW Multiple-Mode Resonator for Ultra-wideband (UWB) Bandpass Filter," *IEEE Microw. Wireless Compon. Lett.*, vol. 16, no. 3, pp. 104-106, Mar. 2006.
- [9] F. Wei, C.-J. Gao, B. Liu, H.-W. Zhang, and X.-W. Shi, "UWB Bandpass Filter with Two Notched-bands Based on SCRLH Resonator," *Electron Lett.*, vol. 46, no. 16, pp. 1134-1135, Aug. 2010.
- [10] Q. Li, Z.-J. Li, C.-H. Liang, and B. Wu, "UWB Bandpass Filter with Notched Band Using DSR," *Electron Lett.*, vol. 46, no. 10, pp. 692-693, May 2010.
- [11] K. Song and Q. Xue, "Asymmetric Dual-line Coupling Structure for Multiple-notch Implementation in UWB Bandpass Filters," *Electron Lett.*, vol. 46, no. 20, pp. 1388-1389, Sep. 2010.
- [12] K. Song and Q. Xue, "Compact Ultra-wideband (UWB) Bandpass Filters with Multiple Notched Bands," *IEEE Microw. Wireless Compon. Lett.*, vol. 20, no. 8, pp. 447-449, Aug. 2010.
- [13] K. S. Ryu and A. A. Kishk, "UWB Antenna with Single or Dual Band-notched for Lower WLAN Band and Upper WLAN Band," *IEEE Trans. Antennas Propag.*, vol. 57, no. 12, pp. 3942-3950, 2009.
- [14] J. W. Jung, H. J. Lee, and Y. S. Lim, "Band Notched Ultra Wideband Internal Antenna for USB Dongle Application," *Microw. Opt. Technol. Lett.*, vol. 50, no. 7, pp. 1789-1793, 2008.
- [15] S. Gao, S. Xiao, and B.-Z. Wang, "Ultrawideband Bandpass Filter with a Controllable Notched Band," *Microw. Opt. Technol. Lett.*, vol. 51, no. 7, pp. 1745-1748, Jul. 2009.
- [16] D. Ahn, J. S. Park, C. S. Kim, Y. Qian, and T. Itoh, "A Design of the Low-pass Filter using the Novel

Microstrip Defected Ground Structure," *IEEE Trans. Microwave Theory Tech.*, vol. 49, pp. 86-93, Jan. 2001.



Shanshan Gao was born in Sichuan Province, China. She received the M.S. degrees in radio physics from the University of Electronic Science and Technology of China (UESTC), Chengdu, in 2008, and is currently working towards the Ph.D. degree in radio physics at UESTC. Her research interests include design and implementation of microwave passive devices for ultra-wideband wireless communication systems.



Shaoqiu Xiao received the Ph.D. degree in electromagnetic field and microwave engineering from the University of Electronic Science and Technology of China (UESTC), Chengdu, in 2003. From January 2004 to June 2004, he was with UESTC as an Assistant Professor.

From July 2004 to March 2006, he was with the wireless Communications Laboratory, National Institute of Information and Communications Technology of Japan (NICT), Singapore, as a Researcher with a focus on the planar antenna and smart antenna design and optimization. From July 2006 to June 2010, he was with UESTC as an Associate Professor. He is now a Professor with UESTC. His current research interests include microwave passive circuits, planar antenna and arrays, and electromagnetics in ultra-wideband wireless communication. He has authored/coauthored more than 100 technical journals, conference papers, books, and book chapters.



Jia-Lin Li was born in Yibin, Sichuan Province, China. He received the M. S. degree from the University of Electronic Science and Technology of China (UESTC), Chengdu, China, in 2004, and the Ph. D. degree from the City University of Hong Kong,

Hong Kong, in 2009, both in electronic engineering. From September 2005 to August 2006, he was a Research Associate with the Wireless Communication Research Center, City University of Hong Kong, Hong Kong. Since September 2009, he has been with the Computational Electromagnetics Laboratory (CEMLab), Institute of Applied Physics, School of Physical Electronics, UESTC, where he is currently a Professor

of Radio Physics. His research interests include the high performance active/passive microwave/millimeter-wave antennas, circuits and systems realized on PCB, multilayer PCB, LTCC, etc.

Dr. Li received the Outstanding Performance Award for Research Degree Students in the Academic Year 2007-2008 from the City University of Hong Kong, and the APMC Champion at the 2008 Asia-Pacific Microwave Conference.

Compact Microstrip-fed Monopole Antenna with Modified Slot Ground Plane for UWB Applications

Maryam Majidzadeh¹ and Changiz Ghobadi²

¹ Department of Electrical Engineering
Urmia University, Urmia, Iran
Maryam_majidzadeh37@yahoo.com

² Department of Electrical Engineering
Urmia University, Urmia, Iran
Ch.Ghobadi@urmia.ac.ir

Abstract — A novel UWB microstrip-fed monopole antenna with modified structure has been designed and analyzed. The main body of the antenna under consideration consists of a quasi square radiating patch with tapered steps and a modified slotted ground plane. Due to the repeatedly cutting of three notches on the radiating patch and also inserting a rectangular slot and three tapered steps on the ground plane, a new resonance is excited and a wide bandwidth is obtained. By applying two sleeves with proper sizes to the antenna structure, an even wider impedance bandwidth is achieved. The antenna has a compact size of $18 \times 12 \times 1.6 \text{ mm}^3$ and operates over the frequency range of 2.34 – 21.43 GHz (9.15:1; 160%). The impedance bandwidth improvement process of the proposed antenna is presented and discussed in detail.

Index Terms — Microstrip feed line, UWB antenna, wide impedance bandwidth.

I. INTRODUCTION

Printed monopole antennas, although known for many years, are still at the center of the attention of the communication experts. Interest in these antennas is basically due to their marvelous merits such as low profile, easy and cost-effective fabrication process and good radiation properties. Equipped with such admirable characteristics, printed monopole antennas have provided a challenging opportunity for antenna designers in

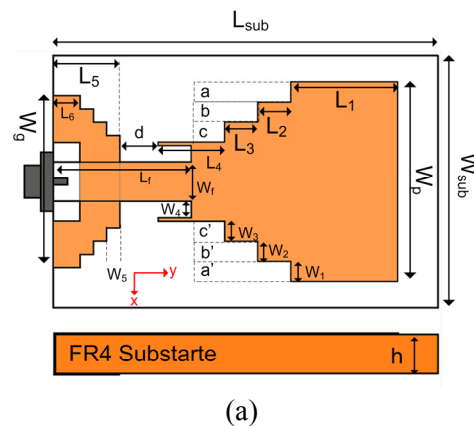
designing novel antennas satisfying UWB requirements. The main drawback to be considered in the antenna design realm is the problem of inherent narrow bandwidth. There has been a vast variety of literature conducted on the design of antennas operating over the UWB frequency range. Different combinations of radiating patch, feed line, and ground plane structures have been introduced to widen the antenna impedance bandwidth. For instance in [1], a square radiating patch with rectangular slots and a ground plane with an inverted T-shaped notch is introduced. A new band enhancement technique, chosen to design an antenna with UWB characteristics is proposed in [2]. An UWB antenna with an inverted T-shaped slot on its radiating patch and an inverted T-shaped conductor on the back plane of the substrate is proposed in [3]. The antenna presented in [4] is a hook shaped antenna with multi branch radiator. An antenna with elliptical/circular slots with U-shaped tuning stub and tapered microstrip feed line, is the structure adopted in [5] to reach the UWB characteristics. The antenna in [6] is a cross slot antenna with U-shaped tuning stub which is designed for UWB applications. In [7], a simple rectangular radiating patch with a ladder shaped conductor on the back plane is excited by a microstrip feed line. By introducing a tapered slot to the antenna structure in [8], UWB performance is obtained. Another antenna with elliptic patch and a hexagonal slot etched from the ground plane on the other side of the substrate is presented in [9]

and provides an impedance bandwidth of 145%. An antenna with tapered-shaped slot and a rectangular tuning stub for UWB systems is offered in [10]. Fractal geometries are also used in the design of UWB antennas. Behavior of a Sierpinski carpet monopole antenna is analyzed in [11]. Also, in [12] a novel UWB antenna is offered which rejects WiMAX and WLAN bands. In this paper, a novel compact microstrip-fed monopole antenna is presented. The proposed antenna has a very compact size of $18 \times 12 \times 1.6 \text{ mm}^3$ and operates over the frequency range of 2.34-21.43GHz (160%). The antenna benefits from a novel shape of ground plane structure and radiating patch. Omnidirectional radiation pattern and constant gain is observed over the UWB frequency range. As mentioned earlier, the proposed antenna, besides covering the UWB frequency range, has a good performance at higher frequencies ranging from 11-21.43GHz. This feature is a salient merit which makes this antenna to be a good candidate in satellite communications [13]. The remainder of the paper is outlined as follows: The structure and design process of the antenna are discussed in Section II. The simulation results of parametric study, measured results and the comparison of the antenna performance with some of the recently published antennas are presented in Section III. Eventually, Section IV concludes the paper.

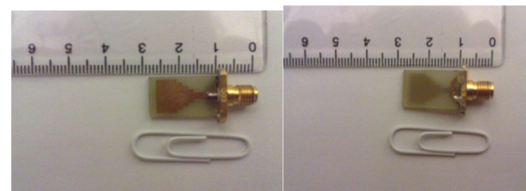
II. ANTENNA DESIGN

The schematic of the proposed monopole antenna is shown in Fig. 1.a. The fabricated antenna is shown in Fig. 1.b. The proposed antenna is printed on a cheap FR4-epoxy substrate with permittivity of 4.4, loss tangent of 0.002 and thickness of 1.6 mm. A microstrip feed line with the length and width of 6mm and 2mm, respectively, is adopted to feed the study antenna. What makes this antenna distinctive from the conventional printed monopole antennas is the modified structure of its ground plane and the inclusion of two sleeves on the lowest edges of the radiating patch. The radiating element is basically a $10 \times 10 \text{ mm}^2$ square on which three notches named as (a, a'), (b, b'), and (c, c') are cut. In the main square patch without notches, the sudden discontinuity between the feed line and the patch, leads to narrow bandwidth and degraded radiation pattern. To overcome the mentioned problem, the notches are embedded on the radiating patch. As it will be

shown later, due to the removing of the mentioned rectangular symmetrical notches from the patch, the bandwidth of the antenna is remarkably enhanced. Two sleeves with dimensions of $1.5 \times 0.1 \text{ mm}^2$ are added to the edges of the lowest steps of the radiating patch to further widen the bandwidth. The proposed antenna benefits from a new shape of ground plane. A rectangular slot with length and width of $4 \times 1.5 \text{ mm}^2$ is removed from the lowest part of the ground plane. This slot, along with three tapered steps, plays an important role in the antenna performance. The values of all the antenna parameters are given in detail in Fig. 1.



(a)



(b)

Fig. 1(a). The schematic geometry of the proposed antenna, (b) The fabricated antenna. $W_{\text{sub}}=12$, $L_{\text{sub}}=18$, $W_f=2$, $L_f=6$, $L_1=5.5$, $L_2=1.5$, $L_3=1.5$, $L_4=3$, $L_5=3$, $L_6=1.5$, $W_1=1$, $W_2=1$, $W_3=1$, $W_4=0.9$, $W_5=0.5$, $W_g=8$, $h=1.6$ (Unit: mm).

III. RESULTS AND DISCUSSIONS

The performance of the monopole antenna has been investigated using the Ansoft High Frequency Structure Simulator (HFSS v. 11). The impedance bandwidth, VSWR, gain and radiation patterns of the proposed antenna are measured and analyzed. All the measured results are obtained using the Agilent 8722ES network analyzer. An exhaustive parametric study is conducted to verify

the effect of different parameters on the performance of the proposed antenna.

A. Ground plane effect

At first, for explaining the effect of the ground plane, four prototypes of proposed antenna (Ant. 1- Ant. 4), with different shapes of ground planes are defined as follows: Antenna 1, includes only a ground plane without any slots on it, with the width and length of $W_{sub} = W_g = 12\text{mm}$ and $L_s = 3\text{mm}$ respectively; in Antenna 2, two rectangular slots are cut from both sides of the conventional rectangular ground plane. In Antenna 2, the ground width is reduced to $W_g = 8\text{mm}$ while its length is kept at $L_s = 3\text{mm}$. Antenna 3, contains a rectangular slot with dimensions of $4\text{mm} \times 1.5\text{mm}$ inserted on the ground (π -shape); and finally the Antenna 4, exhibits the modified ground plane proposed in this paper. The VSWR curves for the Antenna 1 to Antenna 4 are depicted in Fig. 3. These results confirm that both lower and upper band edge frequencies are sensitive to the ground plane shape and have shifted toward lower and higher frequencies respectively, which results in bandwidth improvement, especially at higher frequencies.

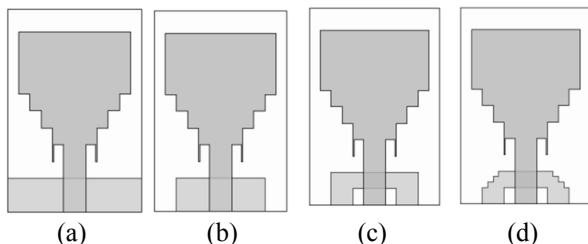


Fig. 2. The geometry of the four prototypes of the proposed antennas. (a) Antenna 1, (b) Antenna 2, (c) Antenna 3, a (d) Antenna 4 (proposed antenna).

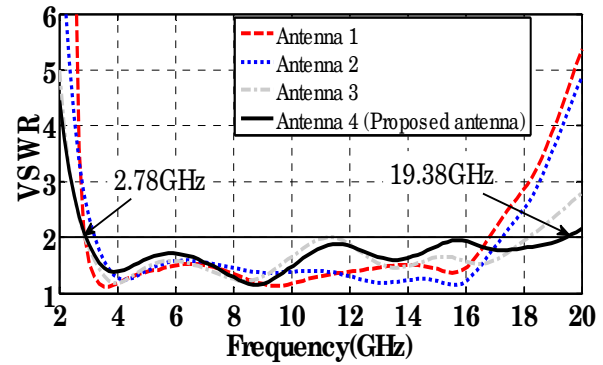


Fig. 3. Simulated VSWR curves for the antennas presented in Fig. 2.

B. Rectangular notches on the radiating patch

As it was mentioned earlier, three symmetrical rectangular slots on the patch are the other elements affect the antenna impedance bandwidth. When there is no notch on the radiating patch, the current encounters a sharp point on its path, but when the current flow path is smoothed by the notches, the impedance matching and the bandwidth are enhanced. Three pairs of notches named as (a, a'), (b, b'), and (c, c') are repeatedly applied to the antenna structure. Figure 4 shows the embedding of notches on the patch. Antenna in Fig. 4.a includes only a pair of notch named as (a, a'). In Fig. 4.b, notches (a, a'), (b, b') are added to the antenna structure. In Fig. 4.c, the antenna has three pair of rectangular notches, and finally in Fig. 4.d, the sleeves are also applied to the antenna and the final configuration is obtained. VSWR curves for the antennas presented in Fig. 4 are plotted in Fig. 5. The simulated results show that repeatedly embedded notches on the patch directly influence both the upper and lower band edge frequencies. The impedance bandwidth enhancement process is clearly seen in Fig. 5. Due to the adding of two sleeves to the lowest steps of the radiating patch, a new resonance is excited. By the appearance of this resonance, at the frequency of about 17.5GHz even wider frequency band is covered by the proposed antenna.

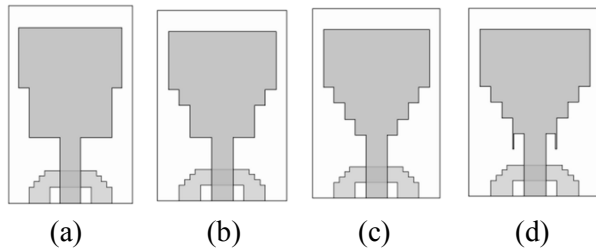


Fig. 4. (a): Antenna with notches (a, a'). (b): Antenna with notches (a, a'), (b, b'). (c): Antenna with notches (a, a'), (b, b'), (c, c'). (d): Proposed antenna.

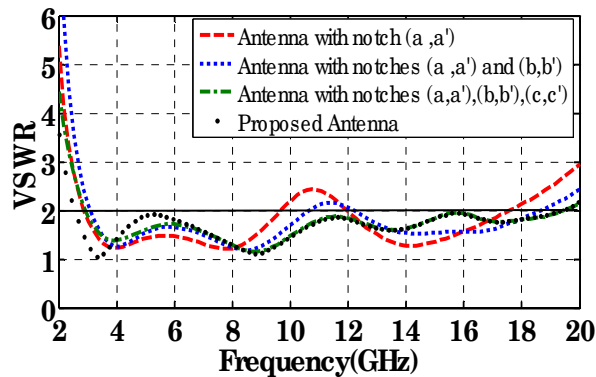


Fig. 5. Simulated VSWR curves for the effect of the notches on the patch.

C. Feed gap distance (d)

The other parameter to be studied is the distance between the upper edge of the ground plane and lower edge of the radiating patch which is named as 'd'. The antenna is analyzed with three different values for d and the results are shown in Fig. 6. It is seen that when d is decreased from the initial value of 2.5 mm, by a step of 1mm, the impedance matching becomes poor and results in bandwidth reduction. From the VSWR curves, for d=1.5 mm, the widest bandwidth is achieved.

The measured VSWR curve for the proposed antenna is depicted in Fig. 7 and is compared to the simulated results. The measured results indicate that the impedance bandwidth is stretched from 2.34 to 21.43 GHz (160%) for VSWR<2. As it is seen, four resonances are excited in the VSWR curve of the proposed antenna, which are shown in Fig. 7. To provide a better understanding of the antenna performance, Fig. 8 shows the surface current distribution at the resonance frequencies of 3.7, 8.7, 13.5, and 17 GHz.

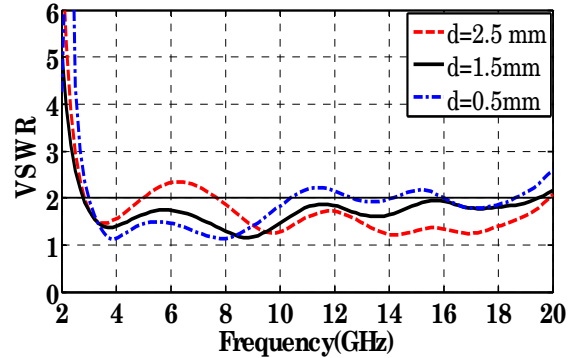


Fig. 6. Simulated VSWR curves for different parameters of 'd'.

As it is seen from Fig. 8. a, at 3.7 GHz, where the first resonance is excited, the majority of the current is concentrated around the edges of the rectangular slot on the ground plane, sleeves, and the lowest step of the patch. It shows that the sleeves and the steps on the patch are important elements in determining the antenna performance at this frequency. In Fig. 8.b, the current distribution at 8.7 GHz is shown. Strong current distribution on the edges of the rectangular slot shows that this part of the ground plane can be considered as a part of the radiating element. It is observed from Fig. 8.c that at 13.5 GHz, the current concentration is stronger on the edges of the two lower steps of the radiating patch and also on the edges of the rectangular ground plane slot which confirms that the rectangular notch significantly affects the bandwidth. The surface current distribution around the fourth resonance frequency (17 GHz), is shown in Fig. 8.d. Here, most of the current is concentrated at the lowest steps and sleeves. From the current distribution at resonance frequencies, it can be deduced that the sleeves and rectangular slot on the ground plane, have the most influence on the antenna bandwidth.

A comparison of the performance of the proposed antenna and some of the recently published antennas is done in Table 1. According to the results, the antenna in this work has the same size in [1] and [3] but it covers 40% and 30% wider bandwidth, respectively. The proposed antenna in this paper occupies a smaller area than the antennas in [5] and the antennas in [7] to [10]. Although having a smaller size, it covers a larger frequency band which make it a very suitable choice to be used in communication systems. The antenna in [4] has a smaller size respect to the

present work, but it has 47.6% narrower bandwidth than the antenna presented in this work.

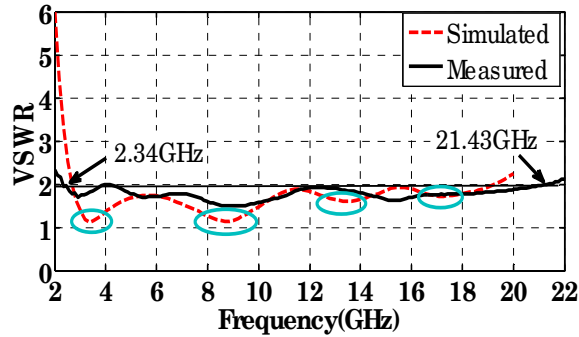


Fig. 7. Simulated and measured VSWR curves for the proposed antenna.

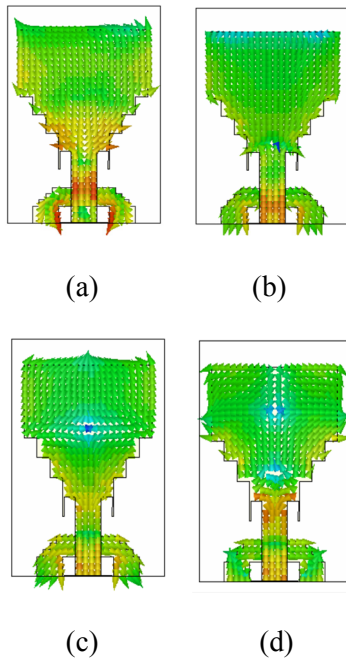


Fig. 8. Current distributions at (a)3.7 GHz, (b)8.7 GHz, (c) 13.5 GHz, (d) 17 GHz.

For the fabricated antenna, a low level group delay is obtained in the measurement process that is shown in Fig. 9, which makes the proposed antenna a suitable candidate for UWB applications.

Apart from the VSWR curves, the gain and radiation efficiency of the proposed antenna are measured and analyzed. The measured peak gain in dB is plotted in Fig. 10. A nearly constant gain is observed for the antenna over the operating frequency range. Gain values are between 1 and

2.3 dBi over the wide operating band of 2.34-21.43 GHz.

Table 1: Comparison of the performance of the proposed antenna and some of the recently published antennas

Ant.	Size	BW	Area Reduction	BW Increment
Ant in [1]	18×12×1.6	3.2-12.73	0	40%
Ant in [3]	18×12×1.6	2.91-14.1	0	30%
Ant in [4]	10×10×1.6	3-10.7	-53.7%	47.6%
Ant in [5]: circular	50×43×1.5	3.46-10.9	8%	56.4%
Ant in [5]: elliptical	42×42×1.5	2.6-10.22	86.9%	41%
Ant in [7]	22×22×1.6	2.7-20	55.37%	7.57%
Ant in [8]	29×26×1	2.91-12	54.1%	38%
Ant in [9]	30×30×1.6	2.9-18	76%	15%
Ant in [10]	24×22×1.6	3-11.2	59%	44.5%
Ant in this work	18×12×1.6	2.34-21.43	-----	-----

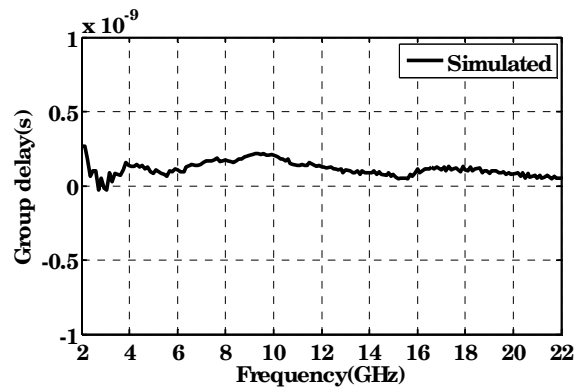


Fig. 9. Simulated group delay of the proposed antenna.

Simulated and measured radiation efficiency are plotted in Fig. 11. As it is seen a radiation efficiency of around 80% is obtained for the fabricated antenna.

Simulated and measured radiation patterns at H-plane (xz plane) and E plane (yz plane) are also plotted in Fig. 12. 3GHz, 8GHz, 11GHz, and 20 GHz are selected as sample frequencies over the operating frequency range. Good agreement is observed between the simulated and measured results. As it is expected an omnidirectional pattern is obtained on H-plane and two nulls are appeared in the radiation patterns of E-plane, which is suitable for UWB applications.

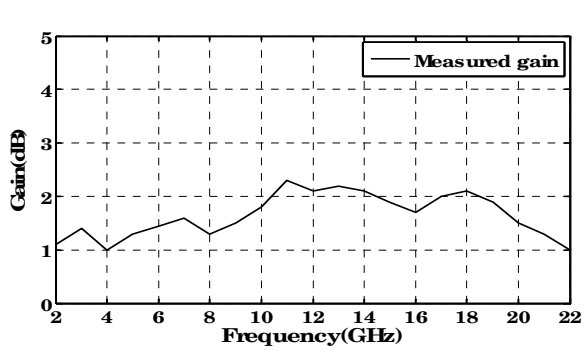


Fig. 10. Measured gain of the proposed antenna.

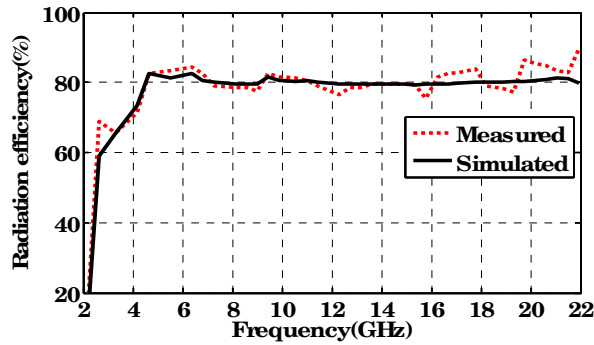


Fig. 11. Measured and simulated radiation efficiency for the proposed antenna.

IV. CONCLUSION

A novel microstrip-fed monopole antenna with modified structure is presented for UWB applications. The antenna is printed on a $18 \times 12 \times 1.6 \text{ mm}^3$ cheap FR4 substrate. The bandwidth of the antenna is stretched from 2.34 to 21.43GHz (160%). The novel ground plane shape along with the modified radiating patch makes this antenna distinctive from the other microstrip antennas. Characteristics such as compact size, low profile, low cost, good impedance matching, omnidirectional pattern, and wider bandwidth respect to the previously designed antennas, make this antenna a beneficial choice for UWB applications.

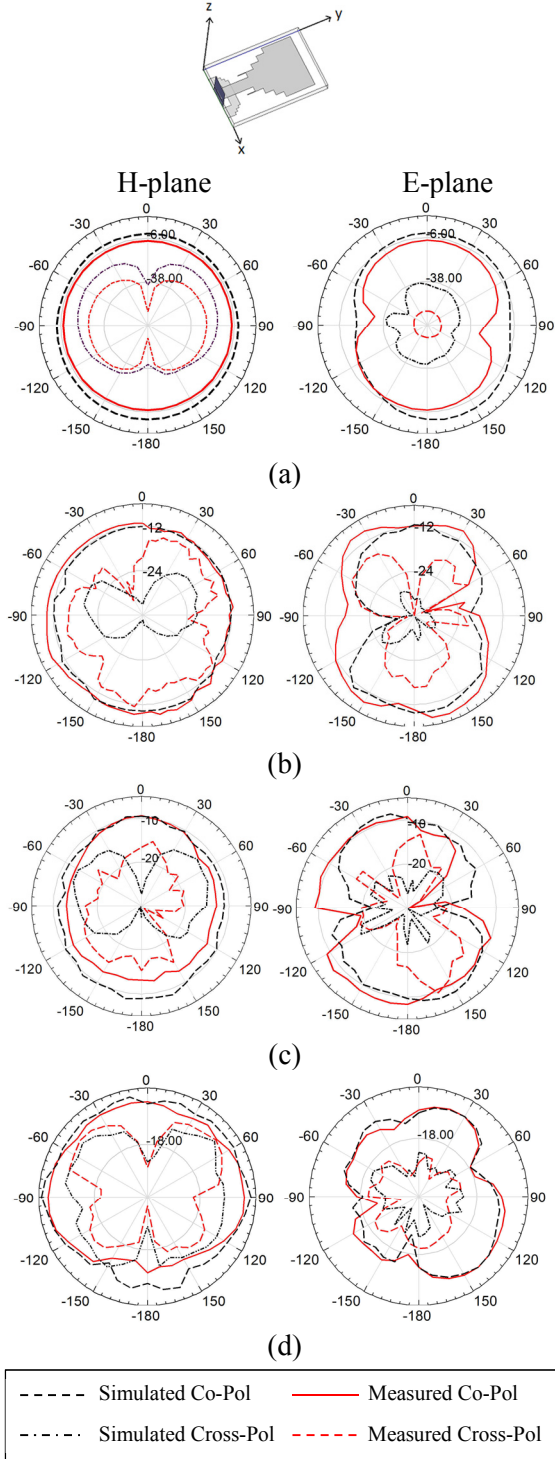


Fig. 12. Measured radiation patterns for the proposed antenna: (a) 3 GHz, (b) 8 GHz, (c) 11 GHz, (d) 20 GHz at H-plane (xz plane) and E-plane (yz plane).

REFERENCES

- [1] M. Ojaroudi, C. Ghobadi, and J. Nourinia, "Small Square Monopole Antenna with Inverted T-Shaped Notch in the Ground Plane for UWB Supplication," *Antennas and Wireless Propagation Letters, IEEE*, vol. 8, pp. 728-731, 2009.
- [2] R. Azim, M. T. Islam, and N. Misran, "Design of a Planar UWB Antenna with New Band Enhancement Technique," *Applied Computational Electromagnetics Society (ACES) Journal*, vol. 26, no. 10, pp. 856-862, October 2011.
- [3] M. Ojaroudi, S. Yazdanifard, N. Ojaroudi, and M. Naser-Moghaddasi, "Small Square Monopole Antenna with Enhanced Bandwidth by Using Inverted T-Shaped Slot and Conductor-Backed Plane," *IEEE Trans. Antennas Propagat.*, vol. 59, no. 2, pp. 670-674, February 2011.
- [4] H.-W. Liu, and C.-F. Yang, "Miniature Hook-Shaped Monopole Antenna for UWB Applications," *Electronics Letters*, vol. 46, no. 4, pp. 265-266, February 2010.
- [5] L. Pengcheng, L. Jianxin, and Ch. Xiaodong, "Study of Printed Elliptical/Circular Slot Antennas for Ultrawideband Applications," *IEEE Trans. Antennas Propagat.*, vol. 54, no. 6, pp. 1670- 1675, June 2006.
- [6] D. S. Javan, and O. H. Ghouchani, "Cross Slot Antenna with U-Shaped Tuning Stub for Ultra Wideband Applications," *Applied Computational Electromagnetics Society (ACES) Journal*, vol. 24, no. 4, pp. 427-432, August 2009.
- [7] R. A. Sadeghzadeh-Sheikhan, M. Naser-Moghaddasi, E. Ebadifallah, H. Roustaa, M. Katouli, and B. S. Virdee, "Planar Monopole Antenna Employing Back-Plane Ladder-Shaped Resonant Structure for Ultra-Wideband Performance," *Microwaves, Antennas & Propagation, IET*, vol. 4, no. 9, pp. 1327-1335, September 2010.
- [8] W. J. Lui, C. H. Cheng, and H. B. Zhu, "Experimental Investigation on Novel Tapered Microstrip Slot Antenna for Ultra-Wideband Applications," *Microwaves, Antennas & Propagation, IET*, vol. 1, no. 2, pp. 480-487, April 2007.
- [9] M. R Ghaderi and F. Mohajeri, "A Compact Hexagonal Wide-Slot Antenna with Microstrip-Fed Monopole for UWB Application," *Antennas and Wireless Propagation Letters, IEEE*, vol. 10, pp. 682-685, 2011.
- [10] R. Azim, M. T. Islam, and N. Misran, "Compact Tapered-Shape Slot Antenna for UWB Applications," *Antennas and Wireless Propagation Letters, IEEE*, vol. 10, pp. 1190-1193, 2011.
- [11] M. Naghshvarian-Jahromi and N. Komjani-Barchloui, "Analysis of the Behavior of Sierpinski Carpet Monopole Antenna," *Applied Computational Electromagnetics Society (ACES) Journal*, vol. 24, no. 1, pp. 32-36, February 2009.
- [12] J. William and R. Nakkeeran, "A New UWB Slot Antenna with Rejection of WiMax and WLAN Bands," *Applied Computational Electromagnetics Society (ACES) Journal*, vol. 25, no. 9, pp. 787-793, September 2010.
- [13] L. Ch. Godara, *Handbook of Antennas in Wireless Communications*, CRC 2002.



Maryam Majidzadeh was born on 18 September, 1987 in Urmia, Iran. She received her B.S. degree in Electrical Engineering from Urmia University, Iran in 2009 and is currently an M.Sc. student in Electrical Communication

Engineering at the same university. Her research interests are in designing of UWB antenna, antenna miniaturization, and impedance bandwidth enhancement techniques.



Changiz Ghobadi was born on 1 June, 1960 in Iran. He received the B.S. degree in Electrical and Electronic Engineering and M.S. degree in Electrical and Telecommunication Engineering from Isfahan University of

Technology, Isfahan, Iran and Ph.D. degree in Electrical-Telecommunication from University of Bath, Bath, UK in 1998. From 1998 he was an Assistant Professor and now is Associated Professor in the Department of Electrical Engineering, of Urmia University, Urmia, Iran. His primary research interests are in antenna design, radar and adaptive filters.

Compact Microstrip Low-Pass Filter Design with Ultra-Wide Reject Band using a Novel Quarter-Circle DGS Shape

Mouloud Challal¹, Ahmed Boutejdar², Mokrane Dehmas¹, Arab Azrar¹, and Abbas Omar²

¹ Department of Electronic, Institute of Electrical & Electronics Engineering
University of Boumerdes, Boumerdes, 35000, Algeria
mchallal@umbb.dz

² Chair of Microwave and Communication Engineering
University of Magdeburg, Magdeburg, 39106, Germany
Ahmed.Boutejdar@ovgu.de

Abstract — A novel quarter-circle defected ground structure shape is introduced in this paper to design and implement an ultra-wide reject band low-pass filter (LPF). Moreover, an equivalent circuit model (ECM) is presented. The proposed LPF has small size and a low insertion loss and a return loss less than -20 dB. Also, a round -20 dB suppression level ranging from 4 GHz to more than 20 GHz is achieved. The simulated results obtained by ECM and full-wave EM show good agreement with the measured ones.

Index Terms — Compensated microstrip line, defected ground structure (DGS), low-pass filter (LPF), quarter-circle (QC) shape.

I. INTRODUCTION

Recently, there has been an important and an increasing interest in the use of defected ground structures (DGSs) for performance improvement of microstrip filters [1-11]. A DGS unit is realized by etching off a simple shape defect from the ground plane. The structure shape can have a simple or a complicated geometry. An etched defect disturbs the shield current distribution in the ground plane. This disturbance modifies the transmission line characteristics (capacitance and inductance) and achieves slow-wave effect and band-stop property. Due to its resonant behavior, this may be compared to the simple and widely used LCR equivalent circuit model.

Usually, DGSs can offer both slow-wave (SW) propagation in the pass-band and good attenuation properties in the stop-band. Consequently, low-pass filters (LPFs) designs based on DGS with broad stop-band have been attracting researchers in latest years. Various DGS shapes for filters applications have been proposed [1-11]. Nevertheless, usually the filters' performances do not completely achieve the communication systems requirements such as compact size, ultra-wide stop-band width and low insertion loss.

In this paper, we propose a novel quarter-circle (QC) DGS shape for stop-band filter design. It shows an upper-stopband and good SW properties. A single QC-DGS generates an attenuation pole frequency which can be simply designed with structural parameters. Its equivalent circuit model (ECM) is analyzed and discussed. Furthermore, a compact ultra-wide stop-band LPF using only two QC-DGS along with compensated line is proposed. This structure type avoids employment of cascaded LPF units and allows achievement of an ultra-wide stop-band with very good insertion and return losses in the LPF pass-band. The simulation results show a good agreement to the measurement ones.

II. QC-DGS UNIT ANALYSIS AND EQUIVALENT CIRCUIT MODEL

Figure 1 shows the proposed QC-DGS pattern with its equivalent circuit model. It is composed of

a connecting slot and two quarter-circle defected areas etched in the ground plane below a 50 Ω microstrip line. The QC-DGS unit is designed on a RO4003 substrate with a permittivity of the dielectric (ϵ_r) of 3.38 and a thickness (h) of 0.813 mm. The calculated width (w) of a 50 Ω microstrip line is 1.92 mm.

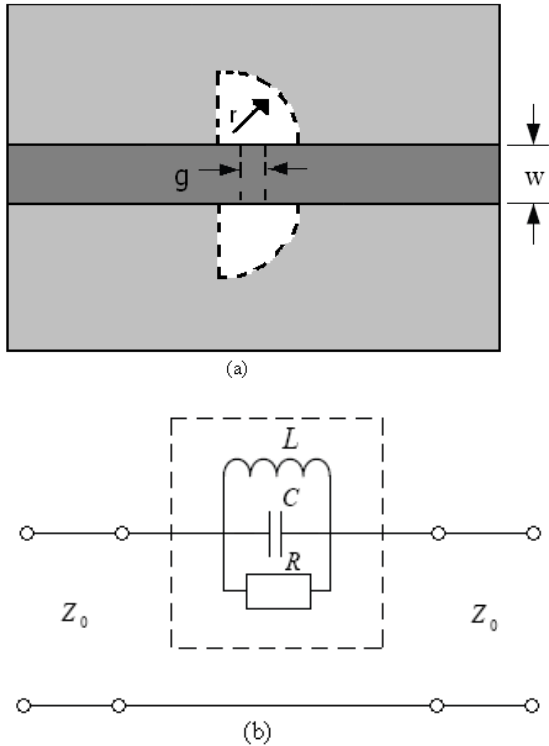


Fig. 1. The proposed of QC-DGS unit (a) geometry, and (b) equivalent circuit model (ECM).

The proposed QC-DGS pattern dimensions r and g are considered to be respectively 5 mm and 2.5 mm and the circuit elements are extracted using the following expressions [12].

$$C = \frac{\omega_0}{2Z_0(\omega_0^2 - \omega_c^2)}, \tag{1}$$

$$L = \frac{1}{\omega_0^2 C}, \tag{2}$$

$$R = \frac{2Z_0}{\sqrt{\frac{1}{|S_{11}(\omega_0)|^2} - (2Z_0(\omega_0 C - \frac{1}{\omega_0 L}))^2 - 1}}, \tag{3}$$

where $\omega_0 (= 2\pi f_0)$ and $\omega_c (= 2\pi f_c)$ are respectively

the angular resonant and 3-dB cutoff frequencies of the DGS pattern.

For the assumed ECM, the parameters C , L , and R are respectively 0.065 pF, 3.17 nH and 1.40 kΩ. The structure is investigated using the full-wave EM IE3D simulator. ECM and EM simulations results are illustrated in Fig. 2 which shows the characteristics of a one-pole LPF with a pole frequency (f_0) at 11 GHz and a 3-dB cutoff frequency (f_c) at 4.26 GHz. It can be observed from Fig. 2 that a broad-stop-band from 8 GHz (-10 dB) to more than 20 GHz is achieved.

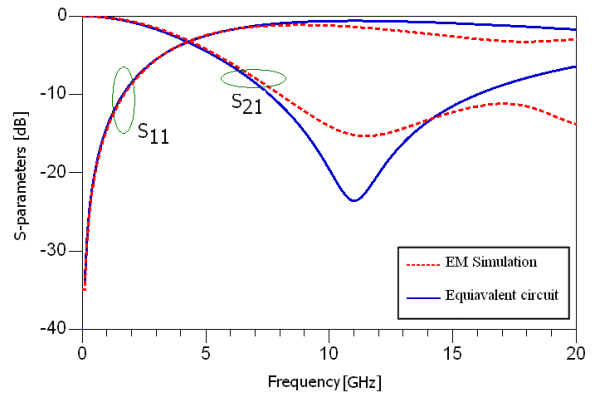


Fig. 2. Equivalent circuit model and EM-Simulations of the proposed QC-DGS pattern with $r=5$ mm, $g=2.5$ mm and $w=1.92$ mm.

In order to investigate the effect of the parameters r and g on the filter performances, the proposed QC-DGS unit is simulated with different r and g . First, the radius r is set successively to 3 mm, 4 mm, 5 mm, and 6 mm keeping g fixed. Next, g is set to 0.2 mm, 1 mm, 2 mm, and 2.5 mm keeping r fixed.

The simulated S-parameters are plotted in Fig. 3 and Fig. 4. It is observed that the pole frequency of the stop-band is affected significantly by both r and g . As the radius r of the proposed QC-DGS increases the pole location and cutoff frequencies move down to lower levels as shown by Fig. 3. When g increases (Fig. 4), the pole location frequency increases while the cutoff frequency remains fixed. Therefore, the proposed QC-DGS presents the significant advantage of controlling easily the pass-band and stop-band characteristics by adjusting only the parameters r and g . The pole and cutoff frequencies are plotted against r and g in Fig. 5 and Fig. 6, respectively.

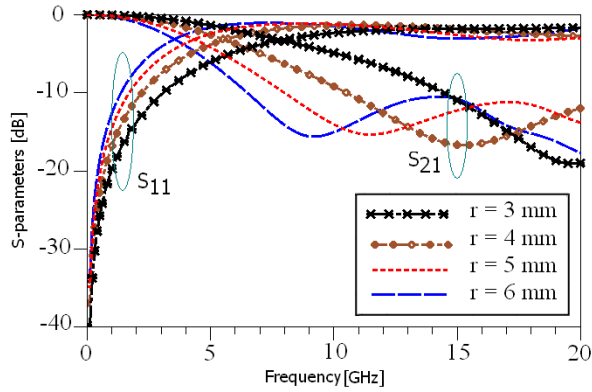


Fig. 3. S-parameters of the proposed QC-DGS cell for different r (g = 2.5 mm).

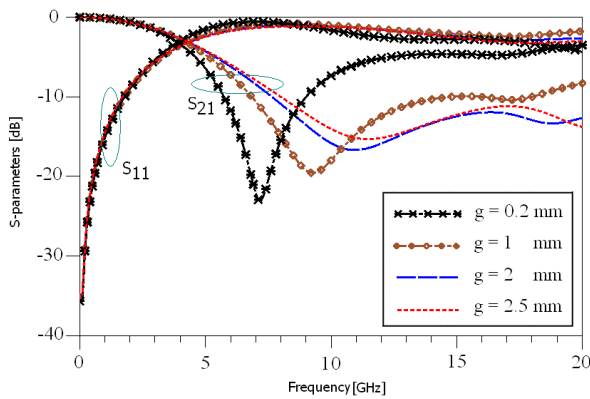


Fig. 4. S-parameters of the proposed QC-DGS cell for various g (r = 5 mm).

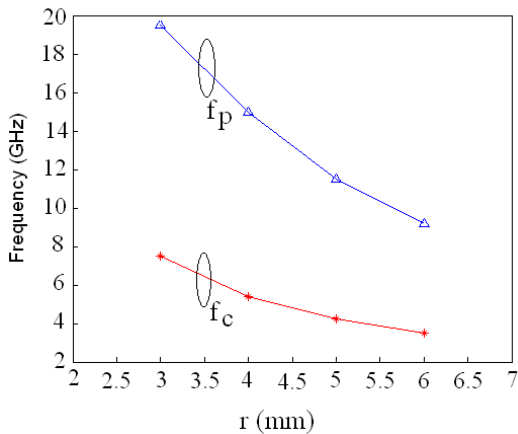


Fig. 5. Pole frequency (f_p) and cutoff frequency (f_c) versus r (g=2.5 mm).

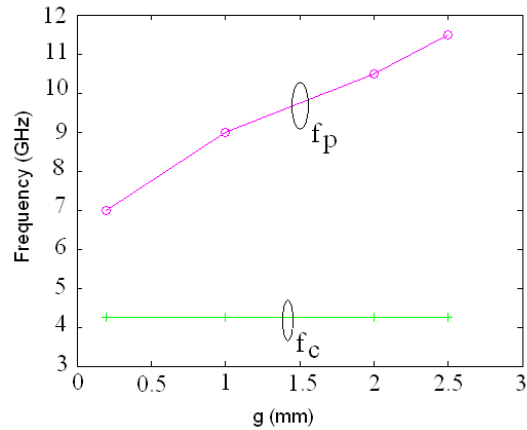


Fig. 6. Pole frequency (f_p) and cutoff frequency (f_c) versus g (r=5 mm).

In order to improve the performance of the proposed QC-DGS, a compensated 25-Ω microstrip line (w₁ = 4.93 mm) is added as shown in Fig. 7. ECM and full-wave EM simulations results are depicted in Fig. 8. It is observed that Fig. 8 shows the validity of the ECM for the proposed structure. In addition, a LPF response with upper-stopband and satisfactory SW properties is achieved.

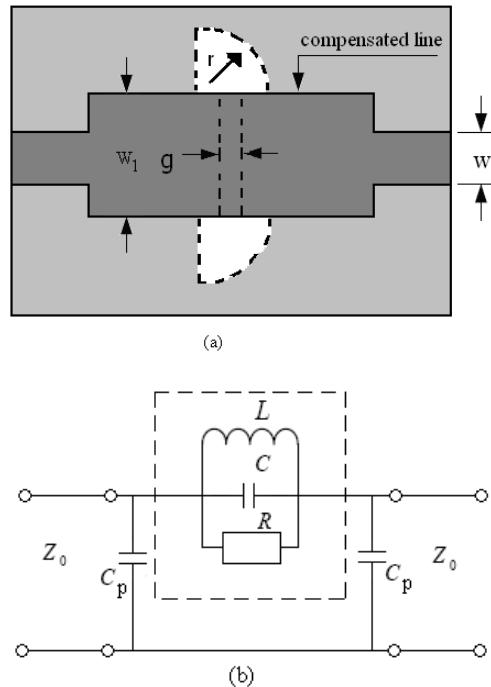


Fig. 7. Proposed of QC-DGS unit with compensated microstrip line (a) geometry and (b) equivalent circuit model (C_p= 0.562 pF).

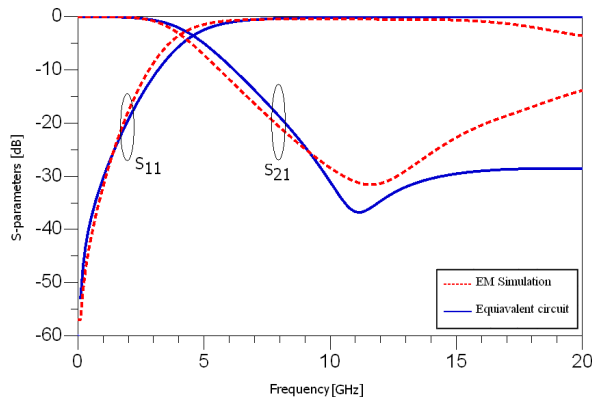


Fig. 8. Circuit and EM-simulations of the proposed QC-DGS cell with compensated line ($r=5$ mm, $g=2.5$ mm and $w_1=4.93$ mm).

III. FIELD DISTRIBUTION IN THE DGS-UNIT

The goal of this DGS unit investigation is to try to prove the validity of the intuitive equivalent circuit elements using the explanation of the EM-field distribution. The field simulation results are shown in Fig. 9 and Fig. 10. Figure 9 shows the field distribution in the pass-band region at the frequency of 1GHz. The magnetic field concentrates in both quarter-circle DGS heads, while a very weak electric field appears in near between both poles of this DGS structure. The transmission power between both feeds is magnetic. Both heads of this DGS will be approached to inductivity (zone I).

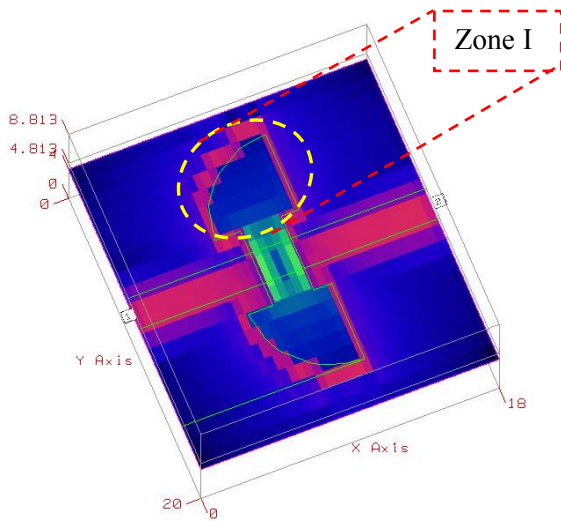


Fig. 9. Electromagnetic field distribution results in the DGS resonator at $f=1$ GHz.

Figure 10 shows a cell with a stop-band behavior at a resonant frequency of 11 GHz. The electric and magnetic fields show same distribution densities. The electric field concentrates between both heads along of the slot, which presents the capacity (Zone II). Based on this EM field investigation, the parallel LC circuit can be an approach model of the DGS unit.

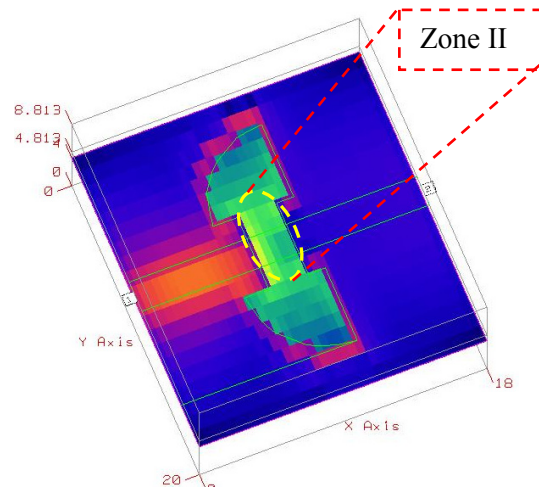


Fig. 10. Electromagnetic field distribution results in the DGS resonator at $f=f_0=11$ GHz.

IV. ULTRA-WIDE STOP-BAND LPF DESIGN USING THE PROPOSED QC-DGS

Taking advantage from the features of the structure presented in the previous section, a compact ultra-wide stop-band LPF composed of two identical QC-DGS units and a compensated microstrip line (CML) as shown in Fig. 11(a) is designed and implemented. This structure avoids employment of LPF units and allows significant enhancement of the characteristics shown in Fig. 2 of the considered structure in the previous section. This results in an ultra-wide stop-band with good insertion and return losses in the LPF pass-band.

The separation between two adjacent resonators (d) is 6 mm, and the width of CML (w_1) is 4.93 mm. The proposed filter can be modeled as two resonators with two shunt capacitors C_p which correspond to the CML as shown in Fig. 11(b).

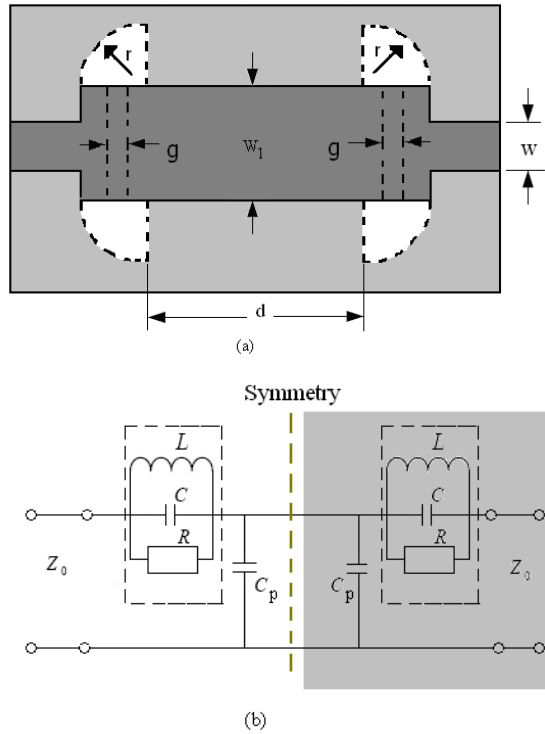


Fig. 11. The proposed ultra-wide stop-band LPF (a) geometry ($r=5$ mm, $g=2.5$ mm, $w=1.92$ mm, $w_1=4.93$ mm and $d=6$ mm), and (b) equivalent circuit model ($C_p=0.562$ pF).

The ECM and full-wave EM simulation results are shown in Fig. 12.

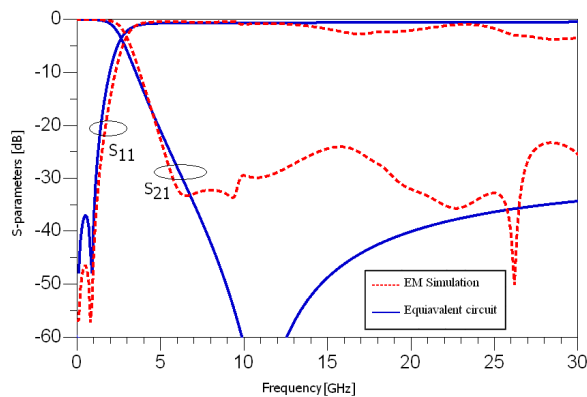


Fig. 12. Equivalent circuit model and EM-simulations of the proposed ultra-wide stop-band LPF.

From Fig. 12, it is clear that the proposed LPF behaves well in both pass-band and stop-band. It is found that the filter has a -3dB cutoff frequency at 2.95 GHz, an insertion loss of 0.1 dB which is

quite small and, a return loss less than -25 dB in the whole pass-band. In addition, an ultra-wide suppression level approximately equal to -20 dB in the frequency stop-band ranging from 5 GHz to more than 30 GHz is achieved. Besides, reasonably good agreement between ECM and full-wave EM simulations can be seen except some difference appears at more than 7 GHz for insertion loss. It could be resulted from the simplicity of the lumped circuit model that the distributed effects are not included in this model. This result shows that the circuit model provides quite good performances and confirms its validity. Furthermore, it can be used as a good tool for initial design and parametric study of the structure that will be refined by EM simulation which provides more accuracy for the predicted insertion loss.

V. FIELD DISTRIBUTION IN THE LOW PASS FILTER

Figure 13 shows the EM-field distribution in the stop-band and in the pass-band of the proposed structure. The simulations of electromagnetic field are carried out using method-of-moments (MOM) by using AWR-simulator.

Figure 13(a) shows the distribution of E-field and H-field in the filter structure at frequency of 1.2 GHz (pass-band). At low frequency, most of the electromagnetic field is distributed around of the DGS resonators and between the input and output of the structure. At transmission domain, the magnetic coupling is the dominant; furthermore it will be easy to improve the response in the pass-band area by changing the distance between both DGS resonators. Contrariwise, from 6.2 GHz the maximal RF current concentrates in the near of the first resonator. As Fig. 13(b) shows, the compensated capacitor is short-circuited and the coupling between the DGS resonators is nearly vanishes, thus no energy flows from the input to output of the filter.

VI. IMPLEMENTATION AND MEASUREMENT

The proposed LPF with two DGSs in the metallic ground plane and a CML on the top layer with size of 24×15 mm² is fabricated as shown in Fig. 14.

Table 1: Comparison of the proposed DGS-LPF with other related LPF

	Substrate dielectric constant/height (mm)	Size (mm ²) x X y	Cutoff frequency fc (GHz)	Stop-band (dB) with -20 dB rejection	Pass-band insertion loss (dB)	Pass-band return loss (dB)
Ref. [2]	4.4/0.8	21 x 20	03.5	4.3 - 15.8	< 2	-
Ref. [3]	3.38/1.524	71 x 13	02.4	3.26 - 10	< 2.26	> 5
Ref. [4]	4.4/0.8	27 x 23	03.7	3.75 - 20	< 1	-
Ref. [5]	2.2/0.788	34 x 11	1.37	4 - 12	-	> 20
This work	3.38/0.813	24 x 15	2.95	4 - 20	0.1	> 20

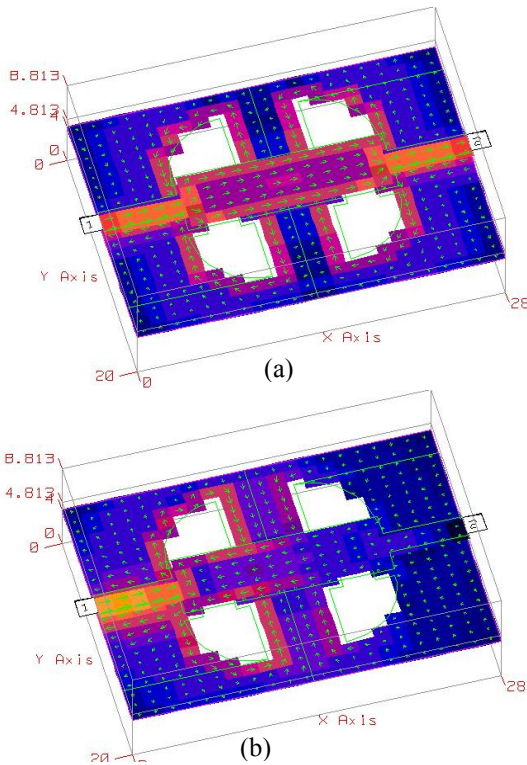


Fig. 13. Electromagnetic field distribution results in the LPF. (a) pass-band at 1.2 GHz and (b) stop-band at 6.2 GHz.

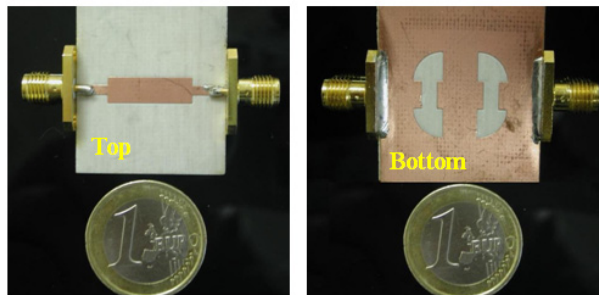


Fig. 14. Photography of the proposed ultra-wide stop-band LPF with 02 DGS patterns.

Figure 15 shows the measured and the simulated results. It is observed from Fig. 15 that the measured results agree with the simulated ones.

From the measured results (see Fig. 15), it is seen that the fabricated UW stop-band LPF has a -3dB cutoff frequency at 2.95 GHz, an insertion loss lower than 0.1 dB in the filter pass-band and, a stop-band suppression at a level lower than -20 dB from 4 GHz to more than 20 GHz. The small deviations between the simulated and measured results may most probably be caused by the usual connectors and manufacturing errors.

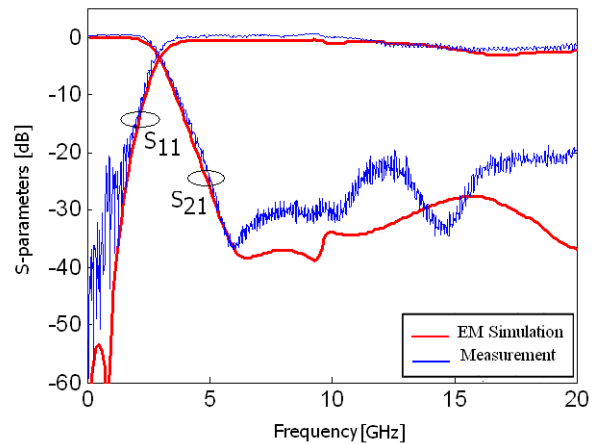


Fig. 15. Measured and simulated S-parameters of the proposed ultra-wide stop-band LPF.

The performance of the proposed DGS LPF is summarized in Table 1 with other reported LPFs for comparison. It can be seen from Table 1 that the proposed filter provides good performances in stop-band rejection and pass-band insertion loss and smaller in size (24 x 15 mm²) than those reported in literature.

VII. CONCLUSION

In this paper, a novel quarter-circle (QC) shape defected ground structure (DGS) and its application to implement an ultra-wide reject band low-pass filter (LPF) has been introduced and investigated. The proposed LPF presents a low insertion loss of 0.1 dB, a return loss much lower than -20 dB, suppression levels approximately -20 dB from 4 GHz to more than 20 GHz and has small size. It has been shown that the simulations results achieved by circuit model and full-wave EM were in excellent agreement with the measurement ones. The proposed compact and high performance LPF can be used in a wide range of microwave and millimeter wave applications.

ACKNOWLEDGMENT

This work was financially supported by the Deutsche Forschungsgemeinschaft (DFG). The authors wish to thank the German Research Foundation for making this project possible. We are grateful to our colleague Ph.D. candidate Abdo Gaber for his contribution to this paper.

REFERENCES

- [1] D. S. La, Y. H. Lu, and J. L. Zhang, "Compact Low-Pass Filters using Novel Φ -Shape Defected Ground Structure," *Microw. and Optical Technology Lett.*, vol. 53, pp. 1456-1459, June 2011.
- [2] H. J. Chen, T. H. Huang, C. S. Chang, L. S. Chen, N. F. Wang, Y. H. Wang, and M. P. Hwang, "A Novel Cross-Shaped DGS Applied to Design Ultra-Wide Stop-Band Low-Pass Filters," *IEEE Microw. Wireless Comp. Lett.*, vol. 16, no. 5, pp. 252-254, May 2006.
- [3] S. W. Ting, K. W. Tam, and R. P. Martins, "Miniaturized Microstrip Lowpass Filter with Wide Stop-Band Using Double Equilateral U-Shaped Defected Ground Structure," *IEEE Microwave Wireless Compon Lett.*, vol. 16, pp. 240-242, May 2006.
- [4] P. Y. Hsiao and R. M. Weng, "An Ultra-Wide Stop-Band Low-Pass Filter Using Dual Reverse U-Shaped DGS," *Microw. and Optical Technology Lett.*, vol. 50, no. 11, pp. 2783-2780, November 2008.
- [5] M. Al Sharkawy, A. Boutejdar, D. El Aziz, and E. Galal, "Design of Compact Microstrip Filter with Large Reject Band using a New Multisectioned T-Shaped Defected Ground Structure and Multilayer Technique," *Microw. and Optical Technology Lett.*, vol. 53, no. 08, pp. 1770-1774, August 2011.
- [6] A. Boutejdar, M. Challal, and A. Azrar, "A Novel Band-Stop Filter Using Octagonal-Shaped Patterned Ground Structures along with Interdigital and Compensated Capacitors," *Applied Computational Electromagnetics Society (ACES) Journal*, vol. 26, no. 4, pp. 312-318, April 2011.
- [7] G. E. Al-Omair, S. F. Mahmoud, and A. S. Al-Zayed, "Lowpass and Bandpass Filter Designs Based on DGS with Complementary Split Ring Resonators," *Applied Computational Electromagnetics Society (ACES) Journal*, vol. 26, no. 11, pp. 907-914, November 2011.
- [8] S. U. Rehman, A. F. A. Sheta, and M. A. S. Alkanhal, "Compact Bandpass Filters with Bandwidth Control Using Defected Ground Structure (DGS)," *Applied Computational Electromagnetics Society (ACES) Journal*, vol. 26, no. 7, pp. 624-630, July 2011.
- [9] M. Al Sharkawy, A. Boutejdar, F. Alhefnawi, and O. Luxor, "Improvement of Compactness of Lowpass/Bandpass Filter Using a New Electromagnetic Coupled Crescent Defected Ground Structure Resonators," *Applied Computational Electromagnetics Society (ACES) Journal*, vol. 25, no. 7, pp. 570-577, July 2010.
- [10] F. Karshenas, A. R. Mallahzadeh, and J. Rashed-Mohassel, "Size Reduction and Harmonic Suppression of Parallel Coupled-Line Bandpass Filters Using Defected Ground Structure," *Applied Computational Electromagnetics Society (ACES) Journal*, vol. 25, no. 2, pp. 149-155, February 2010.
- [11] N. M. Garmjani, N. Komjani, "Improved Microstrip Folded Tri-Section Stepped Impedance Resonator Bandpass Filter using Defected Ground Structure," *Applied Computational Electromagnetics Society (ACES) Journal*, vol. 25, no. 11, pp. 975-983, November 2010.
- [12] Y. Guo and Q. Wang, "An Improved Parameters Extraction Method for Dumbbell-Shaped Defected Ground Structure," *Engineering Journal*, vol. 2, pp. 197-200, March 2010.



Mouloud Challal was born on March 6, 1976, in Algiers, Algeria. He received the electronics and communication engineering degree from University of Bab-Ezzouar, Algiers, Algeria, in April 1999, the M.Sc. degree in microwave and communication from Ecole Nationale Polytechnique, Algiers, Algeria, in Dec. 2001 and the doctorate degree from University of Boumerdes, Algiers, Algeria, in Mar. 2012. Currently, he is a lecturer in the institute of Electrical and Electronic Engineering of Boumerdes

University. His research interests include RF/Microwave circuits, design and analysis of microstrip filters, DGSs behaviors, wireless communication systems, microstrip antenna array analysis, synthesis and design.

Dr. Challal is a member of IEEE and European microwave association (EuMA), and is a reviewer of several international journals and conferences. He is also, the treasurer of IEEE Algeria Subsection.



Ahmed Boutejdar was born in Souk El-Arbaa du Gharb, Morocco. He received the Diplom (Licence) in Mathematics, Physics and Chemistry from Ibn Tofeil University, Kénitra, Morocco and from Technische Hochschule Köthen between 1991 and 1995.

He received B.Sc., Diplom-Eng. And Doktor-Ing. degrees (Ph.D. degree) in Electrical Engineering, Communication, and Microwave Engineering from Otto-von-Guericke university, Magdeburg, Germany in 2002, 2004, and 2010, respectively. He is currently working on a research project on Design, optimization, CMOS-compatible fabrication and characterization of MEMS tunable planar and coplanar DGS filters. His research interests include the design and analysis of microstrip filters, Defected Ground Structures behaviours, fractal DGS-filters, UWB-DGS-filters and tunable DGS-filters using MEMS-technology.

Dr. Boutejdar has published over 110 scientific papers in international journals and in international conference proceeding, and is a reviewer of several international journals and conferences.



Mokrane Dehmas was born in April 1967 in Tizi-Ouzou, Algeria. He received the Engineer and Magister degrees in the National Institute of Electricity and Electronics (INELEC-Boumerdes, Algeria) respectively in 1991 and 1996. He is currently an associate

professor in the Institute of Electrical and Electronic Engineering of the University of Boumerdes and a member of the research team in communication systems. His main fields of interest are semiconductor devices modeling and microstrip radiating structures.



Arab Azrar was born in Takerboust, Bouira, Algeria, on August 2nd, 1971. He received the B.S. degree in Electrical and Electronic Engineering from National Institute of Electricity and Electronics of Boumerdes Algeria in 1995 and the MS and doctorate

degrees from National Polytechnic school of El-Harrach; Algeria respectively in 1998 and 2004. Currently, he is a lecturer in the institute of Electrical and Electronic Engineering of Boumerdes University and his fields of interest include Antennas, Propagation, and Microwaves.



A. S. Omar received the B.Sc. and M.Sc. degrees from Ain Shams University, Cairo, Egypt, in 1978 and 1982, respectively, and the Doktor-Ing. degree in electrical engineering from the Technical University of Hamburg, Hamburg-Harburg, Germany, in 1986. Since 1990, he has been a Professor of

electrical engineering and Head of Chair at the University of Magdeburg, Magdeburg, Germany. He is an Editorial Board member of the Proceedings of the Institution of Electrical Engineers, Electronics Letters, and the Journal of Electromagnetics.

Dr. Omar is a member of the Technical Program Committee of the IEEE Microwave Theory and Techniques Society (MTT-S) Symposium. He is an Editorial Board member of the IEEE Transactions on Microwave Theory and Techniques, the IEEE Transactions on Antennas and Propagation, and the IEEE Microwave and Wireless Components Letters. He is also the IEEE MTT-S financial coordinator for Region 8.

Band-Notch Slot Antenna with Enhanced Bandwidth by using Ω -Shaped Strips Protruded inside Rectangular Slots for UWB Applications

A. Valizade¹, Ch. Ghobadi², J. Nourinia³, N. Ojaroudi⁴, and M. Ojaroudi⁵

¹Department of Electrical Engineering
Urmia University, Urmia, Iran
St_a.valizade@urmia.ac.ir

²Department of Electrical Engineering
Urmia University, Urmia, Iran
ch.ghobadi@urmia.ac.ir

³Department of Electrical Engineering
Urmia University, Urmia, Iran
j.nourinia@urmia.ac.ir

⁴Faculty of Electrical & Computer Engineering
Shahid Rajaee Teacher Training University, Tehran, Iran
n_ojaroudi@srttu.edu

⁵Young Research Group
Ardabil Branch, Islamic Azad University, Ardabil, Iran
m.ojaroudi@iauardabil.ac.ir

Abstract — A novel method for designing a new slot antenna with band-notch characteristic for UWB applications has been presented, in this paper. The proposed antenna consists of a slotted ground plane with an extra rectangular slot on its top, in which a Ω -shaped strip is protruded, and a square-ring radiating stub in which a Ω -shaped strip is protruded. By inserting the rectangular slot with a Ω -shaped strip which is protruded inside this slot, in the ground plane, additional resonance is excited and hence much wider impedance bandwidth can be produced, especially at the higher band, which consequently results in a wide usable fractional bandwidth of more than 125% (3.07-14.03 GHz). In order to generate a band-notch characteristic, we use a square-ring radiating stub with a Ω -shaped strip which is protruded inside this radiating stub. The measured results reveal that the presented slot antenna offers a wide

bandwidth with a band-notch operation which notches the WLAN band (5.02-5.97 GHz). The designed antenna has a small size of 20×20 mm². Good VSWR and radiation pattern characteristics are obtained in the frequency band of interest.

Index Terms — Band-notch function, microstrip-fed slot antenna, protruded Ω -shaped strip, ultra-wideband (UWB) applications.

I. INTRODUCTION

In UWB communication systems, one of the key issues is the design of a compact antenna while providing wideband characteristic over the whole operating band [1]. Consequently, a number of microstrip antennas with different geometries have been experimentally characterized. Moreover, other strategies to improve the impedance bandwidth which do not involve a modification of

the geometry of the planar antenna have been investigated [2-5].

The Federal Communication Commission (FCC)'s allocation of the frequency range 3.1–10.6 GHz for UWB systems causes interference to the existing wireless communication systems, such as the wireless local area network (WLAN) which operates in 5.15–5.35 GHz and 5.725–5.825 GHz bands, so the UWB antenna with a single band-stop performance is required [6-9].

A novel and compact microstrip-fed slot antenna with band-notch characteristic for UWB applications has been presented. Firstly, by inserting a rectangular slot, inside which a Ω -shaped strip is protruded, in the top section of ground plane, additional resonance is excited and hence much wider impedance bandwidth which covers UWB frequency range can be produced. Secondly, to generate a single band-notched function, we use a square-ring radiating stub with a Ω -shaped strip protruded inside the square ring. Good VSWR and radiation pattern characteristics are obtained in the frequency band of interest. Simulated and experimental results show that the proposed slot antenna could be a good candidate for UWB applications.

II. ANTENNA DESIGN

The presented small slot antenna fed by a 50- Ω microstrip line is shown in Fig. 1, which is printed on a FR4 substrate of thickness 0.8 mm, permittivity 4.4, and loss tangent 0.018. The basic slot antenna structure consists of a square stub, a feed line, and a ground plane. The square stub is connected to the 50- Ω microstrip feed-line. On the other side of the substrate, a conducting ground plane is placed. The proposed antenna is connected to a 50- Ω SMA connector for signal transmission.

In this design, to achieve a bandwidth enhancement and a full coverage of UWB frequency range, we etched a rectangular slot inside the ground plane, in which a Ω -shaped strip is protruded. Based on the defected ground structure (DGS), the modified rectangular slot with a Ω -shaped strip protruded inside the slot acts as an impedance matching element to control the impedance bandwidth of the proposed antenna, because it can create additional surface current paths in the antenna and therefore, additional resonance is excited and hence, much wider

impedance bandwidth can be produced, especially at the higher band. As illustrated in Fig. 1, the Ω -shaped strip which is protruded inside the square-ring radiating stub is symmetrical with respect to the longitudinal direction. In this structure, the square ring with a Ω -shaped strip which is protruded inside the square-ring radiating stub can perturb the resonant response and also acts as a half-wave resonant structure [5–6]. At the notched frequency, the current flows are more dominant around the protruded element, and they are oppositely directed between the protruded element and the square-ring radiating stub. As a result, the desired high attenuation near the notched frequency can be produced.

In this work, we start by choosing the aperture length L_s . We have a lot of flexibility in choosing this parameter. The length of the aperture mostly affects the antenna bandwidth. As L_s decreases, so does the antenna BW and vice versa. At the next step, we have to determine the aperture width W_s . The aperture width is approximately $\lambda_s/2$ where λ_s is the slot wavelength. λ_s depends on a number of parameters such as the slot width as well as the thickness and dielectric constant of the substrate on which the slot is fabricated. The last and final step in the design is to choose the length of the radiating patch W . A good starting point is to choose it to be equal to $W=\lambda_m/4$, where λ_m is the guided wavelength in the microstrip line.

The final values of presented slot antenna design parameters are as follows:

Table 1. The final dimensions of the designed antenna

Param	mm	Param	mm	Param	mm
W_{sub}	20	L_{sub}	20	W_s	18
L_s	11	W	7	L_{gnd}	6
W_f	1.5	L_f	4	W_R	6
L_p	4.5	W_p	2	L_{p1}	4.5
W_{p1}	2.5	L_{p2}	5	W_{p2}	2
L_{p3}	0.5	d	7	L_x	5
W_x	6	L_{x1}	2.5	W_{x1}	2
L_{x2}	2.5	W_{x2}	1	L_{x3}	3.5
L_{x4}	0.5				

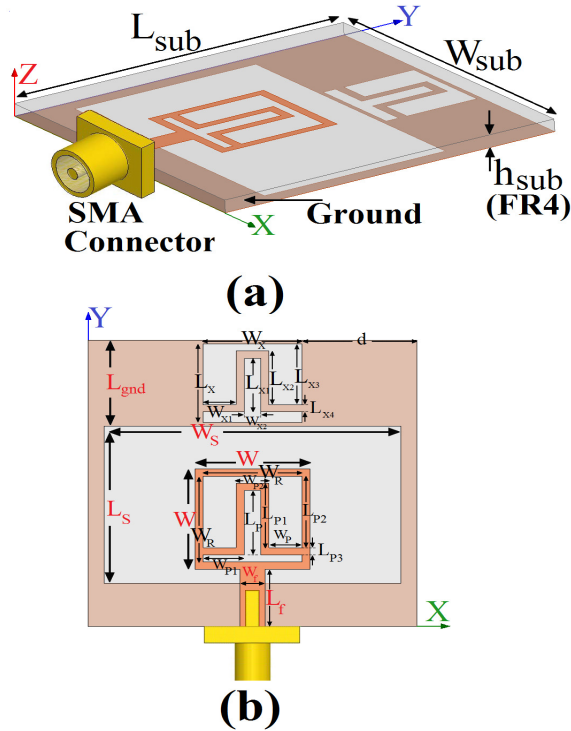


Fig. 1. Geometry of proposed slot antenna, (a) side view, (b) top view.

III. RESULTS AND DISCUSSIONS

In this section, the proposed slot antenna with various design parameters were constructed, and the numerical and experimental results of the input impedance and radiation characteristics are presented and discussed. The proposed microstrip-fed slot antenna was fabricated and tested to demonstrate the effect of the presented structure. The parameters of this proposed antenna were studied by changing one parameter at a time while others were kept fixed. The simulated results are obtained using the Ansoft simulation software high frequency structure simulator (HFSS) [9].

The configurations of various antenna structures are shown in Fig. 2. VSWR characteristics for ordinary slot antenna (Fig. 2 (a)), slot antenna with a rectangular slot with an Ω-shaped strip protruded inside the slot in the ground plane (Fig. 2(b)), and the proposed slot antenna structure (Fig. 2 (c)), are compared in Fig. 3. As shown in Fig. 3, it is observed that the upper frequency bandwidth is affected by the presence of the rectangular slot and the protruded Ω-shaped strip, which are placed in top section of the ground plane. Moreover, the notched frequency bandwidth is sensitive to the square-ring radiating stub which

has a Ω-shaped strip protruded inside the square ring.

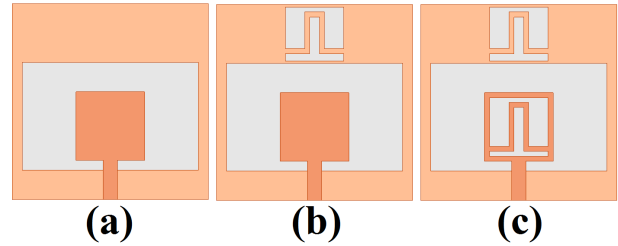


Fig. 2. (a) Basic structure (ordinary slot antenna), (b) antenna with a rectangular slot with a Ω-shaped strip protruded inside the slot in the ground plane, (c) the proposed slot antenna.

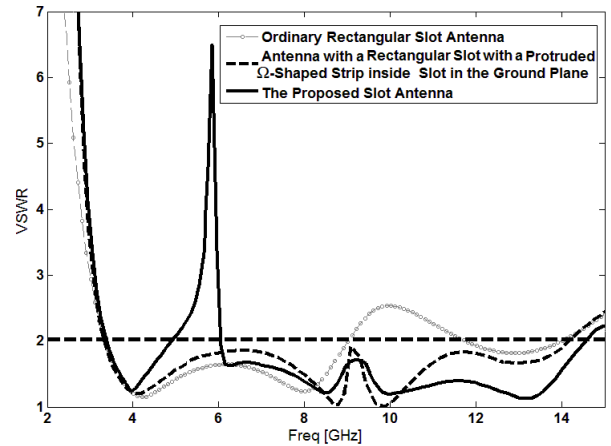


Fig. 3. Simulated VSWR characteristics for antennas shown in Figure 2.

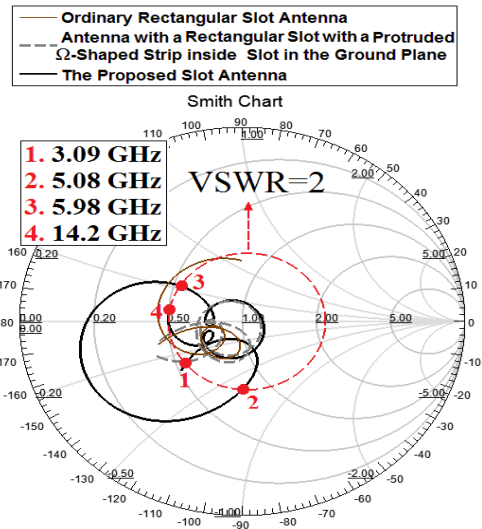


Fig. 4. Smith chart demonstration of simulated input impedance of the various antenna structures which are shown in Fig. 2.

Also the input impedance of the various slot antenna structures that are shown in Fig. 2, are presented on a Smith Chart, as shown in Fig. 4.

To understand the phenomenon behind this bandwidth enhancement, the simulated current distributions on the ground plane for the slot antenna with a rectangular slot in the top section of the ground plane, which has a Ω -shaped strip protruded inside it, at 9.85 GHz is presented in Fig. 5 (a). It can be observed in Fig. 5 (a) that at 9.85 GHz the current concentrates on the edges of the rectangular slot and the interior and exterior edges of the protruded Ω -shaped strip, which are placed on top section of the ground plane. Therefore, the antenna impedance changes at this frequency due to the resonant properties of the protruded strips. It is found that by using this structure, third resonance is generated at 9.85 GHz [4]. Another important design parameter of this structure is the square-ring radiating stub with a Ω -shaped strip which is protruded inside the square ring. Fig. 5 (b) presents the simulated current distributions on the radiating stub plane at the notched frequency (5.5 GHz). As shown in Fig. 5 (b), at the notched frequency the current flows are more dominant around the edges of the square-ring radiating stub and the Ω -shaped strip which is protruded inside the square-ring. As a result, the desired high attenuation near the notched frequency can be produced [7].

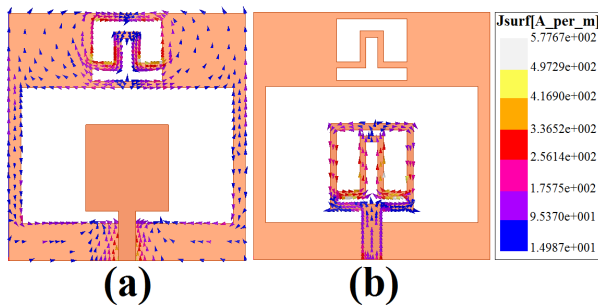


Fig. 5. Simulated surface current distributions (a) on the ground plane for the slot antenna with a rectangular slot with a Ω -shaped strip protruded inside the slot in the ground plane at 9.85 GHz, (b) on the radiating stub for the proposed antenna at notch central frequency (5.5 GHz).

VSWR characteristics for various values of the feed gap distance of the bottom edge of the square radiating stub and the ground plane (d) were analyzed and are illustrated in Fig. 6.

From the results, it is observed that the feed gap distance d is an important parameter in determining the sensitivity of impedance matching.

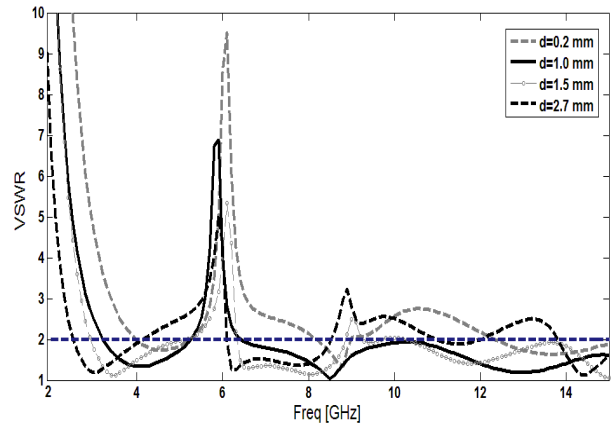


Fig. 6. The effect of various values of d (the feed gap distance) on VSWR.

By adjusting d , the electromagnetic coupling between the bottom edge of the square ring radiating stub and the ground plane can be properly controlled [6]. It is seen that the lower-edge frequency of the impedance bandwidth is reduced with increasing the gap distance, but the matching became poor for larger values. Therefore it can be seen that the optimized gap, d , is 1 mm.

The measured and simulated VSWR characteristics of the proposed antenna are shown in Fig. 7. The fabricated antenna covers the frequency band of 3.07 to over 14.03 GHz with a band-notch function around 5.02-5.97 GHz. As shown in Fig. 7, there exists a discrepancy between the measured data and the simulated results. In a physical network analyzer measurement, the feeding mechanism of the proposed antenna is composed of a SMA connector and a microstrip line (the microstrip feed-line is excited by a SMA connector) whereas the simulated results are obtained using the Ansoft simulation software (HFSS), that in HFSS by default, the antenna is excited by a wave port that it is renormalized to a 50-Ohm full port impedance at all frequencies, therefore this discrepancy between measured data and the simulated results could be due to the effect of the SMA port [6]. In order to confirm the accuracy of VSWR characteristics for the designed antenna, it is recommended that the manufacturing and

measurement processes need to be performed more carefully. In conclusion, as the slot antenna is a short radiator, the SMA connector can degrade its impedance matching.

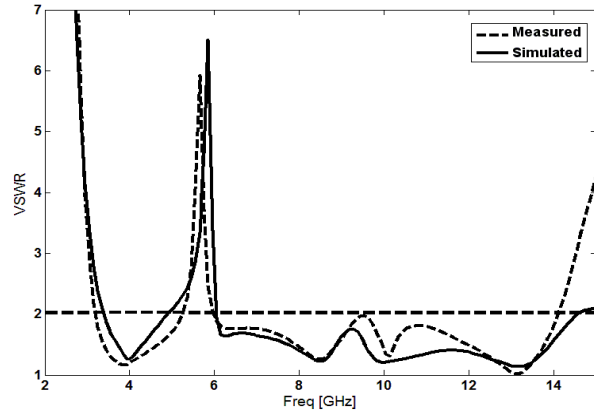


Fig. 7. Measured and simulated VSWR characteristics of the proposed antenna.

Figure 8 illustrates the measured radiation patterns, including the co-polarization and cross-polarization, in the H-plane ($x-z$ plane) and E-plane ($y-z$ plane). It can be seen that the radiation patterns in $x-z$ plane are nearly omnidirectional for three frequencies.

The radiation patterns have been measured inside an anechoic chamber. A two-antenna technique is used to measure the radiation patterns in the z axis direction ($x-z$ plane). Single polarization standard horn is used as transmitter and the fabricated antenna is put as receiver (antenna under test). These measurements were obtained using indoor anechoic chamber room. Several requirements are needed to take into consideration during the measurement process. Obtaining true patterns depends primarily on accurately positioning the probe, accurately measuring the field, and eliminating distortions in the field introduced by the room, track, or the probe itself. The room reflections must be lower than the basic side-lobe-level. The probe itself must have low reflections and accurate position. The measured radiation patterns were plotted into horizontal (H) and vertical (V) cuts. The H-cut is cut for the azimuth plane with fixed elevation angle at 0° and vary the azimuth angle. The V-cut is cut for the elevation plane with fixed azimuth angle at 0° and vary the elevation angle.

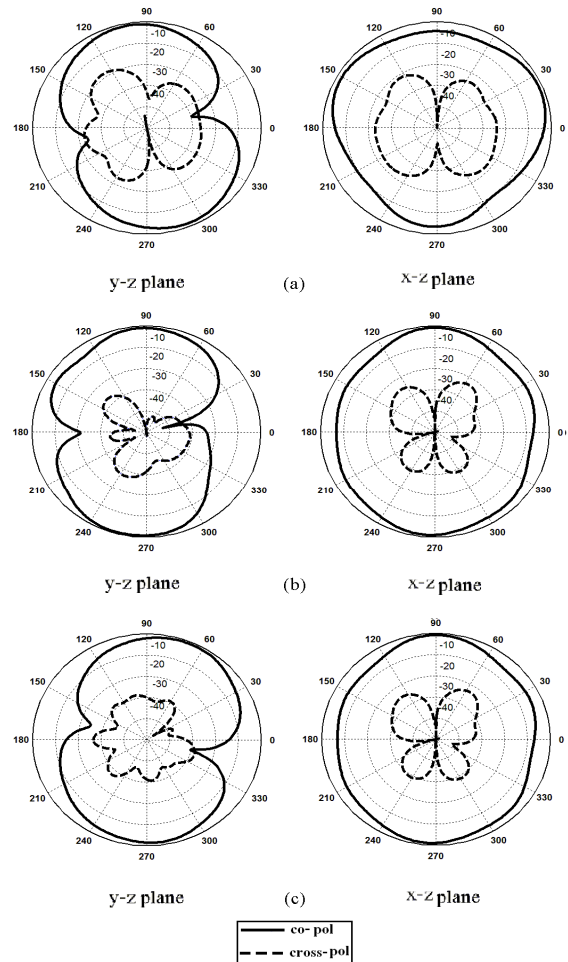


Fig. 8. Measured radiation patterns of the proposed antenna. (a) 4.8 GHz, (b) 7.5 GHz, and (c) 10 GHz.

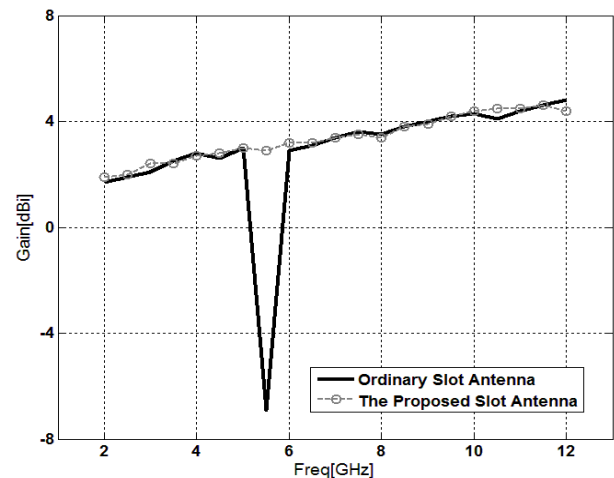


Fig. 9. Maximum gain comparison for the ordinary slot antenna (simulated), and the proposed slot antenna (measured) in the z axis direction ($x-z$ plane).

Figure 9 shows the effects of the rectangular slot with a Ω -shaped strip protruded inside the slot in the ground plane, and a square-ring radiating stub with a Ω -shaped strip protruded inside the square ring on the maximum gain in comparison to the ordinary slot antenna without them. As shown in Fig. 9, the ordinary slot antenna has a gain that is low at 3 GHz and increases with frequency. It is found that the gain of the ordinary antenna is decreased with the use of the rectangular slot with a Ω -shaped strip protruded inside the slot in the ground plane, and the square-ring radiating stub with a Ω -shaped strip protruded inside the square ring. It can be observed in Fig. 9 that by using these structures, a sharp decrease of maximum gain at the notched frequency band of 5.5 GHz occurs. For other frequencies outside the notched frequencies band, the antenna gain with the filter is similar to those without it.

V. CONCLUSION

A new slot antenna with band-notch function for UWB applications is presented. The proposed antenna can operate from 3.07 to 14.03 GHz with WLAN rejection band performance around 5.02–5.97 GHz. In order to enhance the bandwidth we use a rectangular slot with a Ω -shaped strip protruded inside the slot in the ground plane, and also by using a square-ring radiating stub with a Ω -shaped strip protruded inside the square ring, a frequency band-notch function can be achieved. The designed antenna has a small size of 20×20 mm². Simulated and experimental results show that the proposed slot antenna could be a good candidate for UWB applications.

ACKNOWLEDGMENT

The authors are thankful to Microwave Technology (MWT) Company staff for their beneficial and professional help (www.microwave-technology.com).

REFERENCES

- [1] H. Schantz, *The Art and Science of Ultra Wideband Antennas*, Artech House, 2005.
- [2] M. Ojaroudi and A. Faramarzi, "Multi-Resonance Small Square Slot Antenna for Ultra-Wideband Applications," *Microwave and Optical Tech. Letters*, vol. 53, no. 9, September 2011.

- [3] R. Azim, M. T. Islam, and N. Misran, "Design of a Planar UWB Antenna with New Band Enhancement Technique," *Applied Computational Electromagnetics Society (ACES) Journal*, vol. 26, no. 10, pp. 856-862, October 2011.
- [4] D. S. Javan and O. H. Ghouhani, "Cross Slot Antenna with U-Shaped Tuning Stub for Ultra Wideband Applications," *Applied Computational Electromagnetics Society (ACES) Journal*, vol. 24, no. 4, pp. 427-432, August 2009.
- [5] A. Dastranj, A. Imani, and M. Naser-Moghaddasi, "Printed Wide-Slot Antenna for Wideband Applications," *IEEE Transactions on Antenna and Propagations*, vol. 56, no. 10, pp. 3097-3102, October 2008.
- [6] N. Ojaroudi, M. Ojaroudi, and H. Ebrahimian, "Band-Notched UWB Microstrip Slot Antenna with Enhanced Bandwidth by using a Pair of C-Shaped Slots," *Microwave and Optical Tech. Letters*, vol. 54, no. 2, pp. 515-518, February 2012.
- [7] J. William and R. Nakkeeran, "A New UWB Slot Antenna with Rejection of WiMax and WLAN Bands," *Applied Computational Electromagnetics Society (ACES) Journal*, vol. 25, no. 9, pp. 787-793, September 2010.
- [8] M. Naghshvarian-Jahromi and N. Komjani-Barchloui, "Analysis of the Behavior of Sierpinski Carpet Monopole Antenna," *Applied Computational Electromagnetics Society (ACES) Journal*, vol. 24, no. 1, pp. 32-36, February 2009.
- [9] Ansoft High Frequency Structure Simulation (HFSS), Ver. 13, Ansoft Corporation, 2010.



Arash Valizade was born in Tehran, Iran 1986. He received his B.Sc. in Electrical Engineering-Electronic from Azad University of Sabzevar, Iran, in 2008 and M.Sc. degrees in Electrical Engineering-Telecommunication from University of Urmia, Urmia, Iran, in 2012. His primary research interests are in numerical methods in electromagnetics, microstrip antenna design, active integrated antenna and reconfigurable structures.



Changiz Ghobadi was born on June 1, 1960 in Iran. He received his B.Sc. in Electrical Engineering-Electronic and M.Sc. degrees in Electrical Engineering-Telecommunication from Isfahan University of Technology, Isfahan, Iran and Ph.D. degree in Electrical-Telecommunication from University of Bath, Bath, UK in 1998. From 1998, he was an assistant professor and now he is an associated professor in the Department of Electrical Engineering of Urmia University, Urmia, Iran. His primary research interests are in antenna design, radar and adaptive filters.



Javad Nourinia received his B.Sc. in Electrical and Electronic Engineering from Shiraz University and M.Sc. degree in Electrical and Telecommunication Engineering from Iran University of Science and Technology, and Ph.D. degree in Electrical and Telecommunication from University of Science and Technology, Tehran Iran in 2000. From 2000, he was an assistant professor and now he is an associated professor in the Department of Electrical Engineering of Urmia University, Urmia, Iran. His primary research interests are in antenna design, numerical methods in electromagnetic, microwave circuits.



Nasser Ojaroudi was born in 1986 in Germi, Iran. He received his B.Sc. degree in Electrical Engineering from Azad University, Ardabil Branch. From 2011, he is working toward the M.Sc. degree in Telecommunication Engineering at Shahid Rajaee Teacher Training University. Since March 2008, he has been a Research Fellow in the Microwave Technology Company (MWT), Tehran, Iran. His research interests include monopole antenna, slot antennas, microstrip antennas for radar systems, ultra-wideband (UWB) and small antennas for wireless communications, microwave passive devices and circuits, and microwave/millimeter systems.



Mohammad Ojaroudi was born in 1984 in Germi, Iran. He received his B.Sc. degree in Electrical Engineering from Azad University, Ardabil Branch and M.Sc. degree in Telecommunication Engineering from Urmia University. From 2010, he is working toward the Ph.D. degree at Shahid Beheshti University. From 2007 until now, he is a Teaching Assistant with the Department of Electrical Engineering, Islamic Azad University, Ardabil Branch, Iran. Since March 2008, he has been a Research Fellow (Chief Executive Officer) in the Microwave Technology Company (MWT), Tehran, Iran. His research interests include analysis and design of microstrip antennas, design and modeling of microwave structures, radar systems, and electromagnetic theory. He is author and coauthor of more than 60 journal and international conference papers.

Broadband and Compact Zeroth-Order Resonant Antennas with Truncated Grounds

Jian-Chao Liu and Wei Shao

Institute of Applied Physics
University of Electronic Science and Technology of China, Chengdu, 610054, China
ljc_221@126.com, weishao@uestc.edu.cn

Abstract — This paper presents the analysis and design of broadband and compact zeroth-order resonant (ZOR) antennas based on truncated grounds. A ZOR unit cell, whose physical size is independent of the operating frequency due to the fundamental infinite wavelength, can be implemented with a composite right/left-handed (CRLH) or inductor-loaded transmission line (TL). The two types of ZOR antennas with extended bandwidth and more compact size are achieved by introducing the truncated grounds. It is also shown that the supported infinite wavelength can be used to generate a monopole-like radiation pattern. The characteristics of the broadband and compact size of the proposed antennas are verified by the simulated and measured results.

Index Terms — CRLH, inductor-loaded, truncated grounds, ZOR antenna.

I. INTRODUCTION

Metamaterials, which do not exist in nature, have been hypothesized by Veselago in 1968 [1]. Compared with the conventional materials, metamaterials have many unique properties, such as the reversal of Snell's law, the Doppler Effect, and the Vavilov-Cerenkov effect [2]. The appearance of man-made metamaterials has allowed innovations in antennas and microwave circuits to be developed [3-10].

Particularly, the zero propagation constant property is used to design zeroth-order resonant (ZOR) antennas. A ZOR antenna has an infinite wavelength and its resonant frequency is independent of the antenna size. Therefore, a ZOR antenna can be much more compact than a

conventional half-wavelength antenna [10-12]. However, the narrow bandwidth of a ZOR antenna limits its wireless applications.

In recent years, some ZOR antennas are designed to increase the bandwidth. The structure in [13] has a broad bandwidth by using air as the dielectric material. However, it is difficult to fabricate such an antenna. In [14], a strip matching ground is employed to increase the bandwidth. It is built on multiple substrates where a thin substrate with high permittivity is stacked on a thick substrate with low permittivity. Alternatively, the bandwidth of the antenna in [15] is enhanced due to two resonant frequencies which are slightly different. In addition, a broadband coplanar waveguide-fed ZOR antenna is proposed in [16] and a method to extend the bandwidth of metamaterial antennas using a composite right/left-handed (CRLH) structure is presented in [17].

In this paper, two types of ZOR antennas based on CRLH transmission line (TL) and inductor-loaded TL unit cells are studied, respectively. A kind of truncated grounds is adopted to improve the bandwidth performance and further reduce the physical size of the ZOR antennas. By modifying the equivalent shunt capacitance and/or shunt inductance of the unit cells, the bandwidths are substantially extended and physical sizes are further miniature compared to the reference antennas. Moreover, they are built on a single layer and easy to be fabricated.

II. ZOR ANTENNA THEORY

A general CRLH TL model, shown in Fig. 1(a), consists of an inductance L_R in series with a capacitance C_L and a shunt capacitance C_R in

parallel with an inductance L_L . One structure that is commonly used to realize a CRLH TL is the Sievenpiper mushroom structure [18, 19]. When there is no gap between the adjacent patches, it simply becomes an inductor-loaded TL. Figure 1(b) plots the equivalent circuit of an inductor-loaded TL.

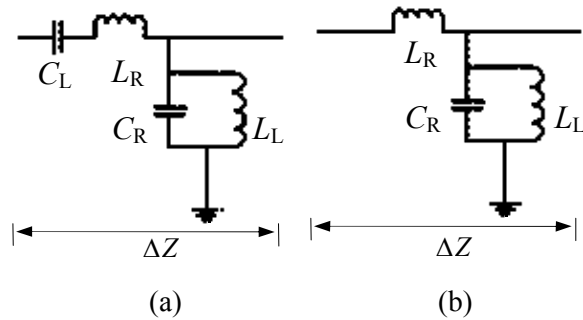


Fig. 1. Models of (a) CRLH TL and (b) inductor-loaded TL.

By applying periodic boundary conditions related to the Bloch-Floquet theorem, the CRLH TL unit cell's dispersion relation is determined by [12]

$$\beta(\omega) = \frac{1}{\Delta Z} \arccos \left(1 - \frac{1}{2} \left(\frac{\omega_L^2}{\omega^2} + \frac{\omega^2}{\omega_R^2} - \frac{\omega_L^2}{\omega_{se}^2} - \frac{\omega_L^2}{\omega_{sh}^2} \right) \right) \quad (1)$$

where

$$\omega_L = \frac{1}{\sqrt{C_L L_L}}, \quad \omega_R = \frac{1}{\sqrt{C_R L_R}} \quad (2)$$

$$\omega_{se} = \frac{1}{\sqrt{C_L L_R}}, \quad \omega_{sh} = \frac{1}{\sqrt{C_R L_L}}$$

It consists of a left-handed (LH) wave at lower band and right-handed (RH) wave at upper band. It can also be predicted that non-zero frequency points (zeroth-order modes) with $\beta = 0$ are presented.

In the case of open boundary conditions, the zeroth-order mode is determined by the shunt resonance (ω_{sh}). That is to say, the series components have no effect on the resonance frequency. Therefore, an inductor-loaded TL unit cell is created when the gap is eliminated. Its propagation constant is given by [12]

$$\beta(\omega) = \frac{1}{\Delta Z} \arccos \left(1 + \frac{1}{2} \left(\frac{L_R}{L_L} - \frac{\omega^2}{\omega_R^2} \right) \right) \quad (3)$$

It can be predicted that only the zeroth-order mode

and RH wave occur in this case.

In this paper, the CRLH TL and inductor-loaded TL unit cells, shown in Fig. 2(a) and (b), are used to realize ZOR antennas.

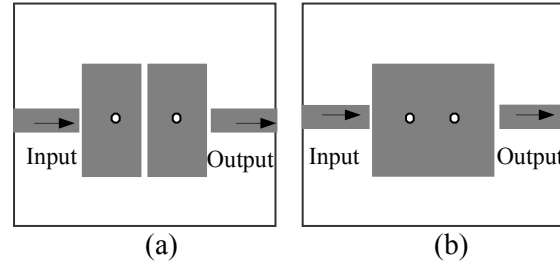


Fig. 2. Configurations of (a) CRLH TL unit cell, and (b) inductor-loaded TL unit cell.

III. PROPOSED BANDWIDTH EXTENSION TECHNIQUE

According to [16], the fractional bandwidth of the resonator is given by

$$BW = G \sqrt{\frac{L_L}{C_R}} \quad (4)$$

where G is the shunt conductance of the lossy CRLH TL. This expression provides a concept with which the bandwidth can be efficiently enhanced by increasing L_L and/or decreasing C_R .

The mushroom unit cell is composed of a rectangle patch, ground plane and metallic via [18]. The LH capacitance and inductance are provided by the capacitance couplings of the top patch with adjacent patches and a metallic via between the top patch and ground plane, respectively. The magnetic flux caused by the flow of current on the top patch contributes to the RH inductance, while the parallel-plate structure between the patch and ground plane contributes to the RH capacitance. The attribute of LH capacitance is eliminated in the case of inductor-loaded TL. Since these configurations provide design freedom for the reactive parameters, both a wider bandwidth and smaller size can be achieved.

IV. ANTENNAS IMPLEMENTATION AND RESULTS ANALYSIS

In this section, the prototypes are all built on the substrate with a relative permittivity of 2.65, loss tangent of 0.001 and thickness of 1.5 mm.

A. CRLH-based ZOR antenna with a truncated ground

The reference model of the CRLH-TL-based ZOR antenna with a whole ground is shown in Fig. 3(a) [12]. The proposed antenna with a truncated ground is illustrated in Fig. 3(b). A feeding line of 50 Ohm and proximity coupling are used as the feed network. As we know, the shunt inductance can be increased in proportion to the length of the shorted stub line. The metallic via lines connecting the metallic via and the ground enlarge the length of the shorted stub line (Fig. 3(b)). Moreover, the area between the top patch and ground plane becomes small, and the shunt capacitance is substantially reduced. Thus, a tradeoff between resonant frequency and bandwidth can be obtained from (2) and (4). In addition, by changing the value of w_2 , not only the shunt capacitance and shunt inductance can be altered, but also the benefit of impedance matching can be achieved. Using the commercial software (Ansoft HFSS) [20], the geometric parameters of the truncated ground are obtained through optimization.

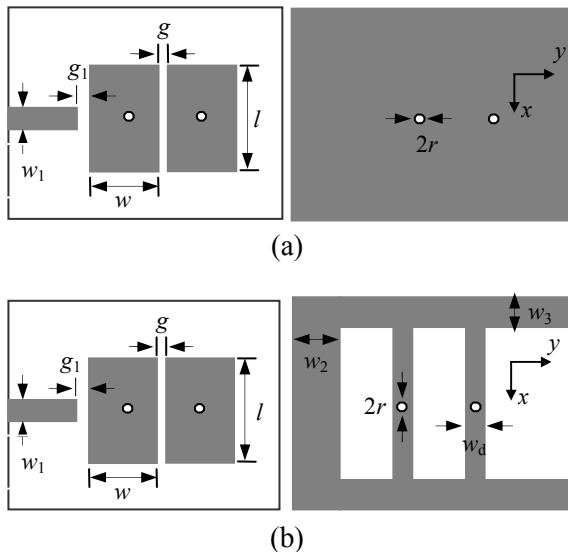


Fig. 3. Top and back views of the CRLH TL antennas: (a) reference antenna and (b) proposed antenna, where $w=7.3$ mm, $l=15$ mm, $w_1=4$ mm, $g=0.2$ mm, $g_1=0.3$ mm, $r=0.2$ mm, $w_d=0.5$ mm, $w_2=10$ mm and $w_3=5$ mm.

In order to verify the theoretical qualitative analysis, we extract the dispersion diagrams, as shown in Fig. 4, for the reference and proposed structures based on the CRLH TL and inductor-

loaded TL unit cells in Fig. 2 [21, 22]. The shunt resonant frequencies for the reference CRLH-TL and ZOR for the reference inductor-loaded TL are almost located at 3.5GHz. The shunt resonant frequency for the proposed CRLH-TL is 2.72GHz and ZOR frequency for the proposed inductor-loaded TL is 2.4GHz.

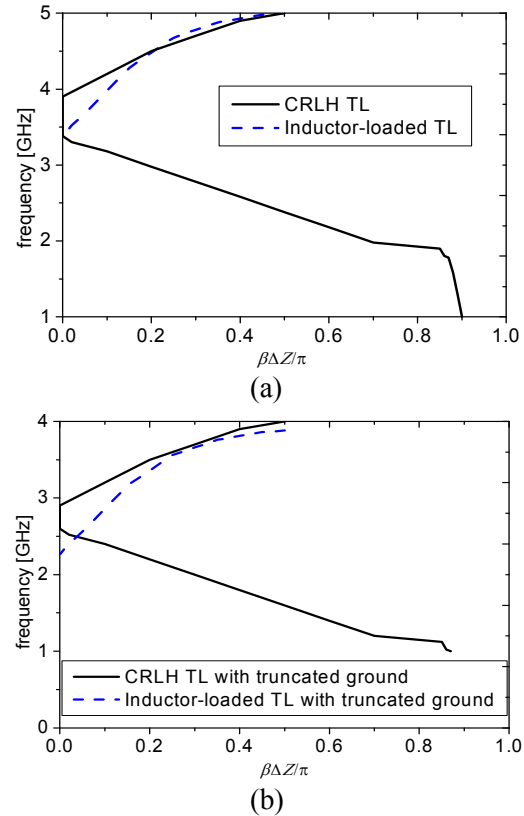
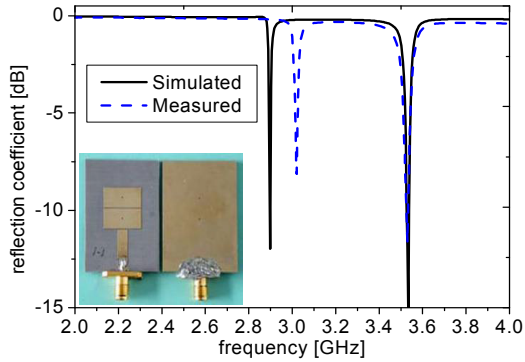


Fig. 4. Dispersion diagrams for (a) two reference unit cells and (b) two proposed unit cells.

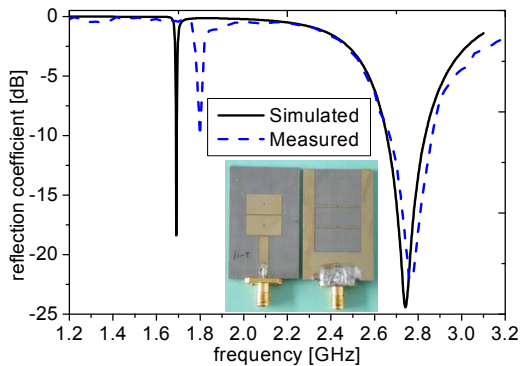
Figure 5 shows the simulated and measured reflection coefficients of the two antennas. The -10dB bandwidth and resonant frequency of the reference CRLH TL antenna are less than 1% and 3.53GHz, respectively. And, for the proposed antenna, the bandwidth is about 7.0% and resonant frequency is about 2.75GHz. The difference between simulation and measurement is mostly due to the influences of manufactured precision and feeding cable.

The simulated radiation patterns of the CRLH TL antennas are shown in Fig. 6. The proposed antenna generates a monopole-like radiation pattern as seen in Fig. 6(b), different from a monopole radiation pattern of the reference

antenna in Fig. 6(a). In terms of the radiation mechanism of the proposed antenna, the magnetic currents mainly concentrate in the slot which approaches to the feeding line. Therefore, the proposed antenna looks like an ideal magnetic dipole rather than a magnetic loop antenna [12].

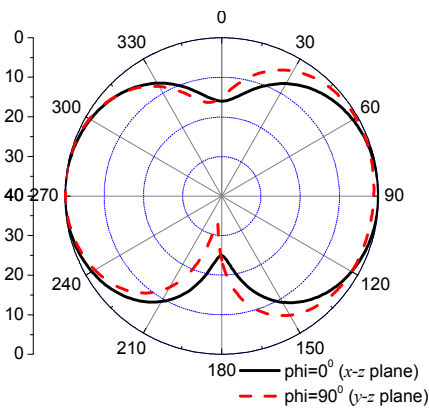


(a)

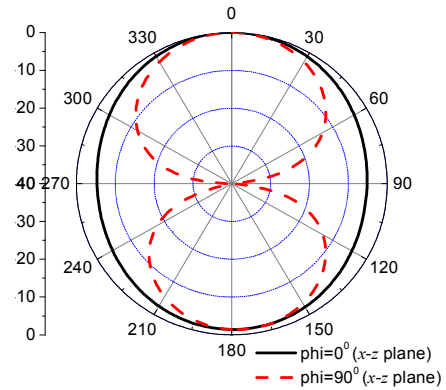


(b)

Fig. 5. Simulated and measured reflection coefficients of CRLH TL antenna (a) with a whole ground and (b) with a truncated ground.



(a)

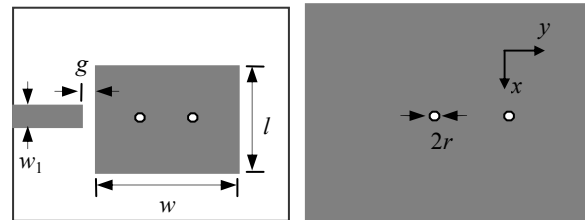


(b)

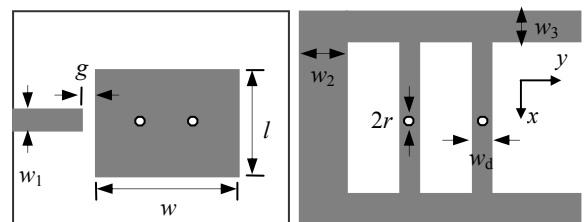
Fig. 6. Simulated radiation patterns for the two CRLH TL antennas (unit: dB) (a) with a whole ground and (b) with a truncated ground.

B. Inductor-loaded ZOR antenna with a truncated ground

The reference and proposed models of the inductor-loaded antenna are shown in Fig. 7(a) and (b), respectively. Similarly, the inductor-loaded antennas with a large L_L and small C_R which result in an improved bandwidth are studied. Figure 8 and Fig. 9 show the reflection coefficients and radiation patterns, respectively. The overall performances of the CRLH TL and inductor-loaded antennas are listed in Table 1.



(a)



(b)

Fig. 7. Top and back views of the inductor-loaded antennas: (a) reference antenna and (b) proposed antenna, where $w=14.8\text{mm}$, $l=15\text{mm}$, $w_1=4\text{mm}$, $g=0.3\text{mm}$, $w_d=0.5\text{mm}$, $w_2=10\text{mm}$, and $w_3=5\text{mm}$.

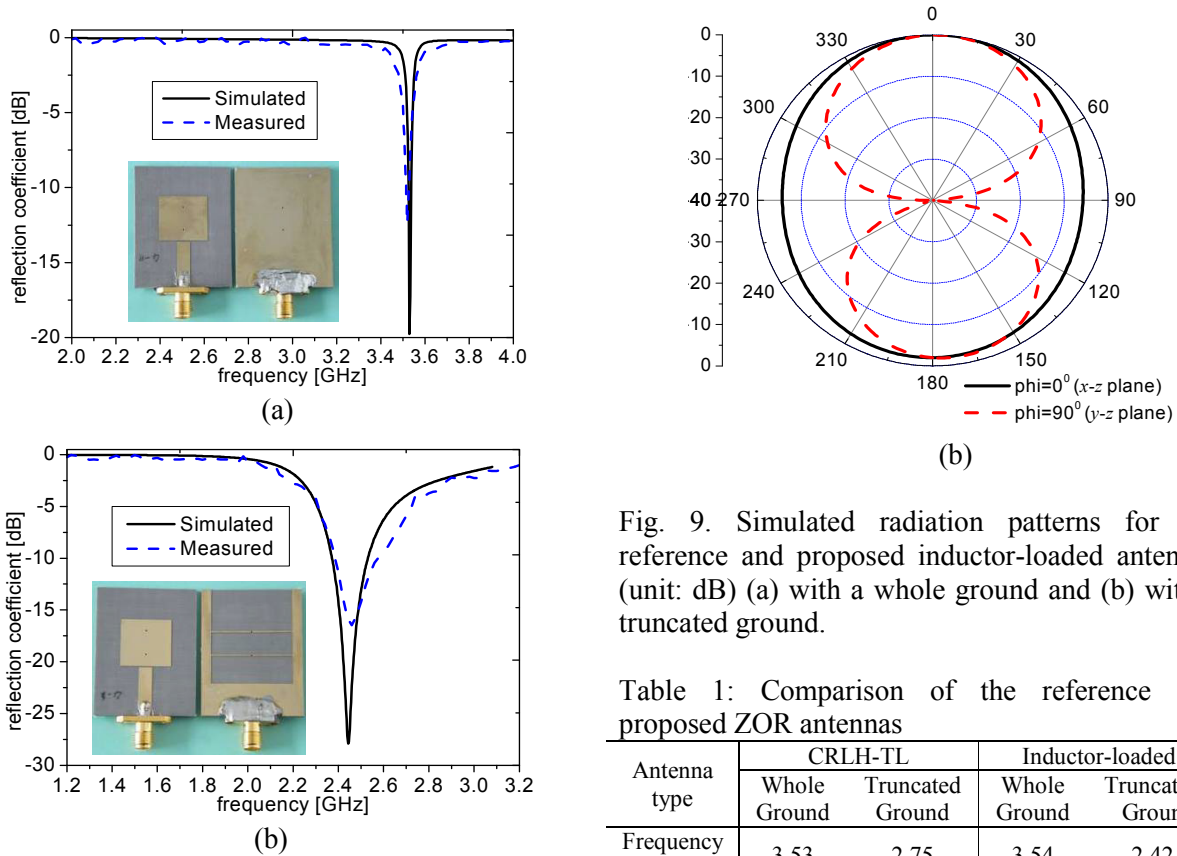


Fig. 8. Simulated and measured reflection coefficients of inductor-loaded antennas (a) with a whole ground and (b) with a truncated ground.

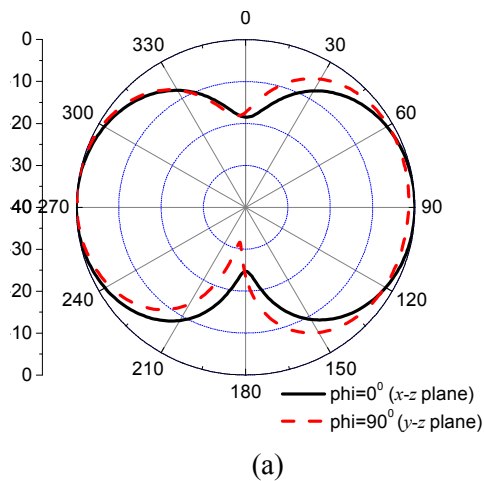


Fig. 9. Simulated radiation patterns for the reference and proposed inductor-loaded antennas (unit: dB) (a) with a whole ground and (b) with a truncated ground.

Table 1: Comparison of the reference and proposed ZOR antennas

Antenna type	CRLH-TL		Inductor-loaded	
	Whole Ground	Truncated Ground	Whole Ground	Truncated Ground
Frequency (GHz)	3.53	2.75	3.54	2.42
Size (λ_0)	0.17 $\times 0.169$	0.13 $\times 0.132$	0.167 $\times 0.169$	0.116 $\times 0.118$
BW (%)	<1	7.0	<1	7.2
Pattern	A	B	A	B
Gain (dB)	1.66	3.29	1.53	2.76
Efficiency (%)	55	67	54	65

A—monopole radiation pattern, B—monopole-like radiation pattern

V. CONCLUSION

In this paper, the extended bandwidth and compact size of ZOR antennas are obtained by introducing a truncated ground structure. The unit cells are implemented with the CRLH TL and inductor-loaded TL, respectively. A flexible design of a high shunt inductance and small shunt capacitance can realize a wider bandwidth and more compact size than those of the conventional ZOR antennas. Particularly, the maximum bandwidth of the proposed antennas can reach about 7.2%. The improved ZOR antennas are suitable for the use in wireless communication systems.

ACKNOWLEDGMENT

This work is supported in part by the National Natural Science Foundation of China (60901023), the NCET Foundation (11-0065) and the Fundamental Research Funds for the Central Universities (ZYGX2010J043).

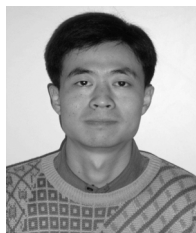
REFERENCES

- [1] V.-G. Veselago, "The Electrodynamics of Substance with Simultaneously Negative Values of ϵ and μ ," *Sov. Phys. Usp.* vol. 10, no. 4, pp. 509-514, Jan. 1968.
- [2] G.-V. Eleftheriades and K.-G. Balmain, "Negative Refraction Metamaterials: Fundamental Principles and Applications," New York, John Wiley & Sons, 2005.
- [3] G.-V. Eleftheriades, A.-K. Lyer, and P.-C. Kremer, "Planar Negative Refractive Index Media using Periodically LC Loaded Transmission Lines," *IEEE Trans. Microw. Theory Tech.*, vol. 50, no. 12, pp. 2702-2712, Dec. 2002.
- [4] R.-A. Shelby, D.-R. Smith, and S. Schultz, "Experimental Verification of a Negative Index of Refraction," *Science*, vol. 292, pp. 77-79, Apr. 2001.
- [5] A. Jafarholi and M. Kamyab, "Dipole Antenna a Miniaturization using Single-Cell Metamaterial," *Applied Computational Electromagnetics Society (ACES) Journal*, vol. 27, no. 3, pp. 261-270, Mar. 2012.
- [6] G. Antonini, "Reduced Order Modeling for Metamaterial Transmission Lines," *Applied Computational Electromagnetics Society (ACES) Newsletter*, vol. 21, no. 3, pp. 78-103, 2006.
- [7] N. Engheta and R.-W. Ziolkowski, *Physics and Engineering Explorations*, Wiley-IEEE Press, 1 edition, July,
- [8] G.-V. Eleftheriades, M.-A. Antoniades, and F. Qureshi, "Antenna Applications of Negative-Refractive Index Transmission-Line Structures," *IET Microw. Antenna Propag.*, vol. 1, no. 1, pp. 12-22, Feb. 2007.
- [9] S. Lim, C. Caloz, and T. Itoh, "Metamaterial-Based Electronically Controlled Transmission-Line Structures as a Novel Leaky-Wave Antenna with Tunable Radiation Angle and Beamwidth," *IEEE Trans. Microw. Theory Tech.*, vol. 53, pp. 161-173, Jan. 2005.
- [10] A. Sanada, M. Kimura, I. Awai, C. Caloz, and T. Itoh, "A Planar Zeroth-Order Resonator Antenna using a Left-Handed Transmission Line," *34th European Microwave Conf. Dig.*, Amsterdam, pp. 1341-1344, Oct. 2004.
- [11] G.-V. Eleftheriades, A. Grbic, and M. Antoniades, "Negative-Refractive-Index Transmission-Line Metamaterials and Enabling Electromagnetic Applications," *IEEE APS Int. Symp. Dig.*, Monterey, CA, pp. 1399-1402, June 2004.
- [12] A. Lai, K.-M.-K.-H. Leong, and T. Itoh, "Infinite Wavelength Resonant Antennas with Monopole Radiation Pattern Based on Periodic Structures," *IEEE Trans. Antennas Propag.*, vol. 55, no. 3, pp. 868-876, Mar. 2007.
- [13] F. Qureshi, M.-A. Antoniades, and G.-V. Eleftheriades, "A Compact and Low Profile Metamaterial Ring Antenna with Vertical Polarization," *IEEE Microw. Wireless Propag. Lett.*, vol. 4, pp. 333-336, 2005.
- [14] C.-J. Lee, K.-M.-K.-H. Leong, and T. Itoh, "Broadband Small Antenna for Potable Wireless Application," *iWat.*, pp. 10-13, Mar. 2008.
- [15] J. Zhu and G.-V. Eleftheriades, "A Compact Transmission Line Metamaterial Antenna with Extended Bandwidth," *IEEE Antenna Wireless Propag. Lett.*, vol. 8, pp. 295-298, 2009.
- [16] T. Jang, J. Choi, and S. Lim, "Compact Coplanar Waveguide (CPW)-Fed Zeroth-Order Resonant Antennas with Extended Bandwidth and High Efficiency on Vialess Single Layer," *IEEE Trans. Antennas Propag.*, vol. 59, no. 2, pp. 363-372, Feb. 2011.
- [17] J. K. Ji, G. H. Kim, and W. M. Seong, "Band Width Enhancement of Metamaterial Antennas Based on Composite Right/Left-Handed Transmission Line," *IEEE Antennas wireless Propag. Lett.*, vol. 9, pp. 36-39, 2010.
- [18] A. Sanada, C. Caloz, and T. Itoh, "Planar Distributed Structures with Negative Refractive Index," *IEEE Trans. Microwave Theory Tech.*, vol. 52, pp. 1252-1263, Apr. 2004.
- [19] D. Sievenpiper, L. Zhang, F.-J. Broas, N.-G. Alexopoulos, and E. Yablonovitch, "High-Impedance Electromagnetic Surfaces with a Forbidden Frequency Band," *IEEE Trans. Microwave Theory Tech.*, vol. 47, pp. 2095-2074, Nov. 1999.
- [20] Ansoft HFSS, ver. 10, ANSYS, Inc., Canonsburg, PA. Available: <http://www.ansoft.com/products/hf/hfss/>
- [21] D.-R. Smith, D.-C. Vier, Th. Koschny, and C.-M. Soukoulis, "Electromagnetic Parameter Retrieval from Inhomogeneous Metamaterials," *Phys. Rev. Lett.* E 71, 036617, 2005.
- [22] C. Caloz and T. Itoh, *Electromagnetic Metamaterials: Transmission Line Theory and Microwave Applications*, New York, Dec. 2005.



Jian Chao Liu received the B.E. degree in Information Engineering from Henan Institute of Science and Technology, Xinxiang, China, in 2009.

From September 2009 to now, he is pursuing the M. Sc. degree in Institute of Applied Physics in University of Electronic Science and Technology of China (UESTC), Chengdu, China. His current research interests include metamaterials and their applications.



Wei Shao received the M. Sc. and Ph. D. degrees in Radio Physics from the UESTC, Chengdu, China, in 2004 and 2006, respectively.

He joined the UESTC and is now an associate professor there. He has been a Visiting Scholar in the Electromagnetic Communication Laboratory, Pennsylvania State University in 2010. His research interests include the computational electromagnetics and antenna technique.

Efficient PEEC-Based Simulations using Reluctance Method for Power Electronic Applications

Danesh Daroui and Jonas Ekman

Department of Computer Science, Electrical and Space Engineering
Luleå University of Technology, Luleå, 971 87, Sweden
danesh.daroui@ltu.se, jonas.ekman@ltu.se

Abstract — This paper presents a partial element equivalent circuit (PEEC)-based solver that has been accelerated to exploit the massively parallel structure of graphics processing unit (GPU) technology, in order to employ a reluctance-based method in an efficient way. A grouping algorithm is also presented which makes reluctance calculation efficient, suitable for GPUs, and feasible even for very large problems. It has been shown that by using the reluctance method, the coefficient matrix in the system equation can be safely sparsified whilst the required accuracy is maintained. Because the calculation of the reluctance matrix includes matrix inversion, which is a task with high computational complexity, GPUs as cooperative units are utilized to reduce computational costs by taking advantage of parallelism. Two test models have been simulated and analyzed to benchmark the solver, and the results have been compared with the previously developed solver. Furthermore, analyzing the results reveals that the reluctance method makes it possible to use a considerably sparser system and thereby solve large problems by decreasing the memory demands and the solution time. It is also proven that the solution is reliable and accurate, whereas the problem has become noticeably smaller.

Index Terms - PEEC, electromagnetic simulation, reluctance, GPU.

I. INTRODUCTION

High frequency electronic circuits have a very important role in modern electronic devices. When the operational frequency of electronic devices is increased, magnetic and electrical

couplings can cause unexpected results, such as current imbalance, thermal hotspots and chip overload, in a high frequency circuit. Moreover, other phenomena such as signal distortion, crosstalk and ground bouncing [1] need to be taken into account. Examination of these phenomena, leads to electromagnetic compatibility (EMC) standards which demand the compliance with limitations for electromagnetic interferences. Therefore, studying susceptibility and emission is an important aspect of high frequency circuit design.

Various methods have been developed to address solutions for electromagnetic analysis. Among these methods, partial element equivalent circuit (PEEC) [2-5] is known to be suitable for combined electromagnetic and circuit analysis and has been widely used in power electronics, PCB design, antenna design and other industrial applications. As the complexity of the electrical systems and devices and the working frequency is increasing continuously [6], new acceleration techniques should be developed to solve real world problems in a reasonable time using limited computational resources. In previous works, other acceleration techniques have been used to increase the performance of the PEEC-based solver for general EMC applications, where no approximation is involved [7-8]. This paper presents a reluctance-based technique that can be employed to solve complex PEEC models in less time and with less memory consumption while some approximations are included in the final solution. A grouping algorithm is proposed to partition the geometry in 3D space and assemble the partial inductances into block diagonal form, to efficiently calculate the reluctance matrix.

Additionally, to the best knowledge of the authors of this article, no PEEC-based solver which is based on GPUs has been reported. However, since GPU technology is relatively new, hence the available hardware and software tools that have been employed in this research are strictly limited to the problems that can fit into GPU internal memories which are usually less than the main memory which is available on modern machines. The presented approach in this work is notably suitable for power electronic systems analysis, since capacitive couplings can be ignored and time retardation is not assumed in the simulations. It has been proven that using reluctances instead of partial inductances, makes it possible to eliminate a large amount of data from the equations, as long as the solution is kept to be accurate and valid [9]. On the other hand, calculation of the reluctance matrix is an expensive process and requires matrix inversion which has a high order in computational complexity which is $O(n^3)$ for a $n \times n$ matrix. In particular, for large structures that will result in large inductance matrices, reluctance calculation can be costly or even impossible to carry out. Hence, parallel processing approach in order to accelerate the reluctance calculation can be considered as a reasonable solution. Typically, modern processing units are enhanced with only few cores, whereas GPUs installed on modern graphic cards can offer processors with hundreds of cores and few GFLOPS of computational performance which makes these units appropriate for extensive and costly computations. Due to the high computational power and availability of GPUs, the technology has successfully used in many research areas, including electromagnetic simulations [10-12] and more specifically, FDTD [13][14] and Method of Moments [15]. It is also shown that the performance gained when a GPU is used is dependent on the problem size, which means that larger problems result in better speedups on GPU-enhanced graphic cards [15].

Fortunately, reluctance method in combination with sparsification techniques will bring a system of equations which consists of a sparse coefficient matrix. By having sparser systems, memory consumption will decrease, and sparse solvers can be used that can solve very large systems in less time than conventional direct solvers which are tailored for dense matrices. The

PEEC-based solver presented in this paper is based on reluctance technique when only inductive couplings exist in the model and capacitive couplings have been neglected. This assumption is primarily valid for applications in power electronics where high current electrical devices are studied where inductance extraction plays an important role because of high $\frac{di}{dt}$ which can cause high induced voltages in a circuit.

II. THE PEEC THEORY

This section gives a brief summary of the classical PEEC formulation. For further information, see [2-5].

A. Extraction of the equivalent circuit

The classical PEEC method is derived from the equation for the total electric field at a point [16] written as

$$\vec{E}^i(\vec{r}, t) = \frac{J(\vec{r}, t)}{\sigma} + \frac{\partial \vec{A}(\vec{r}, t)}{\partial t} + \nabla \phi(\vec{r}, t), \quad (1)$$

where \vec{E}^i is an incident electric field, J is a current density, \vec{A} is the magnetic vector potential, ϕ is the scalar electric potential, and σ is the electrical conductivity all at observation point \vec{r} . By using the definitions of the scalar and vector potentials, the current- and charge-densities are discretized by defining pulse basis functions for the conductors and dielectric materials. Pulse functions are also used for the weighting functions, resulting in a Galerkin type solution. By defining a suitable inner product, a weighted volume integral over the cells, the field equation (1) can be interpreted as Kirchhoff's voltage law over a PEEC cell consisting of partial self inductances between the nodes and partial mutual inductances representing the magnetic field coupling in the equivalent circuit. The partial inductances shown as L_{P11} and L_{P22} in Fig. 1 are defined as

$$L_{P\alpha\beta} = \frac{\mu}{4\pi} \frac{1}{a_\alpha a_\beta} \int_{a_\alpha} \int_{a_\beta} \int_{l_\alpha} \int_{l_\beta} \frac{dl_\alpha \bullet dl_\beta}{|\vec{r}_\alpha - \vec{r}_\beta|} da_\alpha da_\beta \quad (2)$$

for volume cell α and β . Figure 1 also shows the node capacitances which are related to the

coefficients of potential p_{ii} while ratios consisting of p_{ij}/p_{ii} are leading to the current sources in the PEEC circuit. The coefficients of potentials are computed as

$$P_{ij} = \frac{1}{S_i S_j} \frac{1}{4\pi\epsilon_0} \int_{S_i} \int_{S_j} \frac{1}{|\vec{r}_i - \vec{r}_j|} dS_j dS_i, \quad (3)$$

and a resistive term between the nodes is defined as

$$R_\gamma = \frac{l_\gamma}{a_\gamma \sigma_\gamma} \quad (4)$$

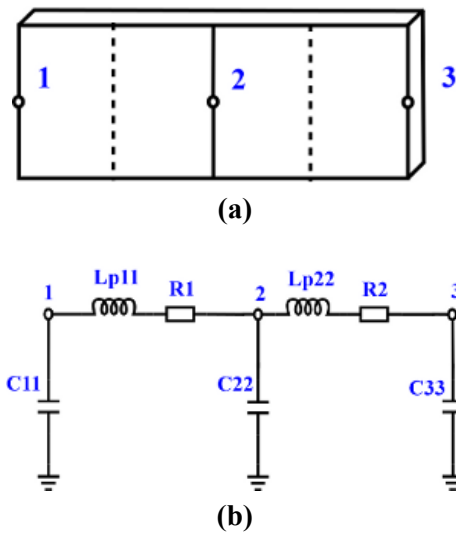


Fig. 1. Metal strip with 3 nodes and 2 cells (a) and corresponding PEEC circuit (b) (mutual couplings are not shown).

In (2), (3) and (4), a represents the cross section of the rectangular volume cell normal to the current direction γ , l is the length in the current direction and S is the charge surface cells. For a detailed derivation of the method, including the non-orthogonal formulation, see [17].

B. Solution of the equivalent circuit

The discretization process of the EFIE in (1) and the successive Galerkin's weighting leads to an equivalent circuit formulation. When Kirchhoff's voltage and current laws are enforced to the N_i independent loops and N_ϕ independent nodes of the PEEC equivalent circuit, the following equations are obtained

$$\begin{aligned} (j\omega P^{-1} + Y_L)I_L - A^T \phi &= I_S \\ -AI_L + (R + j\omega L_P)\phi &= V_S \end{aligned} \quad (5)$$

where

- $\phi \in \mathfrak{R}^{N_\phi}$ is the vector of node potentials to infinity; \mathfrak{R}^{N_ϕ} is the node space of the equivalent network;
- $I_L \in \mathfrak{R}^{N_i}$ is the vector of currents including both conduction and displacement currents; \mathfrak{R}^{N_i} is the current space of the equivalent network;
- L_P is the matrix of partial inductances describing the magnetic field coupling;
- P is the matrix of coefficients of potential describing the electric field coupling;
- Y_L is an admittance matrix describing the lumped components connected to the PEEC model;
- R is the matrix of cell resistances;
- A is the connectivity matrix which describes the current direction between each pair of nodes, assigned to each cell;
- V_S is the vector of distributed voltage sources due to external electromagnetic fields or lumped voltage sources;
- I_S is the vector of lumped current sources.

The equation system in (5) is equivalent to the circuit equations formulated in SPICE-type solvers for obtaining the solution in node voltages and branch currents. However, for PEECs the equation system in (5) contains denser matrices (L_P and P) than a pure electric network system solution due to the large number of mutually coupled inductors and mutual capacitances. Therefore, the solution of PEECs requires linear algebra packages suitable for dense matrices. The equation system in (5) is often entitled a Modified Nodal Analysis (MNA) formulation [18] and can be modified to suit the solution of PEECs [19]. Neglecting capacitive couplings from the PEEC model will lead to (6) which is the reduced form of (5) and discussed in this paper.

$$\begin{aligned} Y_L I_L - A^T \phi &= I_S \\ -AI_L - (R + j\omega L_P)\phi &= V_S \end{aligned} \quad (6)$$

The next section explains that how the dense system derived from MNA formulation is converted to a sparse system, without getting numerically unstable and invalid solution [20-21].

III. SPARSE MATRIX FORMULATIONS USING THE RELUCTANCE METHOD

In this section, the reluctance method and its application to sparsifying systems of linear equations in PEEC are discussed.

A. The reluctance method

From the partial inductance matrix L_p , the reluctance matrix K is defined as the inverse of L_p .

$$K = L_p^{-1} \quad (7)$$

By multiplying L_p with a vector of N branch currents, a vector containing the drop of the magnetic vector potential along each segment will be obtained, as shown in (8).

$$\begin{bmatrix} L_{11} & L_{12} & \dots & L_{1N} \\ L_{21} & L_{22} & \dots & L_{2N} \\ \vdots & \vdots & \vdots & \vdots \\ L_{N1} & L_{N2} & \dots & L_{NN} \end{bmatrix} \begin{bmatrix} i_1 \\ i_2 \\ \vdots \\ i_N \end{bmatrix} = \begin{bmatrix} \sum_{i=1}^N (\int A_{1i} d\vec{l}_1) \\ \sum_{i=1}^N (\int A_{2i} d\vec{l}_2) \\ \vdots \\ \sum_{i=1}^N (\int A_{Ni} d\vec{l}_N) \end{bmatrix} \quad (8)$$

$$\begin{bmatrix} K_{11} & K_{12} & \dots & K_{1N} \\ K_{21} & K_{22} & \dots & K_{2N} \\ \vdots & \vdots & \vdots & \vdots \\ K_{N1} & K_{N2} & \dots & K_{NN} \end{bmatrix} \begin{bmatrix} \sum_{i=1}^N (\int A_{1i} d\vec{l}_1) \\ \sum_{i=1}^N (\int A_{2i} d\vec{l}_2) \\ \vdots \\ \sum_{i=1}^N (\int A_{Ni} d\vec{l}_N) \end{bmatrix} = \begin{bmatrix} i_1 \\ i_2 \\ \vdots \\ i_N \end{bmatrix} \quad (9)$$

To extract values of the reluctance matrix, the linear equation system (9) should be solved. Therefore, unlike the elements of the partial inductance matrix, there is no formulation to calculate the reluctance values directly. Therefore, the L_p matrix is needed to calculate the K matrix. The physical meaning of K_{ij} is defined as the induced current in the i^{th} conductor (aggressor) when the total flux for the j^{th} conductor (victim) is equal to one and the total flux along each other conductor is set to zero. This

definition suggests that the induced current in victims should be in the opposite direction of the current in the aggressor to keep the flux around all victims at zero. These induced currents will generate magnetic fields around victims, which cancel the part of the field induced on the aggressor and shield the field on the aggressor from going farther. This phenomenon explains the locality (shielding effect) of the reluctance matrix [9]. The locality property of the method has been demonstrated in Fig. 2, where the third conductor results in a shorter arrow for the induced current, accounting for the overall effect. Figure 2 also shows the induced current in the third conductor, contributed to by two other bars, in dashed lines, and the overall effect of the induced currents using a solid line arrow. Because of this rippling effect of the magnetic field and the induced current, the value of each K_{ij} in the reluctance matrix represents the overall effect rather than a single active line. Therefore, the off-diagonal values in K would decrease more rapidly than L_p , which exhibits locality and the shielding effect of the reluctance matrix [22].

Like the capacitance matrix, the reluctance matrix is supposed to be symmetric positive definite and have the locality property [20]. Hence, only a small number of elements in the K matrix need to be kept to maintain an appropriate level of accuracy of the solution. The stability of the method is directly related to how the structure is discretized. It has been proven that stability is ensured for a sufficiently discretized structure [21].

B. Extraction of the reluctance matrix

As stated in the previous section, there is no formulation to calculate reluctance matrix directly and thus, the inductance matrix must be calculated first and then inversion carried out. Because matrix inversion is a cumbersome numerical task with time complexity of $O(n^3)$ for a $n \times n$ matrix, inverting a large matrix can highly degrade the overall performance of the solution. Several algorithms have been developed to overcome this problem by defining a window over a structure and then traversing the geometry using the window and the calculating the inductive couplings within the covered area and then finally

extract values for the reluctance sub-matrix [23][24]. In window-based approaches, the stability of the method is highly dependent on the window size. Further, choosing an unnecessarily large window in order to reach a high level of the accuracy can make the reluctance extraction computationally expensive and a small window will return inaccurate results. Therefore, finding an optimum size for the window to be traversed is crucial and usually challenging and hard to find.

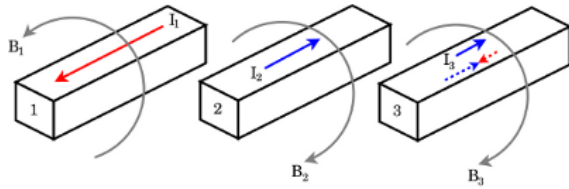


Fig. 2. The effect of reluctance on three parallel bars.

A novel approach to calculate reluctance matrix is proposed in this paper which is based on grouping the parts of the structure along axes, meaning that three main groups are created, which contain parts of the model in the x-, y- and z-axis. Because elements in each group are geometrically perpendicular to the other groups, there will be no inductive couplings between groups and only couplings within each group are considered. This assumption leads to the existence of a block diagonal partial inductance matrix where each block can simply be inverted to determine the reluctance matrix. The total process of inverting all blocks is substantially less costly than inverting the whole matrix. By holding the assumption that the studied structure is uniformly placed in the space along all three axes, each block will have

roughly the dimension size of $\frac{1}{3}$ of the dimensions of partial inductance matrix, as shown in (10). By substituting (10) into (11), the time complexity of the inversion of the original matrix is compared to the time complexity of the inversion of each block. According to (11), the maximum speedup that can be achieved is approximately 9, which is a worthwhile improvement in the performance. Moreover, it can be concluded that the reluctance calculation can be

a bottleneck in the total solution. Thus, a massively parallel approach using GPU technology to accelerate the performance of this part of the solution is a reasonable solution.

$$n_x \approx \frac{n}{3}, n_y \approx \frac{n}{3}, n_z \approx \frac{n}{3} \quad (10)$$

$$\frac{O((n_x + n_y + n_z)^3)}{O(n_x^3) + O(n_y^3) + O(n_z^3)} \leq 9 \quad (11)$$

Figure 3 depicts the reluctance matrix, calculated from a block diagonal partial inductance matrix, where each block which represents parts of the model in each axis, is inverted separately.

$$K = \begin{bmatrix} \tilde{L}_{p_x}^{-1} & & \\ & \tilde{L}_{p_y}^{-1} & \\ & & \tilde{L}_{p_z}^{-1} \\ & & & 0 \end{bmatrix}$$

Fig. 3. Calculating reluctance from an inductance matrix in block diagonal form.

C. Reluctance formulation in PEEC

In this paper, only quasi-static (R,Lp)PEEC is studied, where capacitive couplings are neglected in the problem. This assumption is mostly valid in power electronics and for the models that carry high currents, e.g. bus bars in power frequency converters, where inductive loops are interesting to be identified and studied in

order to simulate the induced voltage when $\frac{di}{dt}$ is

high in such a circuit. Extracting inductance values in high frequency power electronics circuits will help to improve the layout design to reduce the stray inductance and consequently reduce voltage overshoots and reduce switching losses. Based on the MNA formulation in PEEC, the system equation for an (R,Lp)PEEC model is defined as

$$\begin{bmatrix} Y_L & -A^T \\ -A & R + j\omega L_p \end{bmatrix} \begin{bmatrix} \phi \\ I_L \end{bmatrix} = \begin{bmatrix} I_S \\ V_S \end{bmatrix} \quad (12)$$

All elements in (12) are described in Section II-B. In system equation (12), the right hand side is for excitation sources and the unknowns in the equation are *node potential* and *cell currents*.

By applying the reluctance matrix, as defined in (7) to both sides of (12), the new formulation which is shown in (13) will be achieved. This new formulation is introduced as (R,K)PEEC.

$$\begin{bmatrix} Y_L & -A^T \\ -KA & KR + j\omega I \end{bmatrix} \begin{bmatrix} \phi \\ I_L \end{bmatrix} = \begin{bmatrix} I_S \\ KV_S \end{bmatrix} \quad (13)$$

IV. PEEC-BASED SOLVER

This section describes a solver developed based on the PEEC method. Details about solver acceleration using GPUs and sparse solver are also presented in this section.

A. Implementation of the solver

A PEEC-based solver has been written in the C++ language, which utilizes the Intel Math Kernel Library (MKL) [25], optimized for multi-core systems, and the CUDA-based LAPACK (CULA) [26], which is included for the parts of the solver that use the GPU. To solve the sparse system after applying the reluctance matrix, the MUMPS package [27] is used. After calculating each block of the reluctance matrix, it can safely be sparsified. The sparsification can be described as applying a truncation process to small off-diagonal elements in the reluctance matrix by means of the *coupling factor*

$$k_{ij} = \sqrt{\frac{K_{ij}^2}{|K_{ii}| \cdot |K_{jj}|}} \quad (14)$$

between the elements i and j in the matrix. The calculated factor will be compared to a constant value and values that are smaller than the constant will be removed [28]. The approximation in (13) comes from the relation in (15), which is due to the sparsified reluctance matrix. As the K matrix is more sparsified, (15) is more approximate. Similarly, if K matrix is not sparsified at all, the equation $KL_p = I$ will hold which leads to the exact solution.

$$KL_p \approx I \quad (15)$$

It should be noted that, sparser reluctance matrices will create sparser coefficient matrices, which will speed up the solving process. Moreover, due to the locality property of the reluctance matrix, K can be sparsified up to a high level, at which the desirable level of accuracy is still maintained [22]. In a PEEC-based solution, the coefficient matrix in the MNA formulation consumes the largest part of the total allocated memory. Using (R,K)PEEC, this matrix is converted to a sparse matrix where the majority of its elements are set to zero. Thus, the solver assembles the matrix, in a row-by-row manner, and at each step, the assembled row is stored in sparse format to save the memory. Sparse direct solvers involve much more complicated algorithms than solvers suited for dense systems. This class of solvers is used to solve the matrix equation $Ax = b$, where the coefficient matrix A is considered to be large and sparse. The main challenge in these types of solvers is the efficient fill-in of the L and U factors of a sparse system. Typically, matrices in PEEC are dense, unsymmetric, indefinite and ill-conditioned. By sparsifying such matrices, the system becomes even closer to being singular and thereby would need numerical techniques, i.e. pivot perturbation or iterative refinement, to compensate for numerical instabilities. Later, by acquiring a valid sparse system, MUMPS will be utilized as an appropriate solver for this purpose [27]. For unsymmetric matrices, MUMPS first tries to symmetrize the matrix, based on the pattern $A + A^T$, and then reorder the matrix to minimize the cost of the factorization. This process, which is known as symbolic factorization, is necessary to determine the non-zero structure of the factors, before performing any numerical factorization. By having a matrix equation where the coefficient matrix is symmetric, the symbolic factorization can be performed as

$$\psi A \psi^T = LDU \quad (16)$$

where

- A is the sparse coefficient matrix;
- ψ is the permutation matrix that reorders A ;

- L and U are triangular matrices, parts of the factorized A ;
- D is a diagonal matrix, a part of the factorized A .

Using the MUMPS package, various methods for reordering are available, e.g. Approximate Minimum Degree (AMD) [29] and METIS [30]. The reordering can also be performed by providing the solver with a permutation matrix ψ . Using a sparse direct solver, the solution is carried out in three main steps:

1. *Analysis*: The symbolic factorization, which involves reordering, is performed on the symmetric pattern of the coefficient matrix. Permutation applies on the row and columns of the original matrix through a permutation matrix which consists of a set of orthogonal reordering vectors.
2. *Factorization*: By having symbolic data, the numerical factorization is performed using a numerical pivoting method. In the case of detecting zero pivots, perturbation will be performed by the sparse solver. The perturbations can affect the accuracy of the results. The accuracy will be retained by iterative refinement steps after the solution is done.
3. *Solution*: The factorized system is solved in this phase, using backward-forward substitution. As mentioned, some iterative refinement steps are also performed to correct the effect of possible perturbations.

Due to the structure of the sparse coefficient matrix in (R,K)PEEC formulation, many of the diagonal elements are set to zero, which can easily cause the final solution to become numerically unstable. Thus, certain algorithms known as *weighted matching* and *scaling* are used by the solver, to increase the accuracy of the pivoting [31]. MUMPS offers several remedies, and it is very important to choose a proper algorithm for this purpose. During several experiments, it was observed that when no scaling was applied, a few unwanted spikes could appear in the solution. On the other hand, when the scaling algorithms were applied, the spikes didn't appear and accurate

results were acquired. Figure 4 depicts the effect of using scaling to solve a linear equation. It is observed that spikes do not appear in the final solution when a scaling feature with more accurate pivoting is enabled.

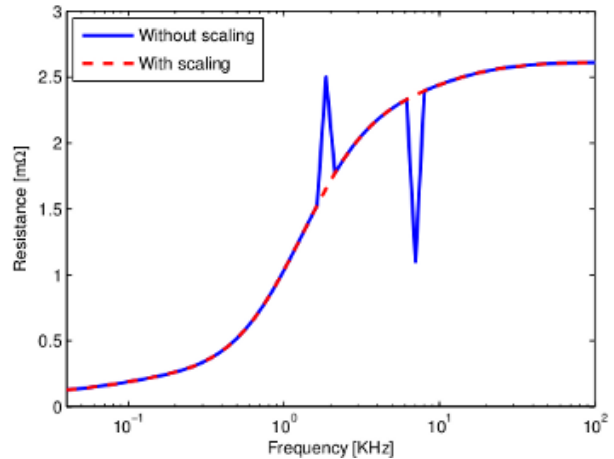


Fig. 4. The effect of scaling on the accuracy of pivoting during the factorization of an ill-conditioned sparse coefficient matrix.

B. GPU Acceleration

According to (10) and (11), grouping the structure along each axis can improve the performance of the reluctance calculation up to a factor of 9. Therefore, massively parallel solutions can be used to speed up this process. In the implemented PEEC-based solver, each block of the reluctance matrix is calculated in the following steps:

1. Calculate each block of the partial inductance matrix;
2. Transfer the calculated block from the host to the GPU device;
3. Invert the transferred block on the GPU device;
4. Transfer the inverted block back to the host;
5. Sparsify the block, and store it in sparse format;
6. Release the memory for that block.

Because the solver uses complex double precision data to solve problems in the frequency domain, NVIDIA Fermibased GPUs are exploited in this research. NVIDIA Fermibased M2050

Tesla series graphic cards offer 448 CUDA cores with 3 GB internal memory and have the computational power of 515 GFLOPS which makes them appropriate for expensive mathematical calculations [32].

The inversion using the GPU is performed by calling a CULA-appropriate routine [26]. Then, the routine will transfer the whole block of data to the graphic card's internal memory, to minimize the communication overhead, and will invert it using the massively parallel structure of the graphic card. When the inversion has been completed, the solution is transferred back to the main memory of the host system. Since the internal memory of available GPUs is commonly less than the available memory on the modern machines, thus the problem size is limited to the size of the internal memory on the graphic cards. In the future, with more powerful GPUs with larger memory and advances in the software tools which could partition the data into blocks which could be solved separately on GPUs, it would be possible to perform the whole solution solely on GPUs. CULA routines use some reserved memory for internal usage, where this workspace is allocated on both the GPU memory and the main memory [32]. The process of inversion is actually performed by both the host CPU and all processing cores on the GPU. However, the computations are mostly handled by the cores available on the GPU.

Additionally, the sparse solver has been compiled to use BLAS [33] operations on the GPU. Hence, all BLAS operations of the solver are performed by the GPU to reach the highest level of parallelism.

V. RESULTS

In this section, the performance of the solver will be studied using a PEEC model of a interconnection bus bar as a part of a power frequency converter. The analyzed model consists of a planar DC-link bus bar as typically used in multi-level medium voltage frequency converters [34]. The purpose of the DC-link in a multi-level

frequency converter is to store the energy between the front-end rectifier and back-end inverter units, and the DC-link must therefore be designed for low stray inductance to limit the overvoltage peaks when switching high currents. Furthermore, the requirements and complexity of the bus bar strongly depend on the circuit topology used for power conversion [35]. The simulation model is depicted in Fig. 5.

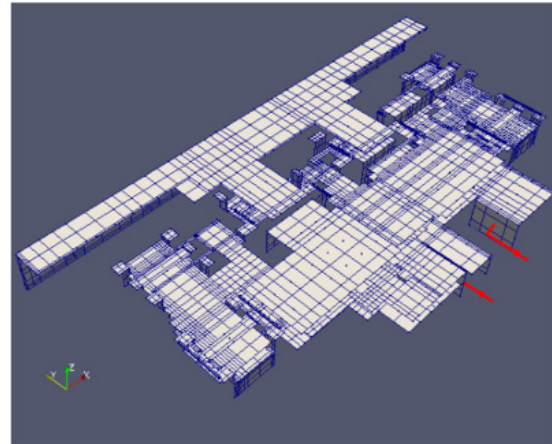


Fig. 5. PEEC model of the studied bus bars.

In the modeled bus bars, a current source with the amplitude of 1A is connected between two ports, which are marked two arrows which point to the connection ports. The simulation has been performed from 1 Hz to 10 MHz using 10 frequency steps. The total resistance and inductance of the bars has been extracted from the simulation. Two different test cases of the same model with different mesh densities have been analyzed. In these tests, the dense solver utilizes the Intel MKL library, while the sparse solver uses the reluctance method together with the sparse direct solver MUMPS. All simulations have been run on a Linux 64-bit cluster, equipped with two quad-core Intel Xeon E5520 2.2 GHz processors with 24 GB of RAM installed and a Tesla M2050 card with 3 GB of on-board memory.

Table 1: Bus bar solution

Model	Solver	Num. of unknowns	Mem. [GB]	Sparse [%]	Time [hh:mm:ss]
BB1	Dense	33 296	17.7	0	06:34:10
	Sparse		13.3	0	01:56:50
	Sparse		0.8	95	01:00:22
	Sparse		0.5	98	00:40:00
BB2	Dense	58 668	55	0	-*
	Sparse		41.5	0	-*
	Sparse		6.6	95	10:12:02
	Sparse		2.8	98	08:10:28

-*: Not available due to memory

Table 1 shows the simulation results of each test case using different levels of sparsification. Figures 6 and 7 present the total resistance and inductance of the bus bars as the frequency increases. It should be noted that for the first test case, the results for the case which the reluctance matrix is sparsified up to 95% almost overlaps the results without any sparsification. Moreover, results from the second test model reveal that as the problem size increases, the error rate decreases when the reluctance matrix gets sparser. Figures 6 and 7 also demonstrates the skin and proximity effects along the bus bars, where, as the frequency increases resistance increases and inductance decreases to a certain level.

From Figs. 6 and 7 and Table 1, several conclusions can be drawn:

- The highest error in the results occurs when the sparsification is up to 98%. However, this error is still adequate and less than 8%.
- Although the reluctance matrix is sparsified up to 98%, the error is still quite low. Moreover, despite this acceptable error in the results, for the smallest model, the speed and memory usage has been improved by factors of approximately 10 and 35, respectively. It is also evident that problems that could not be solved before, due to the lack of the memory (i.e. BB2), can now be solved with small approximations involved in the solution.
- For reluctance calculations, the GPU solution results in a remarkable speedup, compared to the CPU-only solution. The speedup increases even more as the problem size increases. For the first test case, reluctance calculation took 110 and 57 seconds for CPU and GPU respectively and the second test case, reluctance calculation was carried out in 437

and 120 seconds for CPU and GPU respectively. As stated before, all matrix operations have also been done on GPU which improved the overall solution. It is expected that higher speedup will be achieved when graphic cards with higher internal memories are manufactured. Furthermore, at each time, only one block of the inductance matrix shown in Fig. 3 is transferred to the GPU. Thus, the memory peak is always decreased to the largest block in the inductance matrix.

- In Table 1, the dense solver indicates the solver which uses only CPU resources while the sparse solver uses CPU together with GPU resources, since it performs all BLAS operations on GPU. Comparison between dense and sparse solvers with no sparsity, reveals that the GPU have contributed to gain a speedup around 3.4 to solve exactly the same problem.
- Smaller problems loose the accuracy faster than larger problems when the reluctance matrix is sparsified in the same level. Comparison between two analyzed structures, yields that BB1 showed 8% error when the reluctance matrix is 98% sparsified while BB2 had only 3% error with the same level of sparsification, comparing to the cases when 95% sparsification is applied.
- The parallel sparse direct solver shows better performance than the dense solver even when the reluctance matrix is not sparsified at all. This performance increase can be due to the nature of the coefficient matrix in the MNA formulation in the PEEC, which is relatively sparse, and the efficiency of the sparse solver for sparse systems.

VI. CONCLUSION AND FURTHER WORK

The improved solver presented in this paper makes it possible to solve very large problems with limited computational resources. Using the reluctance method, the final coefficient matrix in the system equation can be sparsified without the risk of an unstable solution, due to the diagonal dominance of the reluctance matrix. In the new solver, the bottleneck of the solution is shifted to the reluctance matrix calculation. Therefore, utilizing GPU technology together with grouping algorithms is the key to improving the performance in this phase of the solution. A numerical test case was studied which proved that even by sparsifying the reluctance matrix up to a high level (i.e. 98%) the required accuracy was still satisfied. In addition, memory usage and the grouping algorithms were analyzed, showing that, using grouping strategy, the reluctance matrix can be computed by inverting sub-matrices, which is less expensive and more efficient than inverting the whole L_p matrix. It was also observed that, even when no sparsification is applied to the system, the direct sparse solver performs more efficiently than conventional dense solvers. Because of the relatively sparse matrices involved in MNA formulations, which make sparse solvers more appropriate for this purpose. For the next step, the iterative solvers can be considered for use with the PEEC-based solver. Using iterative solvers, the time complexity of the solution can be reduced, but because of the severely ill conditioned matrices that are involved in the PEEC method, the development of a proper preconditioner will be a challenging and critical task. Finally, the iterative PEEC-based solver can be enhanced to employ GPU hardware. The workload of preconditioning and Krylov subspace solver can be shared between the host and GPU to acquire maximum efficiency and the parallelism.

ACKNOWLEDGMENT

The authors would like to thank ABB for providing bus bars models for this work.

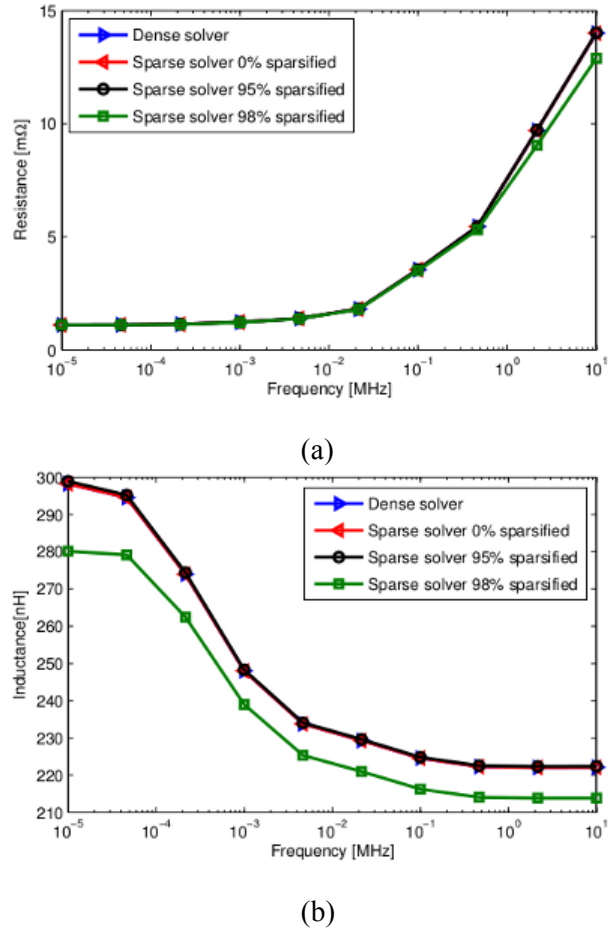


Fig. 6. Bus bar resistance (a) and inductance (b) of the BB1 model, simulated using dense and sparse solvers with different sparsification levels.

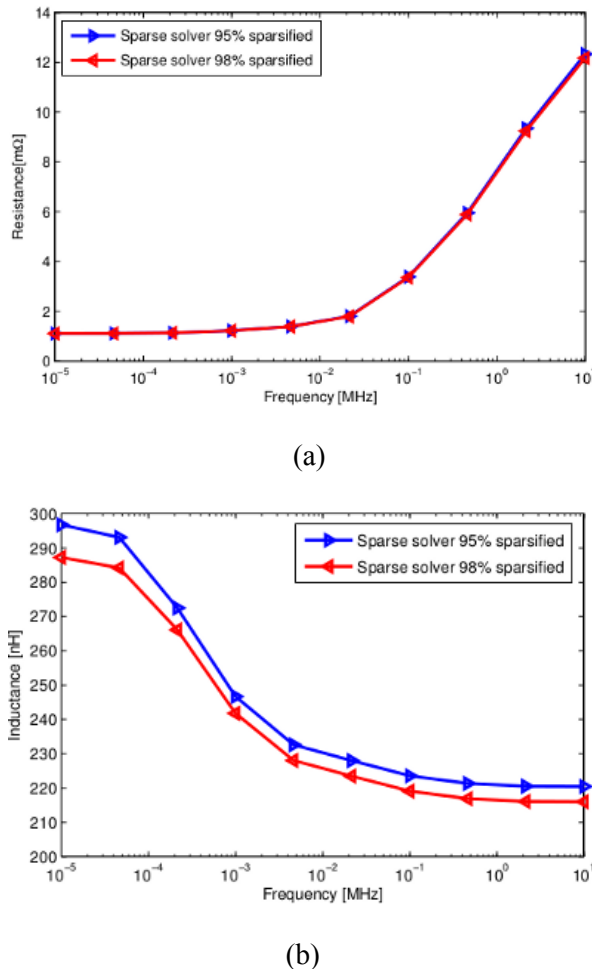


Fig. 7. Bus bar resistance (a) and inductance (b) of the BB2 model, simulated using dense and sparse solvers with different sparsification levels.

REFERENCES

- [1] A. Nishizawa, M. Shimazaki, and S. Tanabe. "Ground Bouncing Analysis Using a Program Linking FDTD and SPICE," *In Proc. of Int. Symposium on Electromagnetic Compatibility*, Seattle, WA, USA, 1999.
- [2] A. E. Ruehli. "Equivalent Circuit Models for Three Dimensional Multiconductor Systems," *IEEE Transactions on Microwave Theory and Techniques*, MTT-22, no. 3, pp. 216-221, March 1974.
- [3] A. E. Ruehli. "Inductance Calculations in a Complex Integrated Circuit Environment," *IBM Journal of Research and Development*, vol. 16, no. 5, pp. 470-481, September 1972.
- [4] A. E. Ruehli, P. A. Brennan. "Efficient Capacitance Calculations for Three Dimensional Multiconductor Systems," *IEEE Transactions on Microwave Theory and Techniques*, MTT-vol. 21 no. 2 pp. 76-82, February 1973.
- [5] Z. Song, F. Duval, D. Su, and A. Louis. "Stable Partial Inductance Calculation for Partial Element Equivalent Circuit Modeling," *Applied Computational Electromagnetics Society (ACES) Journal*, vol. 25, no. 9, 2010.
- [6] G. Antonini, G. Miscione, and J. Ekman. "PEEC Modeling of Automotive Electromagnetic Problems," *Applied Computational Electromagnetics Society (ACES) Newsletter*, vol. 23, no. 1, pp. 39-50, March 2008.
- [7] D. Daroui and J. Ekman. "Parallel Implementation of the PEEC Method," *Applied Computational Electromagnetics Society (ACES) Journal*, vol. 25, no. 5, pp. 410-422, May 2010.
- [8] D. Daroui and J. Ekman. "Performance Analysis of Parallel Nonorthogonal PEEC-based Solver for EMC Applications," *Progress In Electromagnetics Research B*, vol. 41, pp. 77-100, 2012.
- [9] H. Ji, A. Devgan, and W. Dai. "KSPICE: Efficient and Stable RKC Simulation for Capturing On-chip Inductance Effect," *Technical Report*, University of California, April 2000.
- [10] Y. B. Tao, H. Lin, and H. J. Bao. "From CPU to GPU: GPU-based Electromagnetic Computing (GPUECO)," *Progress In Electromagnetic Research*, vol. 8, no. 1, pp. 1-19, 2008.
- [11] M. J. Inman and A. Z. Elsherbeni. "GPU Acceleration of Linear Systems for Computational Electromagnetic Simulations," *In Proc. of the IEEE Int. Symposium on Antennas and Propagation Society*, Charleston, SC, USA, 2009.
- [12] M. Ujaldon. "Using GPUs for Accelerating Electromagnetic Simulations," *Applied Computational Electromagnetics Society (ACES) Journal*, vol. 25, no. 4, 2010.
- [13] M. J. Inman and A. Z. Elsherbeni. "FDTD Calculations using Graphical Processing Units," *In Proc. of the IEEE Conf. on Wireless Communications and Applied Computational Electromagnetics*, HI, USA, 2005.
- [14] V. Demir and A. Z. Elsherbeni. "Compute Unified Device Architecture (CUDA) Based Finite-Difference Time-domain (FDTD) Implementation," *Applied Computational Electromagnetics Society (ACES) Journal*, vol. 25, no. 4, pp. 303-314, April 2010.
- [15] T. Topa, A. Karwowski, and A. Noga. "Using GPU with CUDA to Accelerate MoM-based Electromagnetic Simulation of Wire-grid Models," *IEEE Antennas and Wireless Propagation Letters*, vol. 10, pp. 324-345, 2011.
- [16] S. Ramo, J. R. Whinnery and T. Van Duzer, *Fields and Waves in Communication Electronics*, John Wiley and Sons, 1994.

- [17] A.E. Ruehli, G. Antonini, J. Esch, A. Mayo J. Ekman, and A. Orlandi. "Non-orthogonal PEEC Formulation for Time and Frequency Domain EM and Circuit Modeling," *IEEE Transactions on Electromagnetic Compatibility*, vol. 45, no. 2, pp. 167-176, May 2003.
- [18] C. Ho, A. Ruehli, P. Brennan. "The Modified Nodal Approach to Network Analysis," *IEEE Transactions on Circuits and Systems*, pp. 504-509, June 1975.
- [19] G. Antonini, J. Ekman, and A. Orlandi. "Full Wave Time Domain PEEC Formulation using a Modified Nodal Analysis Approach," *In Proc. of EMC Europe*, Eindhoven, The Netherlands, 2004.
- [20] T.-H. Chen, C. Luk, H. Kim, C C.P. Chen. "Inductance-wise Interconnect Simulator and Extractor," *In Proc. of the IEEE Int. Conf. on Computer Aided Design*, pp. 215-220, San Jose, CA, Nov 2002.
- [21] H. Ji, A. Devgan, and W. Dai. "Ksim: A Stable and Efficient RKC Simulator for Capturing On-chip Inductance Effect," *In Proc. of Design Automation Conference*, CA, USA, 2001.
- [22] C. Luk. "Efficient Inductance Extraction for On-chip Interconnect," *Technical report*, University of Wisconsin-Madison, 2003.
- [23] S. Zenga, W. Yu, J. Shi X, Hong, and C. Cheng. "Efficient Partial Reluctance Extraction for Large-scale Regular Power Grid Structures," *IEICE Transactions on Fundamentals*, E92-A, no. 6, June 2009.
- [24] G. Zhong, C. Koh, V. Balakrishnan, and K. Roy, "An Adaptive Window-based Susceptance Extraction and its Efficient Implementation," *In Proc. of Design Automation Conference*, IN, USA, 2003.
- [25] Intel Math Kernel Library (MKL). Online: <http://software.intel.com/en-us/articles/intel-mkl/>.
- [26] CULA A set of GPU-accelerated linear algebra libraries. Online: <http://www.culatools.com/>.
- [27] MUMPS A parallel sparse direct solver. Online: <http://graal.ens-lyon.fr/MUMPS/>.
- [28] M. L. Zitzmann. "Fast and Efficient Methods for Circuit-based Automotive EMC Simulation", *PhD thesis*, University of Erlangen-Nürnberg, February 2007.
- [29] P. R. Amestoy, T. A. Davis, and I. S. Duff. "An Approximate Minimum Degree Ordering Algorithm," *SIAM Journal on Matrix Analysis and Applications*, vol. 17, pp. 886-905, 1996.
- [30] METIS A Software Package for Partitioning Unstructured Graphs, Meshes, and Computing Fill-Reducing Orderings of Sparse Matrices. Online: <http://glaros.dtc.umn.edu/gkhome/views/metis/>.
- [31] Iain S. Duff. "Developments in Matching and Scaling Algorithms," *Proc. of Appl. Math. Mech.*, vol. 7, no. 1, Aug 2007.
- [32] The Tesla M class GPU modules. Online: <http://www.nvidia.com/object/preconfigured-clusters.html>.
- [33] K. C. Huang, P. C. Wu, and F. J. Wang. "Parallelizing a Level 3 BLAS Library for LAN-Connected Workstations," *In Proc. of Second Symposium on Autonomous Decentralized Systems*, Arizona, USA, April 1995.
- [34] S. Van Acker, P. Salenbien, and A. Cosaert. "Predictability of the Behavior of Power Distribution Components in Power Conversion Applications," *In PCIM Conference*, Shanghai, China, March 2005.
- [35] A. Rodríguez, J. S. Lai, and F. Z. Peng. "Multilevel Inverters: A Survey of Topologies Controls, and Applications," *IEEE Transactions on Industrial Electronics*, vol. 49, no. 4, August 2002.

Method of Moments (MoM) Modeling for Resonating Structures: Propagation inside a Parallel Plate Waveguide

G. Apaydin ¹, L. Sevgi ^{2,3}

¹Department of Electrical-Electronics Engineering
Zirve University, Gaziantep, 27260, Turkey
gokhan.apaydin@zirve.edu.tr

²Department of Electronics and Communications Engineering
Dogus University, Istanbul, 34722, Turkey
lsevgi@dogus.edu.tr

³Department of Electrical and Computer Engineering
University of Massachusetts Lowell (UML), Massachusetts, 01854, USA
levent_sevgi@uml.edu

Abstract — Method of Moments (MoM) modeling inside resonating structures is discussed and a novel approach called Multi-MoM (Mi-MoM) is proposed. Propagation inside a two-dimensional (2D) non-penetrable parallel plate waveguide is taken into account. The Mi-MoM results are compared with the analytical reference solution. Practical ways of different source representations (untilted/tilted Gaussian beams) are also presented. Finally, surface irregularities inside the waveguide and their effects on the propagation are modeled with both Mi-MoM and the Split-Step Parabolic Equation (SSPE) method.

Index Terms - computational electromagnetics, gaussian beam, Green's function, method of moments, mode summation, MoM, parallel plate waveguide, propagation, split step parabolic equation, SSPE.

I. INTRODUCTION

Method of Moments (MoM) [1] is one of the oldest numerical electromagnetic (EM) model. In this method, first a discrete model of the object under investigation is created from small pieces (compared to wavelength) called segments or patches. Everything on these segments is assumed constant. Then, an $N \times N$ system of equations is built with N unknown segment/patch currents, N known segment voltages, calculated from the

Green's function of the problem, and known $N \times N$ segment/patch impedances. The model is closed-form and stable, but necessitates high memory and high speed computers especially for high frequency applications (it requires N^3 operations). It requires the Green's function of the problem. MoM has been successfully applied to broad range of EM scattering problems (see, for example [1-4] for some of the applications). MoM with some acceleration techniques (e.g., Forward-Backward Spectral Acceleration - FBSA) has also been applied to propagation problems [5-7], especially to long-range ground wave propagation over irregular and lossy Earth.

Propagation modeling inside waveguides with irregular and lossy boundaries has become important because of signaling requirements through railway tunnels, communication in mines, screening in printed circuit boards (PCB), etc. The Split-Step Parabolic Equation (SSPE) and Finite Element based PE models to these guiding structures have been developed and calibrated against analytical reference data in [8]. MoM suffers from resonances in these waveguiding structures [9-10] therefore its direct application is a challenge. Here, a novel Multi-Iteration MoM model (Mi-MoM) is introduced for this purpose. Propagation inside a two-dimensional (2D), non-penetrable parallel plate waveguide is taken into account. The novel Mi-MoM model is compared

against analytical reference data (generated from the exact mode summation model), as well as against SSPE [8-9].

Propagation inside a parallel plate waveguide is an interesting EM problem where both analytical and numerical models can be tested one against the others [11-12]. It can also be used for calibration. The Green's function solution (i.e., EM response of a line source) is exact but requires infinite number of mode (eigenfunction) summation [11]. This is a numerical challenge especially in the near vicinity of the line source. Modes are grouped into two; propagating modes (with real eigenvalues) and evanescent modes (with complex eigenvalues). The number of propagating modes depends on the frequency and width of the plate. A tilted directional antenna can also be located inside and can be modeled in terms of modes, but modal excitation coefficients become complex. This is another numerical challenge, especially at high frequencies when the number of propagating modes is extremely high. The modes are global therefore do not suffer from local problems, but extraction of modal excitation coefficients is crucial when generating reference solutions. Analytical exact solution can also be constructed in terms of rays which are local wave pieces; again summation of infinite number of rays is required for the line source excitation [12]. Moreover, eigenray extraction might have numerical problems.

II. THE 2D GREEN'S FUNCTION PROBLEM AND ANALYTICAL REFERENCE SOLUTION

The 2D parallel plate waveguide is pictured in Fig. 1. Here, x and z are the transverse and longitudinal coordinates, respectively. The structure is infinite along y -direction ($\partial/\partial y \equiv 0$). The width of the waveguide is a . The PEC boundaries are assumed Dirichlet-type for the TE_z (transverse electric with respect to z) problem and Neumann-type for the TM_z (transverse magnetic with respect to z) problem (see [13] for TE/TM discussions).

Since the TE_z and TM_z sets are decoupled, each can be excited independently of the other by appropriate selection of the sources, \mathbf{J} and \mathbf{M} . The line sources M_x, M_z, J_y excite the TE_z set, whereas the line sources M_y, J_x, J_z excite the TM_z set.

Further simplification can be obtained by setting the source components $M_x=0, M_z=0$ for the TE_z set, and $J_x=0, J_z=0$ for the TM_z set.

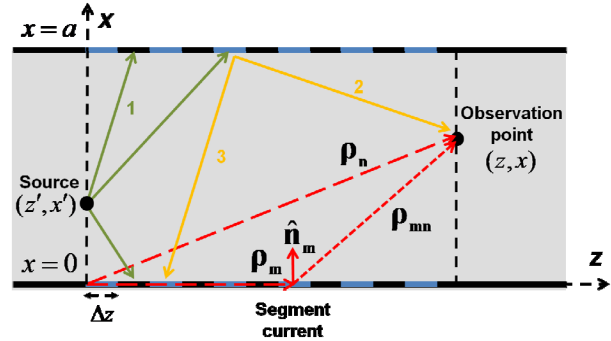


Fig. 1. The non-penetrable (PEC) parallel plate waveguide, x : height, z : range and tilt is measured from z -axis (“+” for forwards, “-” for downwards).

The Green's function problem (under $\exp(j\omega t)$ time dependence) associated with both the TE_z set (when $M_x=M_z=0$) and the TM_z set (when $J_x=J_z=0$) is postulated as:

$$\left\{ \frac{\partial^2}{\partial x^2} + \frac{\partial^2}{\partial z^2} + k_0^2 \right\} g(x, z; x', z') = \delta(x-x')\delta(z-z'), \quad (1)$$

with the boundary conditions (BC)

$$g(x, z; x', z') = 0 \quad \text{at } x = 0, a \quad (TE_z), \quad (2a)$$

$$\frac{\partial}{\partial x} g(x, z; x', z') = 0 \quad \text{at } x = 0, a \quad (TM_z), \quad (2b)$$

$$g(x, z; x', z') = 0 \quad \text{as } z \rightarrow \pm\infty. \quad (2c)$$

Here, (x', z') and (x, z) specify source and observation points, respectively, $\delta(\cdot)$ is the Dirac delta function, $k_0 = 2\pi/\lambda = \omega\sqrt{\epsilon_0\mu_0}$ is the free-space wave-number, and λ is the free-space wavelength.

The Green's function $g(x, z; x', z')$ can be obtained as

$$g(x, z; x', z') = \tilde{g}(z; z') + \frac{2}{a} \sum_{m=1}^{\infty} \frac{e^{-jk_{zm}|z-z'|}}{2jk_{zm}} \Psi(k_{xm}x) \Psi(k_{xm}x'), \quad (3)$$

$$\tilde{g}(z; z') = 0, \Psi(x) = \sin(x) \quad (TE_z), \quad (4a)$$

$$\tilde{g}(z; z') = \frac{1}{a} \frac{e^{-jk_0|z-z'|}}{2jk_0}, \Psi(x) = \cos(x) \quad (TM_z), \quad (4b)$$

where $k_{xm} = m\pi/a$, $k_{zm} = \sqrt{k_0^2 - k_{xm}^2}$. The line-source-excited fields are then given by either

$E_y = j\omega\mu_0 g$ or $H_y = j\omega\varepsilon_0 g$ for the TE_z and TM_z cases, respectively. The remaining field components can be calculated from

$$H_x = \frac{1}{j\omega\mu_0} \left\{ \frac{\partial E_y}{\partial z} - M_x \right\}, \quad (5a)$$

$$H_z = -\frac{1}{j\omega\mu_0} \left\{ \frac{\partial E_y}{\partial x} + M_z \right\}, \quad (5b)$$

for the TE_z model and

$$E_x = -\frac{1}{j\omega\varepsilon_0} \left\{ \frac{\partial H_y}{\partial z} + J_x \right\}, \quad (6a)$$

$$E_z = \frac{1}{j\omega\varepsilon_0} \left\{ \frac{\partial H_y}{\partial x} - J_z \right\}, \quad (6b)$$

for the TM_z model.

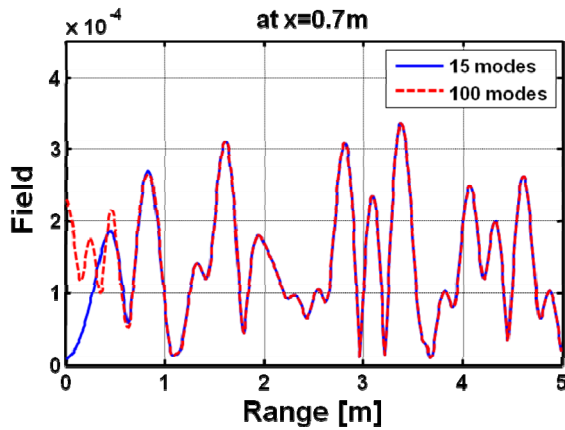


Fig. 2. Field vs. z (TM_z case): (Solid) only 15 propagating modes, (Dashed) The first 100 modes ($a=1$ m, $z'=0$, $x'=0.3$ m, $x=0.7$ m, $k_0 a=50$).

A short MatLab code is prepared for the calculation of field distribution inside the parallel plate waveguide in terms of mode summation for both polarizations. An example is shown in Fig. 2. Here, longitudinal variation of the field inside a 1m-wide plate at $x=0.7$ m is pictured. The line source is at $x'=0.3$ m. The number of propagating modes for the sets of parameters listed in the figure is 15. The two curves belong to the summation of the first 15 and 100 modes. As observed, at a distance beyond $z=0.5$ m (i.e., after 3-4 λ distance) only propagating modes contribute. Figure 3 displays field vs. x at two

different distances ($z=2\lambda$ and $z=20\lambda$). As observed, the contribution of only propagating modes at $z=2\lambda$ is not enough to build the correct field distribution.

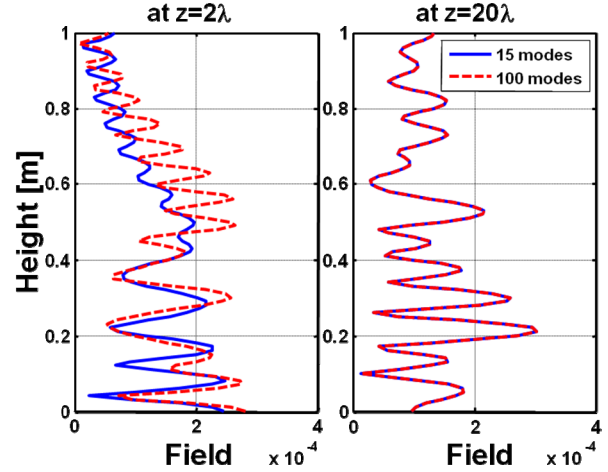


Fig. 3. Field vs. x (TM_z case): (Solid) only 15 propagating modes, (Dashed) The first 100 modes ($a=1$ m, $z'=0$, $x'=0.3$ m, $k_0 a=50$).

The line source is a theoretical antenna. In practice, a directive antenna is used in many applications. This antenna can be tilted upwards or downwards. A directive antenna with tilt-capability is usually modeled by injecting a vertical field distribution (e.g., a complex Gaussian function) in analytical and numerical simulations. It is therefore a challenge to compare models using line source excitations models with directive antennas; even data normalization may not be a solution in many cases. One solution in modeling a tilted (Gaussian) beam excitation is to use a line source at a specific horizontal position and then determine the ray excitation coefficients according to their departure angles.

The tilted Gaussian source $f(x, z')$ inside a parallel plate waveguide at $z=z'$ may be represented in terms of modal summation as:

$$f(x, z') = \sum_{m=m_0}^M c_m(z') v_m \Psi(k_{xm} x), \quad (7)$$

where M is the highest mode that should be included for the specified excitation (and depends on the specified accuracy), v_m is the normalization constant calculated from

$$v_m = \left(\int_{x=0}^a \Psi^2(k_{xm}x) dx \right)^{-1/2}, \quad (8)$$

and $c_m(z')$ is the modal excitation coefficient, numerically derived from transverse orthonormality condition:

$$c_m(z') = v_m \int_0^a f(x, z') \Psi(k_{xm}x) dx. \quad (9)$$

The initial field profile $f(x, 0)$ at $z' = 0$ is generated from a tilted Gaussian pattern

$$f(x, 0) = \exp \left[-jk_0 x \sin \theta_{elv} - \frac{(x - x')^2}{w^2} \right], \quad (10)$$

where $w = \sqrt{2 \ln 2} / (k_0 \sin(\theta_{bw} / 2))$. The tilted antenna pattern is specified by its transverse position (x'), beamwidth (θ_{bw}) and tilt (elevation) angle (θ_{elv}). Note that, Ψ again shows either Sine or Cosine function starting from either $m_0=1$ or $m_0=0$ for the TE_z and TM_z cases, respectively. The number of modes would be finite for numerical computations. It is common to choose a vertically extending Gaussian function with arbitrary location having vertical elevation angle in the range of $\pm 90^\circ$ (plus for upwards, minus for downwards). Note that the modal excitation coefficient c_m is real for a real source function without any tilt, and becomes complex if the source is tilted.

It should be noted that, reference data can best be generated from analytical exact solution if numerically computed accurately. The mode summation solution is exact but necessitates infinite number of terms with complex excitation coefficients for tilted directive antennas.

Figure 4 illustrates reliability of the reference data for a tilted Gaussian antenna. Here, field vs. x at two different z points for the same set of parameters, but for a directive antenna tilted 30° downwards with 45° beamwidth. The solid line belongs to data generated with the mode summation model. The dashed line belongs to the well-known Split-Step Parabolic Equation (SSPE) model [9]. A perfect agreement indicates the reliability of the reference data under both line source and directive antenna excitations.

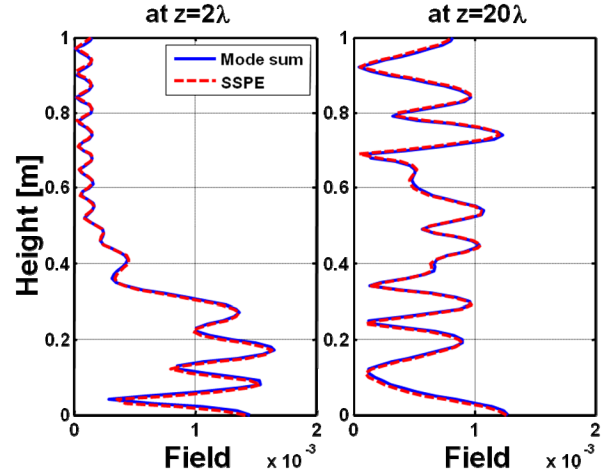


Fig. 4. Field vs. x (TM_z case): (Solid) Mode sum with 49 modes, (Dashed) SSPE ($a = 1$ m, $z' = 0$, $x' = 0.3$ m, $k_0 a = 50$, $dz = dx = 0.01$ m, $\theta_{bw} = 45^\circ$, $\theta_{elv} = -10^\circ$).

III. PARALLEL PLATE WAVEGUIDE AND METHOD OF MOMENT MODELING

Method of Moments (MoM) technique can be used to find propagation of horizontally (TE_z case) and vertically (TM_z case) polarized waves by using the Electric Field Integral Equation (EFIE) and the Magnetic Field Integral Equation (MFIE), respectively. Open region propagation over irregular ground and/or rough surface has been successfully modeled with MoM (see, for example, [5-7] among a huge number of reference list which cannot be included here). In the classical MoM, the integral equation is converted to the corresponding matrix equation via the discretization of the ground/surface. Then, an $N \times N$ system of equations $[V] = [Z][I]$ is constructed and is solved numerically. Here, $[I]$ contains the unknown segment currents, $[V]$ contains segment voltages excited by the source, $[Z]$ is the $N \times N$ impedance matrix of the ground/surface. Solution of this system yields the unknown segment currents. Superposition of the contributions of the segment currents via the Green's function of the problem yields the ground-scattered field. Finally, the total field is obtained by adding the incident field [6].

The classical MoM approach can be enhanced to model propagation inside waveguiding

structures. This is achieved by using the free-space Green's functions with a multi-iterative approach to build in the presence of the multiple reflections due to the conducting walls. Figure 1 shows MoM discretization and related parameters. Ray 1, shown as a sample, induces segment currents because of the external source. Ray 2 contributes to the field because of the induced segment currents. Ray 3 represents higher order effects on bottom segments caused by top segment currents. Necessary formulae for both polarizations are as summarized in [1,2,7]:

TE_z case

$$V_m = -E_y^{inc}(\boldsymbol{\rho}_m) = -E_0 \frac{e^{-jk_0 d_m}}{\sqrt{k_0 d_m}}, \quad (11a)$$

$$d_m = \sqrt{[x(\boldsymbol{\rho}_m) - x']^2 + [z(\boldsymbol{\rho}_m) - z']^2}, \quad (11b)$$

$$Z_{nm} \cong \begin{cases} -\frac{k_0 \eta_0 \Delta z}{4} H_0^{(2)}(k_0 |\boldsymbol{\rho}_n - \boldsymbol{\rho}_m|), m \neq n \\ -\frac{k_0 \eta_0 \Delta z}{4} \left[1 - j \frac{2}{\pi} \log \left(\frac{\gamma k_0 \Delta z}{4e} \right) \right], m = n \end{cases}, \quad (11c)$$

$$E_y^{sc}(\boldsymbol{\rho}_n) \cong -\frac{k_0 Z_0 \Delta z}{4} \sum_{m=1}^N I_m H_0^{(2)}(k_0 |\boldsymbol{\rho}_n - \boldsymbol{\rho}_m|), \quad (11d)$$

$$E_y^{tot} = E_y^{sc} + E_y^{inc}, \quad (11e)$$

TM_z case

$$V_m = -H_y^{inc}(\boldsymbol{\rho}_m) = -\frac{E_0}{\eta_0} \frac{e^{-jk_0 d_m}}{\sqrt{k_0 d_m}}, \quad (12a)$$

$$d_m = \sqrt{[x(\boldsymbol{\rho}_m) - x']^2 + [z(\boldsymbol{\rho}_m) - z']^2}, \quad (12b)$$

$$Z_{nm} \cong \begin{cases} j \frac{k_0 \Delta z}{4} H_1^{(2)}(k_0 |\boldsymbol{\rho}_n - \boldsymbol{\rho}_m|) (\hat{\mathbf{n}}_m \cdot \hat{\boldsymbol{\rho}}_{nm}), m \neq n \\ 0.5, m = n \end{cases}, \quad (12c)$$

$$H_y^{sc}(\boldsymbol{\rho}_n) \cong \frac{jk_0 \Delta z}{4} \sum_{m=1}^N I_m H_1^{(2)}(k_0 |\boldsymbol{\rho}_n - \boldsymbol{\rho}_m|) (\hat{\mathbf{n}}_m \cdot \hat{\boldsymbol{\rho}}_{nm}), \quad (12d)$$

$$H_y^{tot} = H_y^{sc} + H_y^{inc}, \quad (12e)$$

where Δz is the segment length, $\eta_0 \approx 120\pi$ is the intrinsic impedance of free space, $H_0^{(2)}$ and $H_1^{(2)}$ are the second kind Hankel functions with order zero and one, respectively, $\gamma \approx 1.781$ is the exponential of the Euler constant, $\hat{\mathbf{n}}_m$ denotes the unit normal vector of the plate at $\boldsymbol{\rho}_m$, and $\hat{\boldsymbol{\rho}}_{nm}$ is

the unit vector in the direction from source $\boldsymbol{\rho}_m$ to the receiving element $\boldsymbol{\rho}_n$.

The Mi-MoM procedure may be outlined as follows:

- First, discretize top and bottom boundaries. Use N segments for the lower and N segments for the upper boundaries. Label all segments from 1 to N in a way that Segment 1 and Segment $N+1$ have the same horizontal (i.e., z) coordinate (i.e., parallel to each other).
- Calculate segment currents $[I]$ from $[I] = [Z]^{-1} [V]$ and scattered/total fields using either E_y^{inc} in (11a) or H_y^{inc} in (12a) for TE_z and TM_z polarizations, respectively.
- For a given source point, calculate distances to all segments and segment voltages, using either E_y^{inc} in (11b) or H_y^{inc} in (12b) for TE_z and TM_z polarizations, respectively. This will yield $[V]$.
- Calculate the impedance matrix Z_{nm} from either (11c) or (12c) for TE_z and TM_z polarizations, respectively.
- The segment currents induced by the external source on the top plate excite field on segments on the bottom plate and a vice versa. For the first segment on the bottom plate, calculate distances to all segments on the top plate and segment voltages, using either E_y^{inc} in (11a) or H_y^{inc} in (12a) for TE_z and TM_z polarizations, respectively. Repeat this for all segments on the bottom plate and find out the voltages on the top plate caused by the segments on the bottom plate.
- Do the same for the segments on the top plate and find out the voltages on the bottom plate caused by the segments on the top plate. This will yield second round $[V]$.
- Use the same impedance matrix Z_{nm} and calculate second round segment currents $[I]$ from $[I] = [Z]^{-1} [V]$ and scattered/total fields using either E_y^{sc} in (11d/11e) or H_y^{sc} in (12d/12e) for TE_z and TM_z cases, respectively.

- Repeat the procedure and find out third round segment currents and scattered/total fields caused by these current.
- Repeat the whole procedure until a desired accuracy is reached.

An alternative way is to find out first round segment currents and then use the Image Method (IM). First, all segment currents of upper and lower plates are obtained. Then, boundaries are removed and image segments are added with respect to the upper and lower plates. Finally, field contributions from the currents of segments and image-segments are superposed at the receiver.

Two examples for the Mi-MoM procedure are given in Figs. 5 and 6. Figure 5 shows propagation factor (PF) (calculated field divided by its free-space value in dB) vs. z at a fixed x inside the parallel plate waveguide calculated with mode summation and Mi-MoM methods. As shown, very good agreement is obtained. As expected, Mi-MoM suffers from end-point effects, since segments before the first one and after the last one are neglected [6]. In order to overcome insufficiency of the MoM end-point effects one needs to extend the horizontally at least one or two wavelengths at both ends.

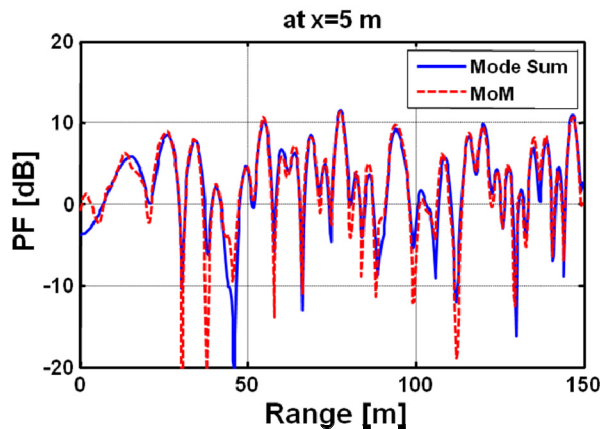


Fig. 5. Propagation factor vs. z (TM_z case): (Solid) Mode sum, (Dashed) Mi-MoM ($a = 100$ m, $z' = 0$, $x' = 50$ m, $x = 5$ m, $k_0 a = 209.5$).

Figure 6 shows field vs. x at two different z points, again calculated with mode summation and Mi-MoM methods. As observed, the agreement is very good. Note that, the agreement in Fig. 5 is better than the agreement in Fig. 6; this is merely

because of the frequency used in these examples ($k_0 a = 209.5$ in Fig. 5, but $k_0 a = 50$ in Fig. 6). The accuracy of Mi-MoM solution increases with frequency (i.e., with $k_0 a$).

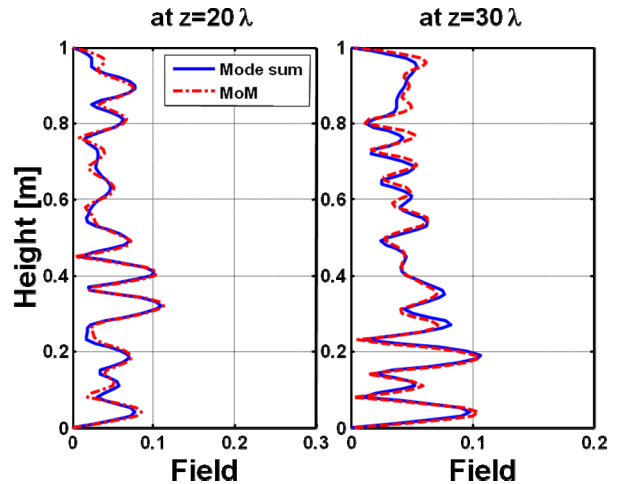


Fig. 6. Field vs. x (TE_z case): (Solid) Mode sum, (Dashed) Mi-MoM, $a = 1$ m, $z' = 0$, $x' = 0.4$ m, $k_0 a = 50$.

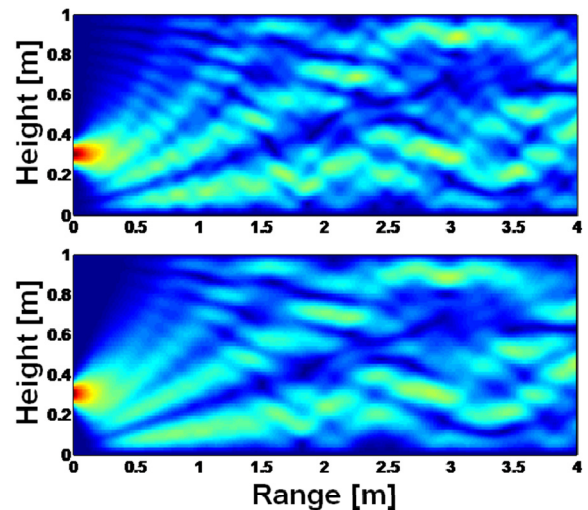


Fig. 7. The field map (TE_z case): (Top) Mode sum with 42 modes, (Bottom) Mi-MoM with 40 iterations, $a = 1$ m, $z' = 0$, $x' = 0.3$ m ($k_0 a = 50$, $dz = dx = 0.01$ m, $\theta_{bw} = 45^\circ$, no tilt).

Figures 7-9 belong to comparisons for directive antennas. As observed, the agreement between Mi-MoM results and the reference data is impressive even for these highly resonating/oscillatory variations.

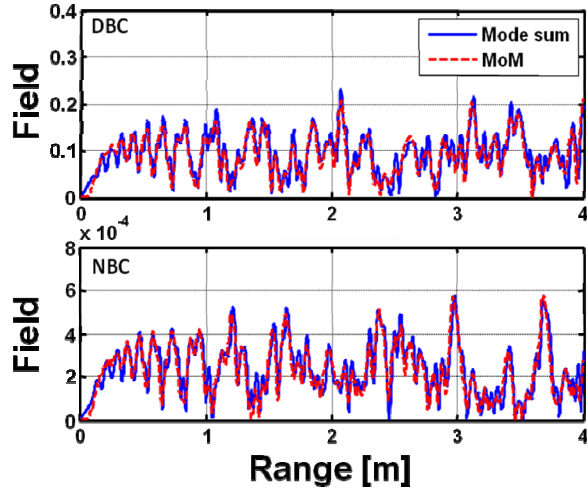


Fig. 8. Field vs. z at $x = 0.2$ m: (Top) TE_z case, (Bottom) TM_z case, (Solid) Mode sum with 282 modes, (Dashed) Mi-MoM with 50 iterations ($a = 1$ m, $z' = 0$, $x' = 0.4$ m, $k_0 a = 200$, $dz = dx = 0.0025$ m, $\theta_{bw} = 80^\circ$, no tilt).

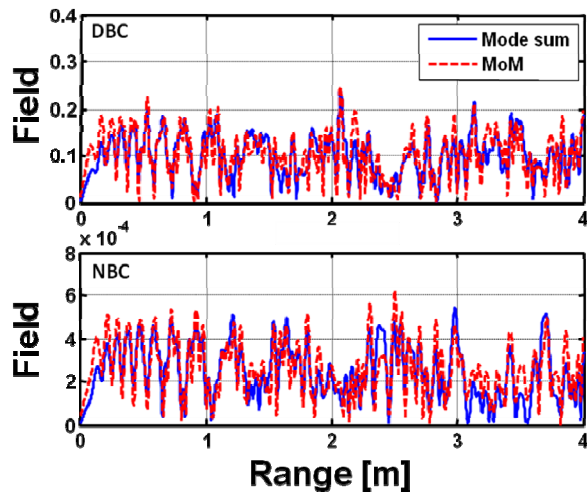


Fig. 9. Field vs. z at $x = 0.2$ m: (Top) TE_z case, (Bottom) TM_z case, (Solid) Mode sum with 298 modes, (Dashed) Mi-MoM with 50 iterations ($a = 1$ m, $z' = 0$, $x' = 0.4$ m, $k_0 a = 200$, $dz = dx = 0.0025$ m, $\theta_{bw} = 45^\circ$, $\theta_{elv} = -20^\circ$).

The final example belongs to a more realistic case. Figure 10 presents Mi-MoM vs. SSPE comparisons inside a PEC parallel plate waveguide with some irregularities on the bottom plate. Figure 10a presents the structure. Here, two Gaussian-shaped hills are shown on the bottom plate. Figure 10b shows 3D field map inside the

plate. Figure 10c belongs to the z variations of the field at $x = 0.4$ m for the TE_z polarization computed with Mi-MoM and SSPE methods.

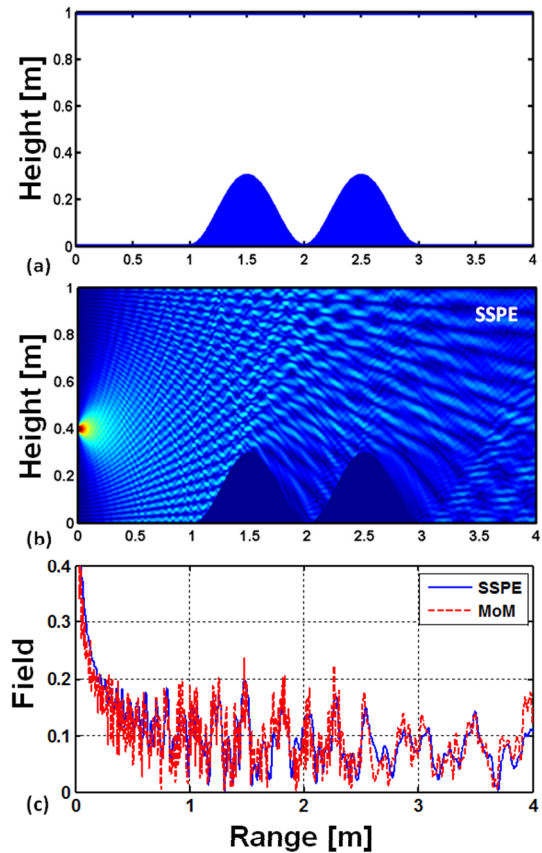


Fig. 10. (a) PEC waveguide with irregular bottom plate, (b) Field map produced with the SSPE, (c) Field vs. z at $x = 0.4$ m, both for TE_z case, (Solid) SSPE, (Dashed) Mi-MoM with 50 iterations ($a = 1$ m, $z' = 0$, $x' = 0.4$ m, $k_0 a = 200$, $\theta_{bw} = 80^\circ$, no tilt, $dz = dx = 0.0025$ m).

VI. CONCLUSIONS

A novel Multi-Iteration Method of Moment (Mi-MoM) procedure is introduced to model the propagation inside resonating structures. A two-dimensional (2D) parallel plate, non-penetrable waveguide is chosen as the test structure.

Mi-MoM results are tested against reference data generated from analytical exact mode summation method and are calibrated. Both the line source excitation and directive antennas are used during these tests. The Mi-MoM approach may increase applicability and efficiency of the MoM which has widely been used in modeling

antenna (radiation), propagation, and scattering problems for several decades.

Note that, $\lambda/10$ segmentation is enough for many applications, but up to $\lambda/100$ discretization will be necessary for high-accuracy computations. Finally, direct solution of the MoM matrix system can be achieved up to 8000-10000 segments with a student PC. Beyond this, acceleration techniques are mandatory [5-7].

REFERENCES

- [1] R. F. Harrington, *Field Computation by Moment Method*, IEEE Press, New York, 1993.
- [2] L. L. Tsai and C. E. Smith, "Moment Methods in Electromagnetics for Undergraduates," *IEEE Trans. Edu.*, vol. E, no. 31, pp. 14-22, 1978.
- [3] J. Moore and R. Pizer, *Moment Methods in Electromagnetics: Techniques and Applications*, Research Studies Press, New York, 1984.
- [4] M. N. O. Sadiku, *Numerical Techniques in Electromagnetics with MATLAB*, CRC Press, 2009.
- [5] H. T. Chou and J. T. Johnson, "Formulation of Forward-backward Method using Novel Spectral Acceleration for the Modeling of Scattering from Impedance Rough Surface," *IEEE Trans. Geo. and Remote Sensing*, vol. 38, pp. 605-607, 2000.
- [6] C. A. Tunc, A. Altintas, and V. B. Erturk, "Examination of Existent Propagation Models Over Large Inhomogeneous Terrain Profiles Using Fast Integral Equation Solution," *IEEE Trans. Antennas and Propag.*, vol. 53, pp. 3080-3083, Sep. 2005.
- [7] F. Akleman and L. Sevgi, "A Novel MoM- and SSPE-based Groundwave-propagation Field-Strength Prediction Simulator," *IEEE Antennas and Propag. Mag.*, vol. 49, pp. 69-82, 2007.
- [8] M. Levy, *Parabolic Equation Methods for Electromagnetic Wave Propagation*, IEE Institution for Electrical Engineers, 1993.
- [9] G. Apaydin and L. Sevgi, "Two-way Propagation Modeling in Waveguides with Three-dimensional Finite-element and Split-step Fourier-based PE Approaches," *IEEE Antennas and Wireless Propagation Letters*, vol. 10, pp. 975-978, 2011.
- [10] R. Ding, L. Tsang, and H. Braunisch, "Wave Propagation in a Randomly Rough Parallel-plate Waveguide," *IEEE Trans. on MTT*, vol. 57, no. 5, pp. 1216-1223, May. 2009.
- [11] L. B. Felsen and A. H. Kamel, "Hybrid Ray-mode Formulation of Parallel Plate Waveguide Green's Functions," *IEEE Trans. Antennas Propag.*, vol. 29, no. 4, pp. 637-649, Jul. 1981.
- [12] L. B. Felsen, F. Akleman, and L. Sevgi, "Wave Propagation inside a Two-dimensional Perfectly Conducting Parallel Plate Waveguide: Hybrid Ray-

mode Techniques and their Visualizations," *IEEE Antennas and Propag. Mag.*, vol. 46, no. 6, pp. 69-89, Dec. 2004.

- [13] L. Sevgi, "Guided Waves and Transverse Fields: Transverse to What?," *IEEE Antennas and Propag. Mag.*, vol. 50, no. 6, pp. 221-225, Dec. 2008.



Gökhan Apaydin received the B.S., M.S., and Ph.D. degrees in electrical and electronics engineering from Bogazici University, Istanbul, Turkey, in 2001, 2003, and 2007 respectively. From 2001 to 2005, he was a Teaching and Research Assistant by Bogazici

University. From 2005 to 2010, he was a Project and Research Engineer with the Applied Research and Development, University of Technology Zurich, Zurich, Switzerland. Since 2010, he has been with Zirve University, Gaziantep, Turkey. He has been working on several research projects on electromagnetic propagation, the development of a finite-element method for electromagnetic computation, filter design, and related areas. He has (co)authored 19 journals and 30 conference papers.



Levent Sevgi received the Ph.D. degree from Istanbul Technical University, Istanbul, Turkey, and Polytechnic Institute of New York University, Brooklyn, in 1990. Prof. Leo Felsen was his advisor. He was with Istanbul Technical University from 1991 to 1998; TUBITAK-MRC, Information Technologies Research Institute, Gebze/Kocaeli, Turkey, from 1999 to 2000; Weber Research Institute/Polytechnic University of New York, from 1988 to 1990; Scientific Research Group of Raytheon Systems, Canada, from 1998 to 1999; and the Center for Defense Studies, ITUVSAM, from 1993 to 1998 and from 2000 to 2002. Since 2001, he has been with Dogus University, Istanbul. He has been involved with complex electromagnetic (EM) problems and systems for more than 20 years.

Prof. Sevgi is an IEEE Fellow, the Writer/Editor of the "Testing ourselves" Column in the IEEE Antennas and Propagation Magazine and a member of the IEEE AP-S Education Committee.

Comparison of Dynamic Differential Evolution and Asynchronous Particle Swarm Optimization for Inverse Scattering of a Two-Dimensional Perfectly Conducting Cylinder

Ching-Lieh Li¹, Chung-Hsin Huang², Chien-Ching Chiu¹, and Chi-Hsien Sun³

¹ Electrical Engineering Department, Tamkang University,
Tamsui District, New Taipei City, Taiwan, R.O.C.

² Department of Computer and Communication Engineering, Taipei College of Maritime Technology,
Tamsui District, New Taipei City, Taiwan, R.O.C.

³ Department of Electronic Engineering, National Taiwan University of Science and Technology,
Taipei, Taiwan, R.O.C.

Abstract — The application of optimization techniques for shape reconstruction of a perfectly conducting two-dimensional cylinder buried in a slab medium is reported in this paper, for which comparative study of four population-based optimization algorithms are conducted. The method of finite difference time domain (FDTD) is employed for the analysis of the forward scattering part, while the inverse scattering problem is transformed into an optimization one. Four algorithms including particle swarm optimization (PSO), asynchronous particle swarm optimization (APSO), differential evolution (DE) and dynamic differential evolution (DDE) are applied to reconstruct the location and shape of a 2-D perfectly conducting cylinder. The performance of these optimization techniques is tested through the use of simulated fields to mimic the experimental measurements contaminated with additive white Gaussian noise. The reconstructed results show that DDE and APSO algorithms outperform the algorithms DE and PSO in terms of convergence speed. And DDE is concluded as the best algorithm in this study.

Index Terms - Inverse Scattering, Time Domain, FDTD, Sub-Grid Finite Difference Time Domain, Dynamic Differential Evolution, Asynchronous Particle Swarm Optimization, Slab Medium, Cubic Spline.

I. INTRODUCTION

The detection and reconstruction of certain buried and inaccessible scatterers by inverting microwave electromagnetic measurements is a research field of considerable interests because of its numerous applications in geophysical prospecting, civil engineering, and nondestructive testing. Numerical inverse scattering studies found in the literature are based on either frequency or time domain approaches [1]-[10]. However, it is well known that one major difficulty in inverse scattering problems is due to its ill-posedness in nature [11].

Another issue with inverse scattering problem is related to the nonlinearity because the inverting procedure involves the product of two unknowns: the electrical property of the object, and the electric field within the object. Especially, in the inverse problem involved with a dielectric slab medium there exists the interaction between the interfaces of three layers and the object, which leads to the complicated Green's function for this three-layer structure. Owing to the difficulties in computing the Green's function by numerical methods, the problems of inverse scattering involved with a dielectric slab were treated less intensively. In general, the nonlinearity of the problem is coped with by applying iterative optimization techniques [12]-[13].

The algorithms based on stochastic strategies offer advantages, over traditional deterministic

algorithms, which include strong search ability simplicity, robustness, and insensitivity to ill-posedness. In contrast to traditional deterministic methods, evolutionary searching schemes provide a more robust and efficient approach for solving inverse scattering problems. PSO and DE both work with a population of solutions; PSO is very efficient at exploring the entire search space, while DE is able to accomplish the same goal as genetic algorithm (GA) in a new and faster way. Thus several improved versions such APSO and DDE have gained considerable attention [14]-[19].

Time domain inverse scattering problems appear quite a lot in the area of remote sensing. Various time domain approaches had been proposed such as the layer-stripping approach [20], Born iterative method (BIM) [21], distorted Born iterative method (DBIM) [22] and different optimization approaches [23], [24]. The inverse scattering problems are usually treated by the traditional deterministic methods which are based on functional minimization via some gradient-type scheme. Furthermore, for gradient-type methods, it is well known that the convergence of the iteration depends highly on the initial guess. If a good initial guess is given, the speed of the convergence can be very fast. On the other hand, if the initial guess is far away from the exact one, the searching tends to get fail [25]. In general, they tend to get trapped in local minima when the initial trial solution is far away from the exact one. Thus, some population-based stochastic methods, such as GA [26], [27] PSO [28]-[31], DDE [32]-[34] are proposed to search the global extrema of the inverse problems to overcome the drawback of the deterministic methods.

Concerning the shape reconstruction of conducting scatterers, the PSO has been investigated whereas the steady-state genetic algorithm (SSGA) has been utilized in the reconstruction of metallic scatterers [27]. In this case, the reported results indicate that PSO is a reliable tool for inverse scattering application. Moreover, it has been shown that both DE and PSO outperform real-coded GA in terms of convergence speed [35], [36]. In recent decades, some papers have compared different algorithms for inverse scattering problems [14], [31], [37], [38]. However, to our knowledge, a comparative study about the performances of DDE and APSO

mainly when applied to inverse scattering problems has not yet been investigated.

In this paper, the shape reconstruction is based on the application of DDE and APSO mainly. The forward problem is solved by the FDTD method, for which the sub-grid technique [39] is implemented to closely describe the fine structure of the cylinder. The inverse problem is formulated into an optimization one, and then the global searching schemes DE, DDE, PSO and APSO are used to search the parameter space. Cubic spline interpolation technique [40] is employed to reduce the number of parameters needed to closely describe a cylinder of arbitrary shape as compared to the Fourier series expansion.

The cost function of the four algorithms is to minimize the discrepancy between the simulated field (mimicking the measured one) and the estimated scattered field data with respect to the parameters of the cubic-spline expansion. Numerical results show that DDE outperforms APSO slightly in terms of shape reconstruction accuracy, giving a lower reconstruction error for the same number of iterations. As a whole, DDE and APSO algorithms outperform the algorithms DE and PSO in terms of convergence speed.

In section II, the details of the sub-grid FDTD method for the forward scattering are presented. In section III and IV, inverse problem and the numerical results of the proposed study are given, respectively. Finally, in section V some conclusions are drawn.

II. FORWARD PROBLEM

Let us consider a two-dimensional three-layer structure with the electromagnetic property (ϵ_1, μ_1) for region 1, (ϵ_2, μ_2) for region 2 and (ϵ_3, μ_3) for region 3, as shown in Fig. 1. A perfectly conducting cylinder to be de-embedded is buried in the second layer, and is parallel to z axis. The perfectly conducting cylinder is illuminated by a line source with Gaussian pulse shape placed at two different positions sequentially denoted by Tx in the first layer, and then the scattered E fields are recorded simultaneously at those points denoted by Rx in the same layer. The cross-section shape of the object is starlike and can be represented in polar coordinates with respect to the origin (X_0, Y_0) of the local coordinate in x - y plane as

shown in Fig. 2. The computational domain is discretized by using Yee cells [41]. It should be mentioned that the computational domain is surrounded by some optimized absorber of the perfect matching layer (PML) [42] to reduce the reflection from the surrounding PML environment.

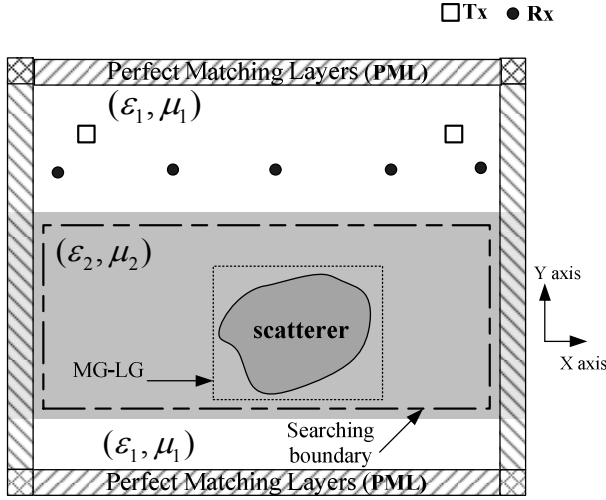


Fig. 1. Geometrical configuration of the problem.

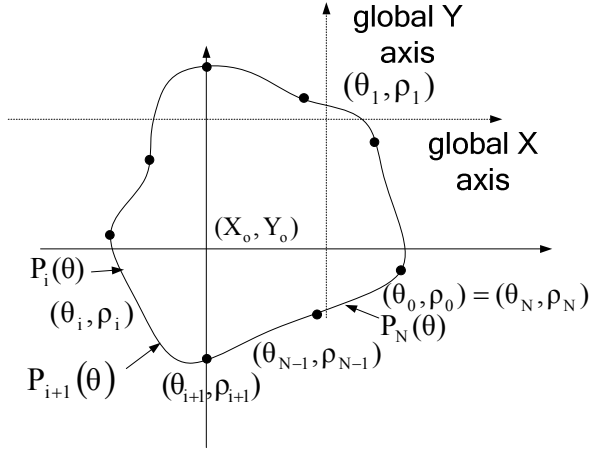


Fig. 2. A cylinder of arbitrary shape is described in terms of a closed cubic spline. The cubic spline consists of the polynomials of degree 3. (X_0, Y_0) is the center position in the x-y plane. The $\rho_1, \rho_2, \dots, \rho_N$ are radius parameters to describe cylinder.

The direct scattering problem is to calculate the scattered electric fields while the shape and location of the scatterer are given. The shape function $F(\theta)$ of the scatterer is described by the trigonometric series in the direct scattering problem

$$F(\theta) = \sum_{n=0}^{N/2} B_n \cos(n\theta) + \sum_{n=1}^{N/2} C_n \sin(n\theta) \quad (1)$$

where B_n and C_n are real coefficients to expand the shape function.

In order to closely describe the shape of the cylinder for both the forward and inverse scattering procedure, the sub-grid technique is implemented in the FDTD code; the details are presented next.

The FDTD method is a direct implementation of the time-dependent Maxwell equations, written in finite-difference form for implementation on a computer.

$$\nabla \times \bar{E}(r, t) = -\frac{\partial \bar{B}(r, t)}{\partial t} \quad (2)$$

$$\nabla \times \bar{H}(r, t) = \frac{\partial \bar{D}(r, t)}{\partial t} + \bar{J}(r, t) \quad (3)$$

The finite-difference procedure was first proposed by Yee [41], who positioned the E and H fields at half-step intervals around a unit cell. Moreover, the E and H fields are evaluated at alternate half time steps, effectively through the use of centered difference expressions for both the space and time derivatives. The above equations can be easily implemented on a computer as follows:

$$E_z^{n+1} \Big|_{i+\frac{1}{2}, j+\frac{1}{2}} = C_a \Big|_{i+\frac{1}{2}, j+\frac{1}{2}} E_z^n \Big|_{i+\frac{1}{2}, j+\frac{1}{2}} + C_b \Big|_{i+\frac{1}{2}, j+\frac{1}{2}} \left[\frac{H_y^{n+\frac{1}{2}} \Big|_{i+\frac{1}{2}, j+\frac{1}{2}} - H_y^{n+\frac{1}{2}} \Big|_{i+\frac{1}{2}, j-\frac{1}{2}}}{\Delta x} - \frac{H_x^{n+\frac{1}{2}} \Big|_{i+\frac{1}{2}, j+\frac{1}{2}} - H_x^{n+\frac{1}{2}} \Big|_{i-\frac{1}{2}, j+\frac{1}{2}}}{\Delta y} \right] \quad (4)$$

$$H_x^{n+\frac{1}{2}} \Big|_{i+\frac{1}{2}, j} = H_x^{n-\frac{1}{2}} \Big|_{i+\frac{1}{2}, j} - D \Big|_{i+\frac{1}{2}, j} \left[\frac{E_z^n \Big|_{i+\frac{1}{2}, j+\frac{1}{2}} - E_z^n \Big|_{i+\frac{1}{2}, j-\frac{1}{2}}}{\Delta y} \right] \quad (5)$$

$$H_y^{n+\frac{1}{2}} \Big|_{i, j+\frac{1}{2}} = H_y^{n-\frac{1}{2}} \Big|_{i, j+\frac{1}{2}} - D \Big|_{i, j+\frac{1}{2}} \left[\frac{E_z^n \Big|_{i+\frac{1}{2}, j+\frac{1}{2}} - E_z^n \Big|_{i-\frac{1}{2}, j+\frac{1}{2}}}{\Delta x} \right] \quad (6)$$

$$C_a = \frac{1 - \sigma \Delta t / 2\epsilon}{1 + \sigma \Delta t / 2\epsilon} \quad C_b = \frac{\Delta t / \epsilon}{1 + \sigma \Delta t / 2\epsilon} \quad D = \Delta t / \epsilon$$

Note that for nonmagnetic materials D is a constant.

In Fig. 3, E and H stand for the electric and magnetic fields on the major grids, respectively, while e and h denote the electric and magnetic fields on the local grids. If the scaling ratio is set at odd ratio, for example 1:3, the E and H fields

coincide with e and h fields in the fine region as shown in Fig. 3. Note that the e and h fields inside the fine region can be updated through the normal Yee-cell algorithm [41] except those at the main-grid-local-grid (MG-LG) boundary [43], such as h_1 , h_2 and h_3 in Fig. 3.

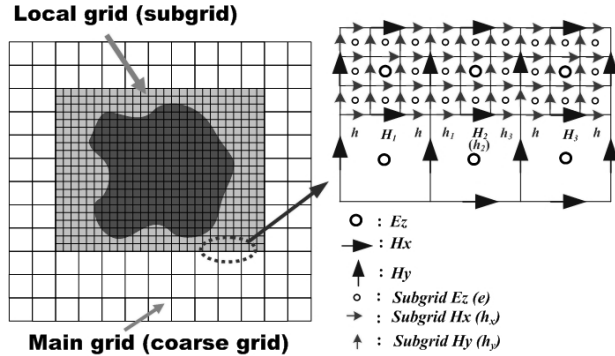


Fig. 3. Structure of the TM_z finite difference time domain method (FDTD) major grids and local grids for the scaling ratio (1:3), H fields are aligned with the main-grid-local-grid (MG-LG) boundary.

The h fields at the MG-LG interface can be linearly interpolated as follows :

$$h_1^{n+v} = H_1^{n+v} + \frac{2}{3}(H_2^{n+v} - H_1^{n+v})$$

$$h_2^{n+v} = H_2^{n+v}, \text{ for } v = \frac{1}{3}, \frac{2}{3} \text{ and } \frac{3}{3}. \quad (7)$$

$$h_3^{n+v} = H_2^{n+v} + \frac{1}{3}(H_3^{n+v} - H_2^{n+v})$$

Note that the H fields don't exist on the main grids actually for $v = \frac{1}{3}$ and $\frac{2}{3}$ and need extra parabolic interpolation calculation by

$$H^{n+v} = H^n + Av + \frac{Bv^2}{2} \quad (8)$$

$$\text{with } A = \frac{H^{n+1} - H^{n-1}}{2}$$

$$B = H^{n+1} - H^{n-1} - 2H^n$$

The corresponding flow chart for updating the EM fields in the fine region is shown in Fig. 4.

Note that at the time step $n + \frac{3}{6}$ the $E^{n+\frac{1}{2}}$ fields on the main grids should be updated by the coincided $e^{n+\frac{3}{6}}$ fields on the local grids. Similarly,

at the time step $n + \frac{6}{6}$ the H^{n+1} fields are updated by the coincided $h^{n+\frac{6}{6}}$ fields.

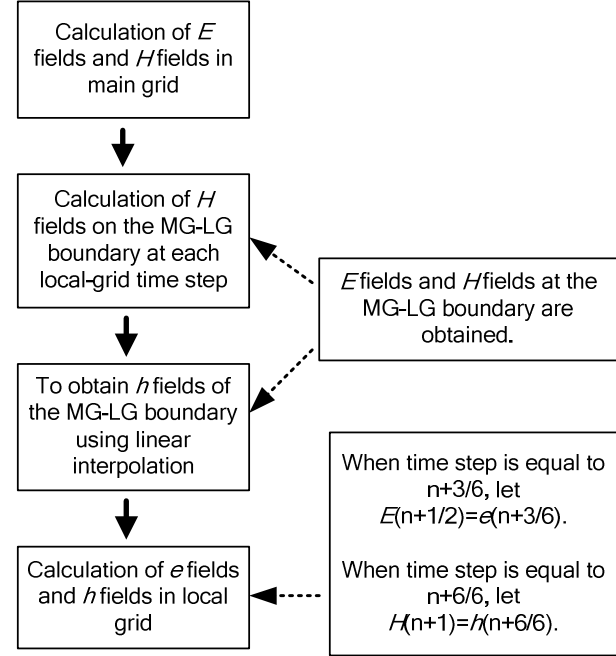


Fig. 4. The flowchart to update the (E,H) fields on the major grids and (e,h) fields on local grids.

For the time domain scattering and inverse scattering problems, the scatterer is assigned with the fine region such that the fine structure of the scatterer can be easily described. If higher resolution is needed, only the fine region needs to be rescaled using a higher ratio for sub-grid. This can avoid discretizing the whole problem space using the finest resolution such that the computational resources are utilized in a more efficient way, which is quite important for the computationally intensive inverse scattering problems. More details on the FDTD Sub-grid scheme can be found in [39].

III. INVERSE PROBLEM

For the inverse scattering problem, the shape and location of the metallic cylinder are reconstructed by the given scattered electric fields measured at the receivers, conceptually. The inverse problem is resolved by an optimization approach, for which the global searching DDE and APSO schemes, etc., are employed to minimize the following cost function (CF) :

$$CF = \frac{\sum_{n=1}^{N_i} \sum_{m=1}^M \sum_{q=0}^Q |E_z^{exp}(n, m, q\Delta t) - E_z^{cal}(n, m, q\Delta t)|}{\sum_{n=1}^{N_i} \sum_{m=1}^M \sum_{q=0}^Q |E_z^{exp}(n, m, q\Delta t)|} \quad (9)$$

where E_z^{exp} and E_z^{cal} are the mimically experimental electric fields and the calculated electric fields, respectively. The N_i and M are the total number of the transmitters and receivers, respectively. Q is the total time step number of the recorded electric fields. The details of the proposed DE, DDE, PSO and APSO are presented next.

A. Differential Evolution (DE) and Dynamic Differential Evolution (DDE)

DE and DDE algorithms start with an initial population of potential solutions that is composed by a group of randomly generated individuals which represent the center position and the geometrical radii of the cylinders. The initial population may be expressed by $\{x_j : j = 1, 2, \dots, Np\}$, where Np is the population size. Each individual in DE or DDE algorithms is a D -dimensional vector consisting of D parameters to be optimized. After initialization, DE and DDE algorithms perform the genetic evolution until the termination criterion is met. DE and DDE algorithms, like other evolutionary algorithms (EAs), also rely on the genetic operations (mutation, crossover and selection) to evolve generation by generation. The flowchart of the DDE algorithm is shown in Fig. 5. DE and DDE algorithms go through six procedures as follows:

1. Initialize a starting population: DE and DDE algorithms are initialized with a population that is composed by a group of randomly generated individuals. As mentioned above, individuals in DE and DDE algorithm represent a set of D -dimensional vectors in the parameter space for the problem, $\{x_j : j = 1, 2, \dots, Np\}$, where D is the number of parameters to be optimized and Np is the population size.
2. Evaluate the population using cost function: After initialization, DE and DDE

algorithms evaluate the cost function (9) for each individual in the population.

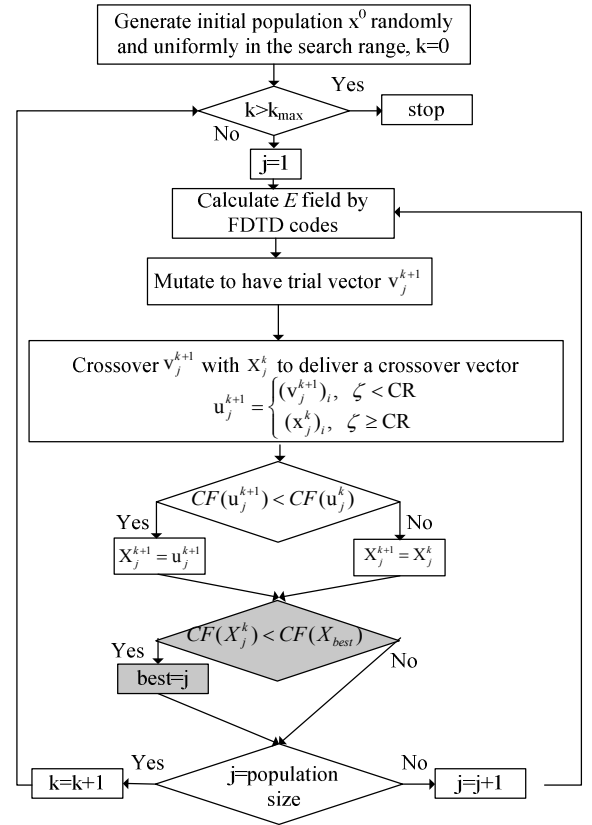


Fig. 5. Flowchart for the dynamic differential evolution. Pessimistic sub-area stands for dynamic update.

3. Perform mutation operation to generate trial vectors: The mutation operation of DDE algorithm is performed by arithmetical combination of individuals. A disturbing vector V_j^{k+1} is generated according to following equation:

$$(v_j^{k+1})_i = (x_j^k)_i + F \cdot [(x_{best}^k)_i - (x_j^k)_i] + \lambda \cdot [(x_m^k)_i - (x_n^k)_i] \quad (10)$$

$, j = 0 \sim N_p - 1, m, n \in [0, N_p - 1],$
 $m \neq n; i = 1 \sim D$

where λ and F are the scaling factors associated with the vector differences $(x_{best}^k - x_j^k)$ and $(x_m^k - x_n^k)$, respectively.

The disturbing vector v_j^{k+1} due to the mutation mechanism consists of parameter vector x_j^k , the best trial vector x_{best}^k and two randomly selected vectors x_m^k and

x_n^k . As comparison, the disturbing vector v_j^{k+1} is generated according to equation (11) for typical DE [12].

$$(v_j^{k+1})_i = (x_j^k)_i + F \cdot [(x_m^k)_i - (x_n^k)_i],$$

$$j = 0 \sim N_p - 1, m, n \in [0, N_p - 1], \quad (11)$$

$$m \neq n; i = 1 \sim D$$

where F are the scaling factors associated with the randomly selected vector difference $(x_m^k - x_n^k)$. One of the main differences between DDE and DE is that DDE includes the idea of approaching the “Best” during the course of optimization procedure.

4. Perform crossover operation with probability of crossover CR to deliver crossover vectors: The crossover operation in DE and DDE algorithms is performed to increase the diversity of the parameter vectors. This operation is similar to the crossover process in GAs. However, the crossover operation in DE and DDE algorithms just allows delivering the crossover vector u_j^{k+1} by mixing the components of the current vector x_j^k and the disturbing vector v_j^{k+1} . It can be expressed as:

$$(u_j^{k+1})_i = \begin{cases} (v_j^{k+1})_i, & \zeta < CR \\ (x_j^k)_i, & \zeta \geq CR \end{cases},$$

$$j = 0 \sim N_p - 1, i = 1 \sim D \quad (12)$$

where CR is the probability of crossover, $CR \in (0,1)$. ζ is the random number generated uniformly between 0 and 1.

5. Perform selection operation to produce offspring: Selection operation is conducted by comparing the parent vector x_j^k with the crossover vectors u_j^{k+1} . The vector with smaller cost function value is selected as a member of the next generation. Explicitly, the selection operation for the minimization problem is given by:

$$x_j^{k+1} = \begin{cases} u_j^{k+1} & , \text{ if } CF(u_j^{k+1}) < CF(x_j^k) \\ x_j^k & , \text{ otherwise} \end{cases}$$

$$, j = 0 \sim N_p - 1 \quad (13)$$

Another major difference between DDE and DE is that DDE algorithm is carried out in a dynamic way: each parent individual would be replaced by its offspring if the offspring has yielded a better cost function value than its parent. While in a typical DE, all the updating actions of the population are performed at the end of the generation, for which it is referred to as static updating mechanism.

6. Stop the process and obtain the best individual if the termination criterion is satisfied, otherwise go to step 2.

Having realized the ideas of approaching the “Best” and dynamic updating, DDE thus exhibits better searching capability than DE does regarding the convergence speed. Hence, DDE is able to reduce the numbers of cost function evaluation and reconstruct the microwave image efficiently.

B. The modified asynchronous Particle swarm optimization (APSO)

Particle swarm global optimization is a class of derivative-free, population-based and self-adaptive search optimization technique which was introduced by Kennedy and Eberhart [13]. Particles (potential solutions) are distributed throughout the searching space and their positions and velocities are modified based on social behavior. The social behaviors in PSO exhibit a population of particles moving toward the most promising region of the search space. Clerc [44] proposed the constriction factor to adjust the velocity of the particle for obtaining the better convergence; the algorithm was named as constriction factor method (CFM). PSO starts with an initial population of potential solutions that is randomly generated and composed of N_p individuals (also called particles), of which each represents the location and the geometrical radii of the cylinder in this study.

After the initialization step, each particle of population is associated with a randomized velocity and position. Thus, each particle has a position and velocity vector, and can move through the problem space. In each generation, every particle changes its velocity according to its

best position up to date with the latest evolution, called \mathcal{X}_{pbest} and the best particle in the swarm, called \mathcal{X}_{gbest} .

Assume there are N_p particles in the swarm that is in a search space of D dimensions, the position and velocity of the j -th particle is determined according to the following equations according to the constriction factor method:

$$\begin{aligned} (v_j^{k+1})_i = \chi \cdot \left(\begin{aligned} &(v_j^k)_i + c_1 \cdot \phi_1 \cdot ((x_{pbest,j}^k)_i - (x_j^k)_i) \\ &+ c_2 \cdot \phi_2 \cdot ((x_{gbest,j}^k)_i - (x_j^k)_i) \end{aligned} \right) \\ , j = 0 \sim N_p - 1, i = 1 \sim D \end{aligned} \quad (14)$$

$$\begin{aligned} x_j^{k+1} = x_j^k + v_j^{k+1}, j = 0 \sim N_p - 1, \\ i = 1 \sim D \end{aligned} \quad (15)$$

$$\text{where } \chi = \frac{2}{|2 - \varphi - \sqrt{\varphi^2 - 4\varphi}|}, \varphi = c_1 + c_2 \geq 4.$$

c_1 and c_2 are the learning coefficients used to control the impact of the local and global component in velocity equation (14). φ is the constriction factor. ϕ_1 and ϕ_2 are both random numbers between 0 and 1. $(v_j^k)_i$ and $(x_j^k)_i$ are the velocity and position of i -th dimension of the j -th particle at the k -th generation. It should be mentioned that the V_{max} method is also applied to control the particle's searching velocity and to confine the particle within the search space [45]. The value of V_{max} is set to be half of X_{max} , where X_{max} is the upper limit of the search space. Note that the V_{max} and X_{max} are maximum velocity and maximum distance, respectively. As an extreme case, if the maximum velocity V_{max} is set to X_{max} , the exploration in the inverse scattering problem space is not limited. Occasionally, the particles may move out of the search space, which could be remedied by applying the boundary condition to draw the foul particles back to the normal space.

The key distinction between PSO and APSO is on the updating mechanism, damping boundary condition and mutation scheme. In a typical synchronous PSO, the algorithm updates the velocities and positions of all particles using equations (14) and (15) till the end of each

generation. And then update the best positions \mathcal{X}_{pbest} and \mathcal{X}_{gbest} . Alternatively, the updating mechanism of the asynchronous PSO use the following rule: after the position movement of each particle the new best positions \mathcal{X}_{pbest} and \mathcal{X}_{gbest} will be updated and then used for next particle immediately if the cost function value for the new position is better than the best record up to date. In this way, the swarm reacts more quickly to speed up the convergence.

The ‘‘damping boundary condition’’ is proposed by Huang and Mohan [46] to ensure the particles move within the legal search space. In many practical optimization problems, the rough location of the global optimum is usually difficult to know in advance. It is therefore required to have a boundary condition that can offer a robust and consistent performance for the PSO technique regardless of the problem. When a particle tends to move outside the search space, the position of particle is re-located about the search boundary and its velocity is multiplied by a random number (between 0 and 1) and arranged in the reverse direction.

Mutation scheme is introduced in PSO and APSO algorithms to speed up the convergence when particles are all around the global optimum. The mutation scheme can also avoid premature convergences in the searching procedure and help \mathcal{X}_{gbest} escape from local optimal positions, thus the robustness of the PSO and APSO algorithms is assured.

The flowchart of the modified asynchronous PSO (APSO) is shown in Fig. 6. APSO goes through seven procedures as follows:

1. Initialize a starting population: randomly generate a swarm of particles.
2. Calculate the E fields by a home-made FDTD code.
3. Evaluate the population using cost function: the APSO algorithm evaluates the cost function (9) for each individual in the population.
4. Find \mathcal{X}_{pbest} and \mathcal{X}_{gbest} .
5. Mutation scheme: the PSO algorithm has been shown to converge rapidly during the initial stages of a global

search, but when around the global optimum, the search can become very slow. For the reason, mutation scheme is introduced into APSO. As shown in Fig. 6, there is an additional competition between the x_{gbest} and $x_{gbest_{mu}}$. The current x_{gbest} will be replaced by the $x_{gbest_{mu}}$ if the $x_{gbest_{mu}}$ is better than the current x_{gbest} . The $x_{gbest_{mu}}$ is generated by following way:

$$x_{gbest_{mu}} = \begin{cases} x_{gbest} - \phi_3 \cdot \left[c_3 - (c_3 - c_4) \cdot \frac{k}{k_{max}} \right] \cdot (X_{max} - X_{min}), & \text{if } \phi_{mu} < 0.5 \\ x_{gbest} + \phi_3 \cdot \left[c_3 - (c_3 - c_4) \cdot \frac{k}{k_{max}} \right] \cdot (X_{max} - X_{min}), & \text{if } \phi_{mu} \geq 0.5 \end{cases} \quad (16)$$

where c_3 and c_4 are the scaling parameter. ϕ_3 and ϕ_{mu} are both the random numbers between 0 and 1. k is the current iteration number. k_{max} is the maximum iteration number. X_{max} and X_{min} are the upper limit and lower limit of the search space, respectively.

6. Update the velocity and position.
7. Stop the process and obtain the best individual if the termination criterion is satisfied, otherwise, go to step 2.

It should be noted that since both APSO and DDE realize the ideas of approaching the ‘‘Best’’ and dynamic updating, they exhibit similar searching capability and convergence property.

B. Cubic spline interpolation technique

It should be noted that in the inverse problem, the shape function of the 2-D perfectly conducting cylinder is described by a cubic spline in this study instead of the trigonometric series (1) shown in the section of the forward problem. The cubic spline is more efficient in terms of the unknown number required to describe a cylinder of arbitrary cross

section. In addition, by using the cubic spline the coordinates of local origin inside the cylinder serve as the searching parameters and can move around the searching space, which is very hard to achieve, if not impossible, when the trigonometric series expansion is used in the inversion procedure. Thus by using the cubic spline expansion, the justification for the objective of the inverse scattering is maintained.

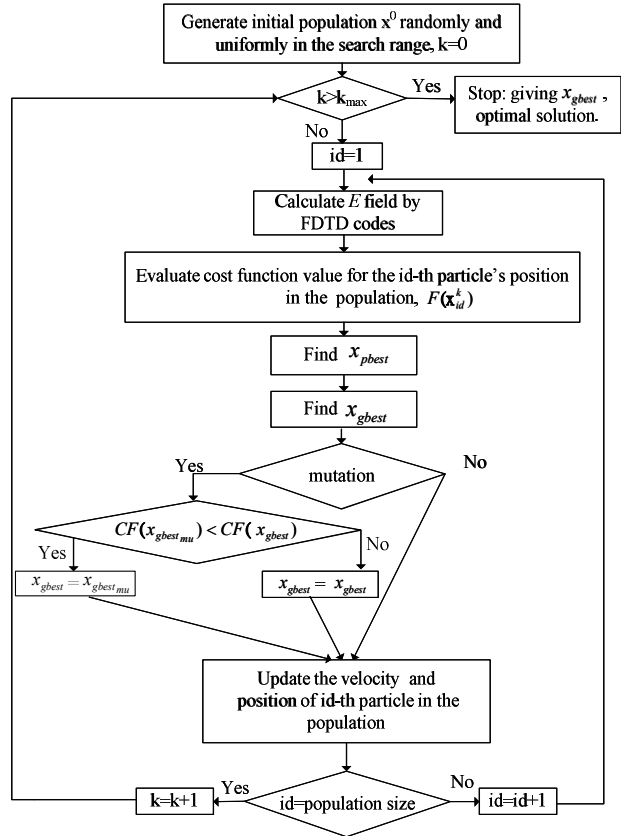


Fig. 6. Flowchart for the modified APSO.

As shown in Fig. 2, the cubic spline consists of the polynomials of degree 3 $P_i(\theta)$, $i = 1, 2, \dots, N$, which satisfy the following smooth conditions:

$$\begin{aligned} P_i(\theta_i) &= P_{i+1}(\theta_i) \equiv \rho_i \\ P_i'(\theta_i) &= P_{i+1}'(\theta_i) \\ i &= 1, 2, \dots, N \\ (17) \\ P_i''(\theta_i) &= P_{i+1}''(\theta_i) \end{aligned}$$

and

$$\begin{aligned}
P_1(\theta_0) &= P_N(\theta_N) \\
P_1'(\theta_0) &= P_N'(\theta_N) \equiv \rho'_N \\
P_1''(\theta_0) &= P_N''(\theta_N)
\end{aligned} \tag{18}$$

Through the interpolation of the cubic spline, an arbitrary smooth cylinder can be easily described through the radius parameters $\rho_1, \rho_2, \dots, \rho_N$ and the slope ρ'_N , of which the details are referred to [40]. By combining the PSO, APSO, DE or DDE algorithm with the cubic spline interpolation technique, together with the FDTD sub-grid method, we are able to reconstruct the microwave image efficiently.

It should be noted that the coordinates of local origin inside the cylinder plus the radii of the geometrical spline used to describe the shape of the cylinder will be determined by the PSO, APSO, DE and DDE algorithms.

IV. NUMERICAL RESULTS

As shown in Fig. 1, the problem space is divided in 68×68 grids with the grid size $\Delta x = \Delta y = 5.95$ mm. The metallic cylinder is buried in a lossless slab medium ($\sigma_1 = \sigma_2 = \sigma_3 = 0$). The transmitters and receivers are placed in free space above the homogeneous dielectric. The permittivities in regions 1, 2 and 3 are characterized by $\epsilon_1 = \epsilon_0$, $\epsilon_2 = 8\epsilon_0$ and $\epsilon_3 = \epsilon_0$, respectively, while the permeability μ_0 is used for each region; i.e., only non-magnetic media are concerned here.

The scatterer is illuminated by cylindrical waves with the electric field polarized along the z axis, while the time dependence of the field is a derivative Gaussian pulse. The waveform is plotted in Fig. 7. The cylindrical object is illuminated by a transmitter at two different positions ($N_T=2$), which are located at $(-143\text{mm}, 178.5\text{mm})$ and $(143\text{mm}, 178.5\text{mm})$, respectively. The scattered E fields for each illumination are collected at the five receivers ($M=5$), which are equally separated by 47.8mm along the line at distance 48mm from the interface between region 1 and region 2.

The time duration is set to $300 \Delta t$ ($q = 300$). In order to describe the shape of the cylinder more

accurately, the sub-grid FDTD technique is employed both in the forward scattering (1:9) and the inverse scattering (1:5) - but with different scaling ratios as indicated in the parentheses. The proposed inversion procedures are implemented through some home-made Fortran programs that runs on an Intel PC (3.4 GHz/ 2G memory /500 G). The typical CPU time needed for DDE and APSO examples are about 11 and 9.5 hours, respectively, in this study.

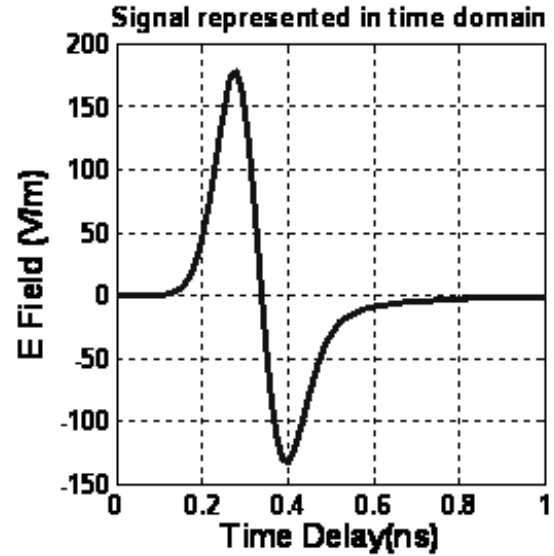


Fig. 7. Signal represented in time domain.

Three examples are investigated for the inverse scattering of the proposed structure by using the DDE and APSO, etc. There are eleven unknown parameters to retrieve, which include the center position (X_o, Y_o) , the radius ρ_i , $i = 1, 2, \dots, 8$ of the shape function and the slope ρ'_N . Relatively wide searching ranges are used for DDE and APSO, etc, to optimize the cost function given by (9). The parameters and the corresponding searching ranges are listed as follows:

$$\begin{aligned}
-47.6\text{mm} &\leq X_o \leq 47.6\text{mm} \\
-47.6\text{mm} &\leq Y_o \leq 47.6\text{mm} \quad , \quad 5.95\text{mm} \leq \rho_i \leq 71.4\text{mm} \quad , \\
i &= 1, 2, \dots, 8 \quad , \quad -1 \leq \rho'_N \leq 1 \quad .
\end{aligned}$$

The operational coefficients for the DDE algorithm are set as below: The crossover rate $CR=0.8$. The weighting factor $F = \lambda=0.8$ and the population size $Np=110$.

The relative coefficients of the modified APSO are set below. The learning coefficients c_1 and c_2 are set to 2.8 and 1.3, respectively. The scaling parameter, c_3 and c_4 , are set to 0.1 and 0.05, respectively. The mutation probability is 0.4 and the population size is set to 30. Here, the shape error DF is defined as

$$DF = \left\{ \frac{1}{N'} \sum_{i=1}^{N'} [F^{cal}(\theta_i) - F(\theta_i)]^2 / F^2(\theta_i) \right\}^{1/2} \quad (19)$$

where the N' is set to 720.

As mentioned above, application of sub-grid technique can result in large savings of computer time and memory for the FDTD method. Thus, in this study, sub-grid FDTD technique is implemented to efficiently describe the details of the dielectric cylinders shape. For the first example, the perfectly conducting cylinder with shape function $F(\theta) = 29.75$ (unit: mm) is tested. In Figs. 8 and 9, the standard FDTD with uniform grid of (1:1) case is compared with the sub-grid FDTD cases of different scaling ratios (1:3), (1:5) and (1:7) for the inverse scattering by DDE and APSO algorithms, respectively. The reconstructed details are listed in Table I for DDE and APSO algorithms, respectively. Obviously, the results obtained by using the standard FDTD with uniform grid (1:1) are not as good as those of the sub-grid FDTD cases. Moreover, the values of DF for DDE and APSO algorithms are very close.

Table 1: The errors of the reconstructed shape function for example 1 by using different subgridding ratios.

subgridding ratio	DF via DDE	DF via APSO
1:1	9.38%	8.92%
1:3	1.85%	4.50%
1:5	1.35%	1.68%
1:7	1.02%	1.52%

It also suggests that the scaling ratio (1:5) is suitable for the following examples to be studied. On the other hand, in order to achieve the same accuracy for the standard FDTD with uniform grid, the grid size of the whole space has to be reduced to smoothly describe the geometry of the perfectly conducting cylinder, however, the

computation time would be increased quite a lot, 3.85 times as compared to the subgrid FDTD scheme of (1:5) case. Moreover, the convergence curves of the cost function versus generation as the proposed DDE and APSO algorithms being executed five times out of ten by using different random seeds are shown in Figs. 10 and 11, respectively to demonstrate the stability of the algorithms.

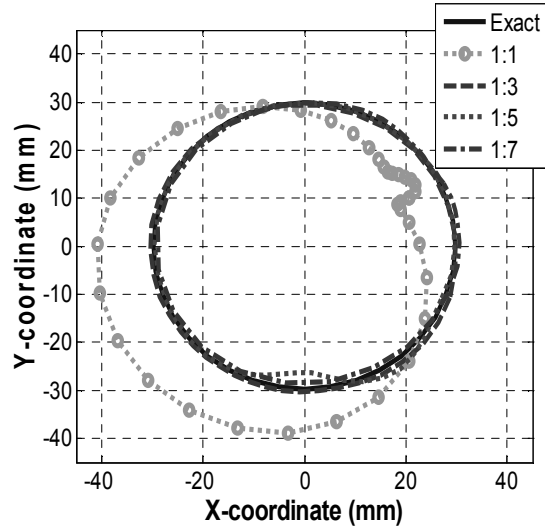


Fig. 8. The reconstructed shapes of the cylinder for example 1 by using different scaling ratios for the sub-grid via DDE. The shape function of this object is given by $F(\theta) = 29.75$ mm.

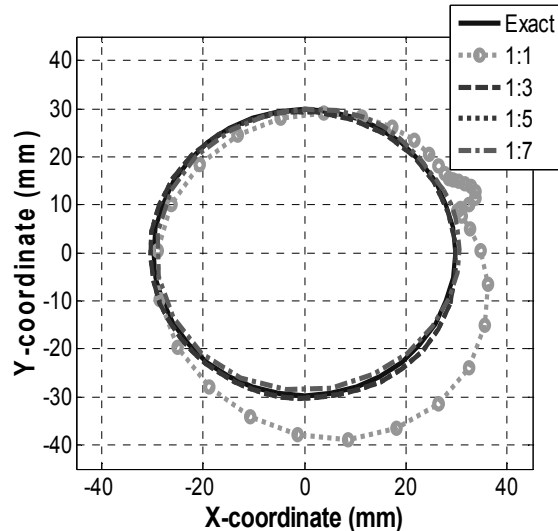


Fig. 9. The reconstructed shapes of the cylinder for example 1 by using different scaling ratios for the sub-grid via APSO. The shape function of this object is given by $F(\theta) = 29.75$ mm.

For the second example, a non-symmetric perfectly conducting cylinder with shape function $F(\theta) = 29.75 + 11.9 \cos(2\theta) + 5.95 \sin(\theta) + 5.95 \sin(2\theta)$ (unit:mm) is considered. Figure 12 shows the reconstructed images by of the use of DDE, APSO, DE and PSO algorithms for comparison. The values of DF for DDE, APSO, DE and PSO are about 5.8%, 11.4%, 17.9% and 25.3% in the final generation, respectively. The cost function value versus the number of function call is shown in Fig. 13. PSO is severely affected by premature convergence and stagnation problem. The key differences between PSO and APSO are about the convergence speed, the computation time and the accuracy, since APSO includes damping boundary condition scheme and mutation scheme. The performance of DDE is the best in this example.

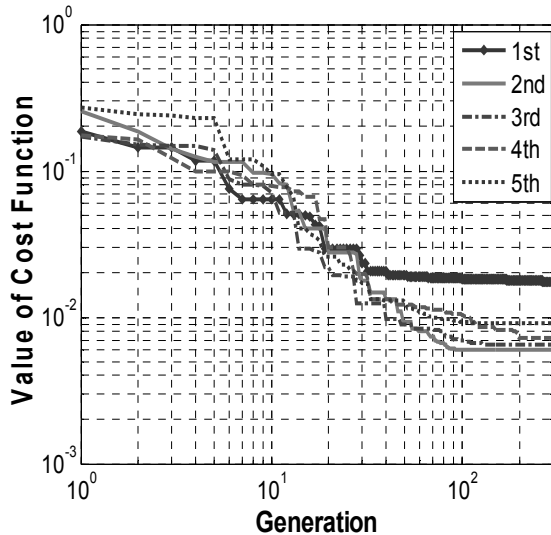


Fig. 10. The convergence curves of the cost function versus generation as the proposed DDE algorithm being executed five times out of ten by using different tables of random number.

In order to investigate the sensitivity of the imaging algorithm against random noise, the mimical experimental scattered fields are then contaminated by white Gaussian noise of zero mean. The relative noise level (RNL) is defined as:

$$RNL = \frac{\sigma_g}{\sqrt{\frac{\sum_{n=1}^{N_i} \sum_{m=1}^{M_i} \sum_{k=0}^K |E_z^{\text{exp}}(n, m, k\Delta t)|^2}{(N_i)(M_i)(K+1)}}} \quad (20)$$

The relative noise levels of 10^{-4} , 10^{-3} , 10^{-2} , 0.1 and 0.5 are tested. Figure 14 shows the values of DF of the final reconstructed results vs. RNL. It is observed that good reconstruction can be achieved regarding the shape of the metallic cylinder when the relative noise level is below 10^{-2} .

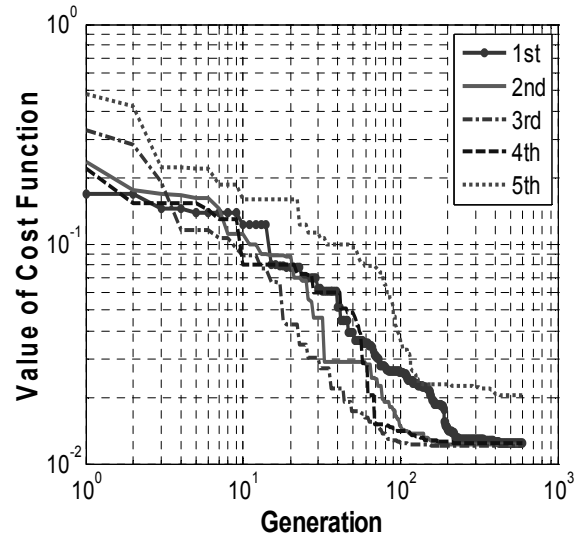


Fig. 11. The convergence curves of the cost function versus generation as the proposed APSO being executed five times out of ten by using different tables of random number.

For the third example, the shape function of this object is given by $F(\theta) = 29.75 + 5.95 \cos(3\theta)$ (unit:mm) is considered. Figure 15 shows that the reconstructed images by of the use of DDE, APSO, DE and PSO algorithms for comparison. The values of DF for DDE, APSO, DE and PSO are about 5.3%, 9.6%, 14.3% and 19.6% in the final generation, respectively. Figure 16 shows that the cost function versus the number of function call. It is clear that the DDE and APSO outperform PSO. The latter PSO is severely affected by premature convergence and/or stagnation problem, while the former DDE and APSO are more robust to avoid local optimal due to the inclusion of dynamic update and/or the “Best” concept for optimization as mentioned previously [32]-[34].

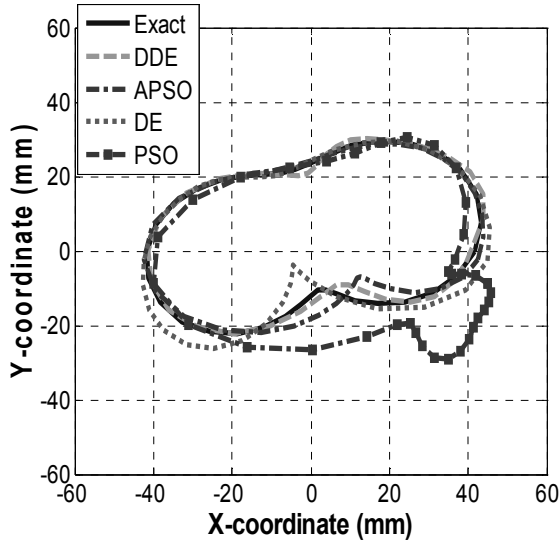


Fig. 12. The reconstructed cross section of the cylinder of example 2 by DDE, APSO, DE and PSO. The shape function of this object is given by $F(\theta) = 29.75 + 11.9\cos(2\theta) + 5.95\sin(\theta) + 5.95\sin(2\theta)$ mm.

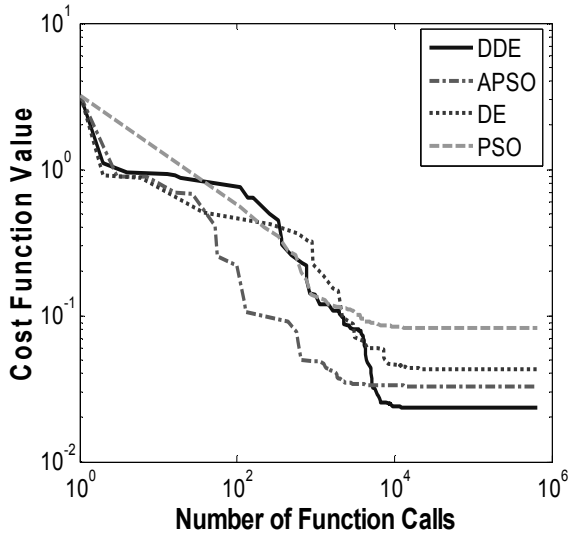


Fig. 13. The value of cost function versus the number of function call for example 2. The shape function of this object is given by $F(\theta) = 29.75 + 11.9\cos(2\theta) + 5.95\sin(\theta) + 5.95\sin(2\theta)$ mm.

Again, investigation on the sensitivity of the imaging algorithms against random noise is conducted for this example. Figure 17 shows the values of DF of the final reconstructed results vs. RNL. It could be observed that good reconstruction can be achieved regarding the shape of the metallic cylinder when the relative noise level is below 10^{-2} . It is worth to mention that the

image reconstruction at the backside of the scatterer is relative hard due to the shadowing effect in example 3.

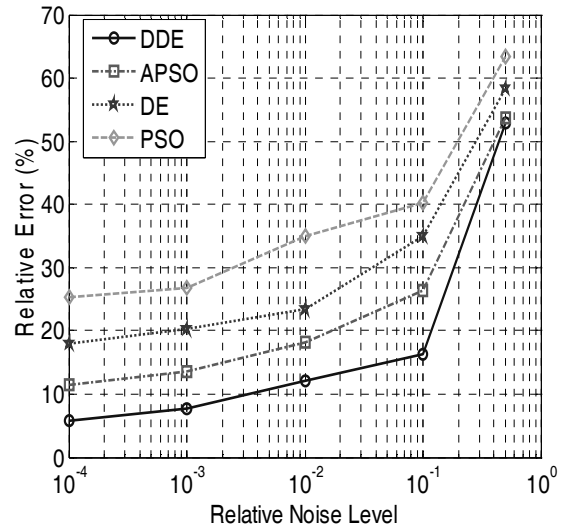


Fig. 14. Shape error as function of RNL by DDE, APSO, DE and PSO, respectively. The shape function of this object is given by $F(\theta) = 29.75 + 11.9\cos(2\theta) + 5.95\sin(\theta) + 5.95\sin(2\theta)$ mm.

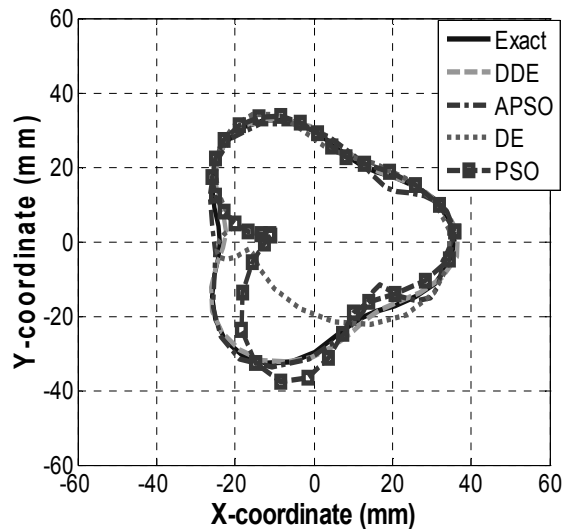


Fig. 15. The reconstructed cross section of the cylinder of example 3 by DDE, APSO, DE and PSO. The shape function of this object is given by $F(\theta) = 29.75 + 17.85\cos(3\theta)$ mm.

Finally, the computational burden, which is related to the generation of new solution candidates from the previous ones, is roughly the same for DDE and APSO. For the shape reconstruction examples studied, the computation

time is dominated by the FDTD procedure of the direct-scattering problems.

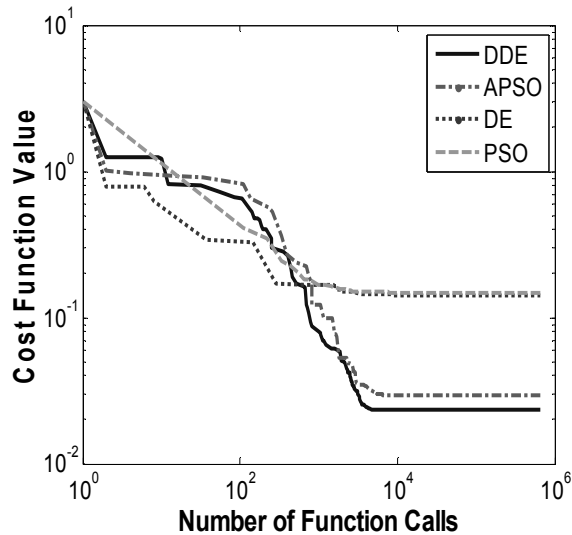


Fig. 16. The value of cost function versus the number of function call for example 2. The shape function of this object is given by $F(\theta) = 29.75 + 17.85 \cos(3\theta)$ mm.

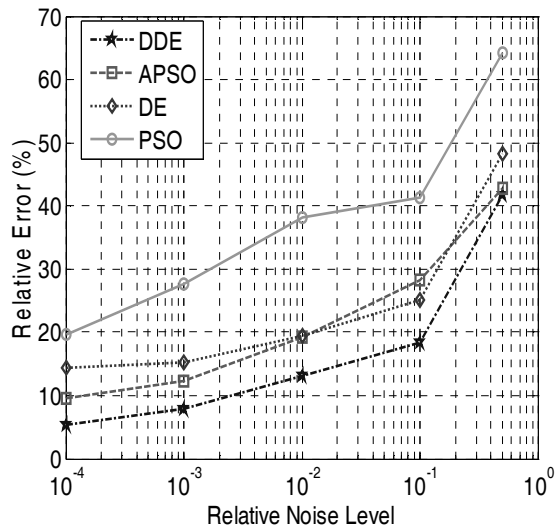


Fig. 17. Shape error as function of RNL by DDE, APSO, DE and PSO, respectively. The shape function of this object is given by $F(\theta) = 29.75 + 17.85 \cos(3\theta)$ mm.

V. CONCLUSION

The problem of shape reconstruction of perfectly conducting cylinder is investigated by applying DDE, APSO, DE and PSO techniques, for which the inverse problem is reformulated into an optimization one. Since both DDE and APSO

realize the ideas of approaching the “Best” and dynamic updating, they exhibit similar searching capability and convergence property and outperform DE and PSO. Numerical results show that DDE and APSO are reliable for the time domain inverse problem of 2D metallic cylinder even when the initial guess is far from the exact one. Moreover, DDE and APSO can result in accurate reconstruction even when the effects of noise are included under the condition of noise level less than 10^{-2} . It should be mentioned that this comparative study is indicative and its conclusion should not be considered generally applicable in all inverse scattering problems.

ACKNOWLEDGMENT

This work was supported by National Science Council, Republic of China, under Grant NSC 101-2221-E-229-001.

REFERENCES

- [1] C. H. Huang, C. C. Chiu, C. J. Lin, Y. F. Chen, "Inverse Scattering of Inhomogeneous Dielectric Cylinders Buried in a Slab Medium by TE Wave Illumination," *Applied Computational Electromagnetics Society (ACES) Journal*, vol. 22, no. 2, pp. 295 - 301, July 2007.
- [2] G. Oliveri, P. Rocca, and A. Massa, "A Bayesian Compressive Sampling-based Inversion for Imaging Sparse Scatterers," *IEEE Transactions on Geosciences and Remote Sensing*, vol. 49, no. 10, pp. 3993-4006, October, 2011.
- [3] L. Poli, G. Oliveri, and A. Massa, "Microwave Imaging within the First-order Born Approximation by means of the Contrast-field Bayesian Compressive Sensing," *IEEE Transactions on Antennas and Propagation*, vol. 60, no. 6, pp. 2865-2879, Jun. 2012.
- [4] L. Pan, Y. Zhong, X. Chen and S. P. Yeo "Subspace-Based Optimization Method for Inverse Scattering Problems Utilizing Phaseless Data," *IEEE Transactions Geoscience and Remote Sensing*, vol. 49, no. 3, pp. 981 - 987, Mar. 2011
- [5] I. Jeffrey, V. I. Okhmatovski, J. LoVetri, C. Gilmore, "An Adaptive Basis Function Solution to the 1D and 2D Inverse Scattering Problems using the DBIM and the BIM," *Applied Computational Electromagnetics Society (ACES) Journal*, vol. 22, no. 1, pp. 60-70, March 2007.
- [6] C. Loo, M. Hamid, "Inverse Scattering of a Dielectric Sphere Partially Buried in a Ground Plane Using a Radial Basis Function Network," *Applied Computational Electromagnetics Society (ACES) Journal*, vol. 19, no. 3, pp. 135-146, November 2004.

- [7] C. H. Sun, C. C. Chiu, and C. J. Lin "Image Reconstruction of Inhomogeneous Biaxial Dielectric Cylinders Buried in a Slab Medium.", *International Journal of Applied Electromagnetics and Mechanics*, vol. 34, no.1, 2, pp. 33-48, Nov. 2010.
- [8] C. H. Sun and C. C. Chiu "Electromagnetic imaging of Buried Perfectly Conducting Cylinders Targets Using the Dynamic Differential Evolution." *International Journal of RF and Microwave Computer-Aided Engineering*. vol. 22, no 2, pp. 141-146, Mar. 2012.
- [9] C. H. Sun, C. C. Chiu, and C. J. Lin "Image Reconstruction of Inhomogeneous Biaxial Dielectric Cylinders Buried in a Slab Medium." *International Journal of Applied Electromagnetics and Mechanics*, vol. 34, no.1, 2, pp. 33-48, Nov. 2010.
- [10] W. Chien, C. H. Sun, C. C. Chiu, "Image Reconstruction for a Partially Immersed Imperfectly Conducting Cylinder by Genetic Algorithm," *International Journal of Imaging Systems and Technology* vol. 19, pp. 299-305, Dec. 2009.
- [11] P. C. Sabatier, "Theoretical Considerations for Inverse Scattering," *Radio Science*, vol. 18, pp. 629 - 631, Jan. 1983.
- [12] R. Storn, and K. Price, "Differential Evolution - a Simple and Efficient Adaptive Scheme for Global Optimization over Continuous Spaces," Technical Report TR-95-012, International Computer Science Institute, Berkeley, 1995.
- [13] J. Kennedy and R. C. Eberhart, "Particle Swarm Optimization," *Proceedings of the IEEE International Conference on Neural Network*, pp. 1942-1948, 1995.
- [14] I. T. Rekanos, "Shape Reconstruction of a Perfectly Conducting Scatterer Using Differential Evolution and Particle Swarm Optimization," *IEEE Transactions on Geoscience and Remote Sensing*, vol. 46, no. 7, pp. 1967-1974, 2008.
- [15] A. Semnani and M. Kamyab, "An Enhanced Method for Inverse Scattering Problems Using Fourier Series Expansion in Conjunction with FDTD and PSO," *Progress In Electromagnetic Research*. PIER 76, pp. 45-64, 2007.
- [16] M. Farmahini-Farahani, R. Faraji-Dana, M. Shahabadi, "Fast and Accurate Cascaded Particle Swarm Gradient Optimization Method for Solving 2-D Inverse Scattering Problems," *Applied Computational Electromagnetics Society (ACES) Journal*, vol. 24, no. 5, pp. 511-517, October 2009.
- [17] C. H. Sun, C. L. Liu, K. C. Chen, C. C. Chiu, C. L. Li, and C. C. Tasi, "Electromagnetic Transverse Electric Wave Inverse Scattering of a Partially Immersed Conductor by Steady-State Genetic Algorithm," *Electromagnetics*. vol. 28, no. 6, pp. 389-400, Aug. 2008.
- [18] W. Chien, C-C. Chiu, "Cubic-Spline Expansion with GA for Half-Space Inverse Problems," *Applied Computational Electromagnetics Society (ACES) Journal*, vol. 20, no. 2, pp. 136-143, July 2005.
- [19] C. C. Chiu, C. H. Sun and Y. S. Fan "Shape Reconstruction of 2-D Perfectly Conducting Cylinder Targets Using the Particle Swarm Optimization." *Imaging Science Journal*. vol. 60, no. 2, pp. 83-89, Apr. 2012.
- [20] A. E. Yagle and J. L. Frolik, "On the Feasibility of Impulse Reflection Response Data for the Two-dimensional Inverse Scattering Problem," *IEEE Transactions on Antennas and Propagation*. vol. 44, no. 12, pp. 1551-1564, Dec. 1996.
- [21] M. Moghaddam, W. C. Chew, and M. Oristaglio, "A Comparison of the Born Iterative Method and Tarantola's Method for an Electromagnetic Time-domain Inverse Problem," *International Journal of Imaging Systems and Technology*, vol. 3, pp. 318-333, 1991.
- [22] W. H. Weedon, "Broadband Microwave Inverse Scattering: Theory and Experiment," Ph.D. dissertation, University of Illinois at Urbana-Champaign, 1994.
- [23] I. T. Rekanos, "Time-domain Inverse Scattering using Lagrange Multipliers: an Iterative FDTD-based Optimization Technique," *Journal of Electromagnetic Waves and Applications*, vol. 17, no. 2, pp. 271-289, 2003.
- [24] M. Benedetti, D. Lesselier, M. Lambert, and A. Massa, "A Multi-resolution Technique Based on Shape Optimization for the Reconstruction of Homogeneous Dielectric Objects," *Inverse Problems*, vol. 25, no. 1, pp. 1-26, January 2009.
- [25] C. H. Huang, Y. F. Chen, and C. C. Chiu, "Permittivity Distribution Reconstruction of Dielectric Objects by a Cascaded Method," *Journal of Electromagnetic Waves and Applications* vol. 21, no. 2, pp. 145-159, Jan. 2007.
- [26] C. H. Sun, C. L. Li, C. C. Chiu and C. H. Huang, "Time Domain Image Reconstruction for a Buried 2D Homogeneous Dielectric Cylinder Using NU-SSGA.", *Research in Nondestructive Evaluation*, vol. 22, no.1, pp. 1-15, Jan. 2011.
- [27] C. H. Huang, C. C. Chiu, C. L. Li, and Y.-H. Li, "Image Reconstruction of the Buried Metallic Cylinder Using FDTD Method and SSGA," *Progress In Electromagnetic Research*. PIER 85, pp. 195-210, Aug. 2008.
- [28] C. H. Huang, C. H. Chen, C. C. Chiu and C. L. Li, "Reconstruction of the Buried Homogenous

- Dielectric Cylinder by FDTD and Asynchronous Particle Swarm Optimization.” *Applied Computational Electromagnetics Society (ACES) Journal*, vol. 25, no. 8, pp. 672-681, Aug. 2010.
- [29] C. H. Sun, C. C. Chiu and C. L. Li, “Time-Domain Inverse Scattering of a Two-dimensional Metallic Cylinder in Slab Medium Using Asynchronous Particle Swarm Optimization.”, *Progress In Electromagnetic Research M. (PIERM)*, vol. 14, pp. 85-100. Aug. 2010.
- [30] A. Semnani, M. Kamyab, “An Enhanced Hybrid Method for Solving Inverse Scattering Problems,” *IEEE Transactions on Magnetics*, vol. 45, no. 3, pp. 1534-1537, Mar. 2009.
- [31] C. C. Chiu, C. H. Sun and W. L. Chang “Comparison of Particle Swarm Optimization and Asynchronous Particle Swarm Optimization for Inverse Scattering of a Two-Dimensional Perfectly Conducting Cylinder.”, *International Journal of Applied Electromagnetics and Mechanics*, vol. 35, no.4, pp. 249-261, Apr. 2011.
- [32] C. H. Sun, C. C. Chiu, C. L. Li, and C. H. Huang, “Time Domain Image Reconstruction for Homogenous Dielectric Objects by Dynamic Differential Evolution,” *Electromagnetics*. vol. 30, no. 4, pp. 309-323, May 2010.
- [33] C. H. Sun, C. C. Chiu, W. Chien and C. L. Li, “Application of FDTD and Dynamic Differential Evolution for Inverse Scattering of a Two-Dimensional Perfectly Conducting Cylinder in Slab Medium”, *Journal of Electronic Imaging*, vol. 19, 043016, Dec. 2010.
- [34] C. C. Chiu and C. H. Sun “A Study of Microwave Imaging for a Metallic Cylinder.” *International Journal of RF and Microwave Computer-Aided Engineering*, vol. 22, no. 5, pp. 632-638, Sept. 2012.
- [35] M. Donelli and A. Massa, “Computational Approach Based on a Particle Swarm Optimizer for Microwave Imaging of Two-dimensional Dielectric Scatterers,” *IEEE Trans. Microw. Theory Tech.*, vol. 53, no. 5, pp. 1761-1776, May 2005.
- [36] M. Donelli, G. Franceschini, A. Martini, and A. Massa, “An Integrated Multiscaling Strategy Based on a Particle Swarm Algorithm for Inverse Scattering Problems,” *IEEE Trans. Geosci. Remote Sens.*, vol. 44, no. 2, pp. 298-312, Feb. 2006.
- [37] C. C. Chiu and W. C. Hsiao “Comparison of Asynchronous Particle Swarm Optimization and Dynamic Differential Evolution for Partially Immersed Conductor.” *Waves in Random and Complex Media*. vol. 21, no. 3, pp. 485-500, Aug. 2011.
- [38] A. Semnani, M. Kamyab, and I. T. Rekanos, “Reconstruction of One-Dimensional Dielectric Scatterers Using Differential Evolution and Particle Swarm Optimization,” *IEEE Geoscience and Remote Sensing Letters*, vol. 6, no. 4, pp. 671-675, Oct. 2009.
- [39] M. W. Chevalier, R. J. Luebbers and V. P. Cable, “FDTD Local Grid with Material Traverse,” *IEEE Trans. Antennas and Propagation*, vol. 45, no. 3, pp. 411-421, March 1997.
- [40] C. de Boor, “*A Practical Guide to Splines*,” Springer-Verlag, New York, 1978.
- [41] K. Yee, “Numerical Solutions of Initial Boundary Value Problems involving Maxwell's Equations in Isotropic Media,” *IEEE Transactions on Antennas and Propagation*, vol. AP-14, pp. 302-307, 1966.
- [42] C. L. Li, C. W. Liu, and S. H. Chen, “Optimization of a PML Absorber's Conductivity Profile using FDTD,” *Microwave and Optical Technology Letters.*, vol. 37, pp. 380-383, 2003.
- [43] I. S. Kim and W. J. R. Hoefer, “A Local Mesh Refinement Algorithm for the Time-domain Finite-difference Method using Maxwell's Curl Equations,” *IEEE Trans. Microwave Theory Tech.*, vol. 38, no. 6, pp. 812-815, June 1990.
- [44] M. Clerc, “The Swarm and the Queen: Towards a Deterministic and Adaptive Particle Swarm Optimization,” *Proceedings of Congress on Evolutionary Computation*, Washington, DC, pp. 1951-1957, 1999.
- [45] A. Carlisle and G. Dozier, “An Off-The-Shelf PSO,” *Proceedings of the 2001 Workshop on Particle Swarm Optimization*, pp. 1-6, 2001.
- [46] T. Huang, A. S. Mohan, “A Hybrid Boundary Condition for Robust Particle Swarm Optimization,” *IEEE Antennas and Wireless Propagation Letters*, vol. 4, pp. 112-117, 2005.



Ching-Lieh Li was born November 24, 1963, in Pingtung, Taiwan. He received the B.S. degree from National Taiwan University, Taipei, Taiwan, in 1985, and the M.S. and Ph.D. degrees from Michigan State University, East Lansing, in 1990 and 1993, respectively, all in electrical engineering. From 1989 to 1993, he was a Research Assistant in the Electrical Engineering Department, Michigan State University, where he worked on the measurement techniques for determining the electromagnetic properties of materials. In 1993, he joined the Electrical Engineering Faculty at Tamkang University, Taipei, Taiwan, where now he is a professor. Currently, his research activities involve inverse scattering problem, and microstrip antenna design and dielectric material

characterization, etc.. His areas of special interest include theoretical and computational electromagnetics, and application of various optimization schemes such as SSGA, PSO, DE, and Taguchi method to electromagnetics.



Chung-Hsin Huang was born in New Taipei City, Taiwan, Republic of China, on February 1, 1980. He received M.S.E.E. and Ph.D degrees in electrical engineering from Tamkang University, Taipei, Taiwan, in 2004 and 2009 respectively. He is currently an

Assistant Professor with the Department of Computer and Communication Engineering, Taipei College of Maritime Technology. His current research interests include electromagnetic wave theory and applications, optimization methods, dielectric material characterization and wireless communications.



Chien-Ching Chiu received his BSCE degree from National Chiao Tung University, Hsinchu, Taiwan, in 1985 and his MSEE and PhD degrees from National Taiwan University, Taipei, in 1987 and 1991, respectively. From 1987 to

1989, he was a communication officer with the ROC Army Force. In 1992 he joined the faculty of the Department of Electrical Engineering, Tamkang University, where he is now a professor. From 1998 to 1999, he was a visiting scholar at the Massachusetts Institute of Technology, Cambridge, and the University of Illinois at Urbana-Champaign. He is a visiting professor with the University of Wollongong, Australia, in 2006. Moreover, he was a visiting professor with the University of London, United Kingdom, in 2011. His current research interests include microwave imaging, numerical techniques in electromagnetics, indoor wireless communications, and ultrawideband communication systems. He has published more than 100 journal papers on inverse scattering problems, communication systems and optimization algorithms.



Chi-Hsien Sun received M.S.E.E. and Ph.D degrees in electrical engineering from Tamkang University, Taipei, Taiwan, in 2008 and 2012 respectively. He is now with the Department of Electronic Engineering, NTUST, as a postdoctoral fellow since 2012.

His special interests include theoretical and computational electromagnetics, and application of various optimization schemes such as the steady state genetic algorithm (SSGA), particle swarm optimization (PSO), dynamic differential evolution (DDE), self-adaptive dynamic differential evolution (SADDE) and the Taguchi method in electromagnetics.

2012 INSTITUTIONAL MEMBERS

DTIC-OCP LIBRARY
8725 John J. Kingman Rd, Ste 0944
Fort Belvoir, VA 22060-6218

AUSTRALIAN DEFENCE LIBRARY
Northcott Drive
Canberra, A.C.T. 2600 Australia

BEIJING BOOK CO, INC
701 E Linden Avenue
Linden, NJ 07036-2495

DARTMOUTH COLLEGE
6025 Baker/Berry Library
Hanover, NH 03755-3560

DSTO EDINBURGH
AU/33851-AP, PO Box 830470
Birmingham, AL 35283

SIMEON J. EARL – BAE SYSTEMS
W432A, Warton Aerodome
Preston, Lancs., UK PR4 1AX

ENGINEERING INFORMATION, INC
PO Box 543
Amsterdam, Netherlands 1000 Am

ETSE TELECOMUNICACION
Biblioteca, Campus Lagoas
Vigo, 36200 Spain

GA INSTITUTE OF TECHNOLOGY
EBS-Lib Mail code 0900
74 Cherry Street
Atlanta, GA 30332

TIMOTHY HOLZHEIMER
Raytheon
PO Box 1044
Rockwall, TX 75087

HRL LABS, RESEARCH LIBRARY
3011 Malibu Canyon
Malibu, CA 90265

IEE INSPEC
Michael Faraday House
6 Hills Way
Stevenage, Herts UK SG1 2AY

INSTITUTE FOR SCIENTIFIC INFO.
Publication Processing Dept.
3501 Market St.
Philadelphia, PA 19104-3302

LIBRARY – DRDC OTTAWA
3701 Carling Avenue
Ottawa, Ontario, Canada K1A OZ4

LIBRARY of CONGRESS
Reg. Of Copyrights
Attn: 407 Deposits
Washington DC, 20559

LINDA HALL LIBRARY
5109 Cherry Street
Kansas City, MO 64110-2498

MISSOURI S&T
400 W 14th Street
Rolla, MO 56409

MIT LINCOLN LABORATORY
Periodicals Library
244 Wood Street
Lexington, MA 02420

NATIONAL CHI NAN UNIVERSITY
Lily Journal & Book Co, Ltd
20920 Glenbrook Drive
Walnut, CA 91789-3809

JOHN NORGARD
UCCS
20340 Pine Shadow Drive
Colorado Springs, CO 80908

OSAMA MOHAMMED
Florida International University
10555 W Flagler Street
Miami, FL 33174

NAVAL POSTGRADUATE SCHOOL
Attn:J. Rozdal/411 Dyer Rd./ Rm 111
Monterey, CA 93943-5101

NDL KAGAKU
C/O KWE-ACCESS
PO Box 300613 (JFK A/P)
Jamaica, NY 11430-0613

OVIEDO LIBRARY
PO BOX 830679
Birmingham, AL 35283

DAVID PAULSEN
E3Compliance
1523 North Joe Wilson Road
Cedr Hill, TX 75104-1437

PENN STATE UNIVERSITY
126 Paterno Library
University Park, PA 16802-1808

DAVID J. PINION
1122 E Pike Street #1217
SEATTLE, WA 98122

KATHERINE SIAKAVARA
Gymnasiou 8
Thessaloniki, Greece 55236

SWETS INFORMATION SERVICES
160 Ninth Avenue, Suite A
Runnemedede, NJ 08078

YUTAKA TANGE
Maizuru Natl College of Technology
234 Shiroya
Maizuru, Kyoto, Japan 625-8511

TIB & UNIV. BIB. HANNOVER
DE/5100/G1/0001
Welfengarten 1B
Hannover, Germany 30167

UEKAE
PO Box 830470
Birmingham, AL 35283

UNIV OF CENTRAL FLORIDA
4000 Central Florida Boulevard
Orlando, FL 32816-8005

UNIVERSITY OF COLORADO
1720 Pleasant Street, 184 UCB
Boulder, CO 80309-0184

UNIVERSITY OF KANSAS –
WATSON
1425 Jayhawk Blvd 210S
Lawrence, KS 66045-7594

UNIVERSITY OF MISSISSIPPI
JD Williams Library
University, MS 38677-1848

UNIVERSITY LIBRARY/HKUST
Clear Water Bay Road
Kowloon, Honk Kong

CHUAN CHENG WANG
8F, No. 31, Lane 546
MingCheng 2nd Road, Zuoying Dist
Kaoshiung City, Taiwan 813

THOMAS WEILAND
TU Darmstadt
Schlossgartenstrasse 8
Darmstadt, Hessen, Germany 64289

STEVEN WEISS
US Army Research Lab
2800 Powder Mill Road
Adelphi, MD 20783

YOSHIHIDE YAMADA
NATIONAL DEFENSE ACADEMY
1-10-20 Hashirimizu
Yokosuka, Kanagawa,
Japan 239-8686

INFORMATION FOR AUTHORS

PUBLICATION CRITERIA

Each paper is required to manifest some relation to applied computational electromagnetics. **Papers may address general issues in applied computational electromagnetics, or they may focus on specific applications, techniques, codes, or computational issues.** While the following list is not exhaustive, each paper will generally relate to at least one of these areas:

- 1. Code validation.** This is done using internal checks or experimental, analytical or other computational data. Measured data of potential utility to code validation efforts will also be considered for publication.
- 2. Code performance analysis.** This usually involves identification of numerical accuracy or other limitations, solution convergence, numerical and physical modeling error, and parameter tradeoffs. However, it is also permissible to address issues such as ease-of-use, set-up time, run time, special outputs, or other special features.
- 3. Computational studies of basic physics.** This involves using a code, algorithm, or computational technique to simulate reality in such a way that better, or new physical insight or understanding, is achieved.
- 4. New computational techniques** or new applications for existing computational techniques or codes.
- 5. “Tricks of the trade”** in selecting and applying codes and techniques.
- 6. New codes, algorithms, code enhancement, and code fixes.** This category is self-explanatory, but includes significant changes to existing codes, such as applicability extensions, algorithm optimization, problem correction, limitation removal, or other performance improvement. **Note: Code (or algorithm) capability descriptions are not acceptable, unless they contain sufficient technical material to justify consideration.**
- 7. Code input/output issues.** This normally involves innovations in input (such as input geometry standardization, automatic mesh generation, or computer-aided design) or in output (whether it be tabular, graphical, statistical, Fourier-transformed, or otherwise signal-processed). Material dealing with input/output database management, output interpretation, or other input/output issues will also be considered for publication.
- 8. Computer hardware issues.** This is the category for analysis of hardware capabilities and limitations of various types of electromagnetics computational requirements. Vector and parallel computational techniques and implementation are of particular interest. Applications of interest include, but are not limited to,

antennas (and their electromagnetic environments), networks, static fields, radar cross section, inverse scattering, shielding, radiation hazards, biological effects, biomedical applications, electromagnetic pulse (EMP), electromagnetic interference (EMI), electromagnetic compatibility (EMC), power transmission, charge transport, dielectric, magnetic and nonlinear materials, microwave components, MEMS, RFID, and MMIC technologies, remote sensing and geometrical and physical optics, radar and communications systems, sensors, fiber optics, plasmas, particle accelerators, generators and motors, electromagnetic wave propagation, non-destructive evaluation, eddy currents, and inverse scattering.

Techniques of interest include but not limited to frequency-domain and time-domain techniques, integral equation and differential equation techniques, diffraction theories, physical and geometrical optics, method of moments, finite differences and finite element techniques, transmission line method, modal expansions, perturbation methods, and hybrid methods.

Where possible and appropriate, authors are required to provide statements of quantitative accuracy for measured and/or computed data. This issue is discussed in “Accuracy & Publication: Requiring, quantitative accuracy statements to accompany data,” by E. K. Miller, *ACES Newsletter*, Vol. 9, No. 3, pp. 23-29, 1994, ISBN 1056-9170.

SUBMITTAL PROCEDURE

All submissions should be uploaded to ACES server through ACES web site (<http://aces.ee.olemiss.edu>) by using the upload button, journal section. Only pdf files are accepted for submission. The file size should not be larger than 5MB, otherwise permission from the Editor-in-Chief should be obtained first. Automated acknowledgment of the electronic submission, after the upload process is successfully completed, will be sent to the corresponding author only. It is the responsibility of the corresponding author to keep the remaining authors, if applicable, informed. Email submission is not accepted and will not be processed.

EDITORIAL REVIEW

In order to ensure an appropriate level of quality control, papers are peer reviewed. They are reviewed both for technical correctness and for adherence to the listed guidelines regarding information content and format.

PAPER FORMAT

Only camera-ready electronic files are accepted for publication. The term **“camera-ready”** means that the material is neat, legible, reproducible, and in accordance with the final version format listed below.

The following requirements are in effect for the final version of an ACES Journal paper:

1. The paper title should not be placed on a separate page.

The title, author(s), abstract, and (space permitting) beginning of the paper itself should all be on the first page. The title, author(s), and author affiliations should be centered (center-justified) on the first page. The title should be of font size 16 and bolded, the author names should be of font size 12 and bolded, and the author affiliation should be of font size 12 (regular font, neither italic nor bolded).

2. An abstract is required. The abstract should be a brief summary of the work described in the paper. It should state the computer codes, computational techniques, and applications discussed in the paper (as applicable) and should otherwise be usable by technical abstracting and indexing services. The word "Abstract" has to be placed at the left margin of the paper, and should be bolded and italic. It also should be followed by a hyphen (–) with the main text of the abstract starting on the same line.
3. All section titles have to be centered and all the title letters should be written in caps. The section titles need to be numbered using roman numbering (I. II.)
4. Either British English or American English spellings may be used, provided that each word is spelled consistently throughout the paper.
5. Internal consistency of references format should be maintained. As a guideline for authors, we recommend that references be given using numerical numbering in the body of the paper (with numerical listing of all references at the end of the paper). The first letter of the authors' first name should be listed followed by a period, which in turn, followed by the authors' complete last name. Use a coma (,) to separate between the authors' names. Titles of papers or articles should be in quotation marks (" "), followed by the title of journal, which should be in italic font. The journal volume (vol.), issue number (no.), page numbering (pp.), month and year of publication should come after the journal title in the sequence listed here.
6. Internal consistency shall also be maintained for other elements of style, such as equation numbering. Equation numbers should be placed in parentheses at the right column margin. All symbols in any equation have to be defined before the equation appears or right immediately following the equation.
7. The use of SI units is strongly encouraged. English units may be used as secondary units (in parentheses).
8. Figures and tables should be formatted appropriately (centered within the column, side-by-side, etc.) on the page such that the presented data appears close to and after it is being referenced in the text. When including figures and tables, all care should be taken so that they will appear appropriately when printed in black and white. For better visibility of paper on computer screen, it is good to make color figures with different line styles for figures with multiple curves. Colors should also be tested to insure their ability to be distinguished after

black and white printing. Avoid the use of large symbols with curves in a figure. It is always better to use different line styles such as solid, dotted, dashed, etc.

9. A figure caption should be located directly beneath the corresponding figure, and should be fully justified.
10. The intent and meaning of all text must be clear. For authors who are not masters of the English language, the ACES Editorial Staff will provide assistance with grammar (subject to clarity of intent and meaning). However, this may delay the scheduled publication date.
11. Unused space should be minimized. Sections and subsections should not normally begin on a new page.

ACES reserves the right to edit any uploaded material, however, this is not generally done. It is the author(s) responsibility to provide acceptable camera-ready files in pdf and MSWord formats. Incompatible or incomplete files will not be processed for publication, and authors will be requested to re-upload a revised acceptable version.

COPYRIGHTS AND RELEASES

Each primary author must execute the online copyright form and obtain a release from his/her organization vesting the copyright with ACES. Both the author(s) and affiliated organization(s) are allowed to use the copyrighted material freely for their own private purposes.

Permission is granted to quote short passages and reproduce figures and tables from and ACES Journal issue provided the source is cited. Copies of ACES Journal articles may be made in accordance with usage permitted by Sections 107 or 108 of the U.S. Copyright Law. This consent does not extend to other kinds of copying, such as for general distribution, for advertising or promotional purposes, for creating new collective works, or for resale. The reproduction of multiple copies and the use of articles or extracts for commercial purposes require the consent of the author and specific permission from ACES. Institutional members are allowed to copy any ACES Journal issue for their internal distribution only.

PUBLICATION CHARGES

All authors are allowed for 8 printed pages per paper without charge. Mandatory page charges of \$75 a page apply to all pages in excess of 8 printed pages. Authors are entitled to one, free of charge, copy of the printed journal issue in which their paper was published. Additional reprints are available for \$ 50. Requests for additional re-prints should be submitted to the managing editor or ACES Secretary.

Corresponding author is required to complete the online form for the over page charge payment right after the initial acceptance of the paper is conveyed to the corresponding author by email.

ACES Journal is abstracted in INSPEC, in Engineering Index, DTIC, Science Citation Index Expanded, the Research Alert, and to Current Contents/Engineering, Computing & Technology.